TOWARDS HIGH RESOLUTION ENDOSCOPIC OPTICAL COHERENCE TOMOGRAPHY FOR IMAGING INTERNAL ORGANS

by
Jessica Mavadia-Shukla

A dissertation submitted to Johns Hopkins University in conformity with the requirements for the degree of Doctor of Philosophy

Baltimore, Maryland

November, 2017

ABSTRACT

Optical coherence tomography (OCT) is a light based interferometric imaging technique that can provide high resolution (5-20 μm at 1300 nm), depth resolved, images in real-time. With recent advances in portable low coherent light sources for OCT it is now possible to achieve ultrahigh axial resolutions (≤ 3 μm) by moving to shorter central wavelengths such as 800 nm while utilizing a broad spectral bandwidth. Our goal was to push ultrahigh resolution OCT technology to *in vivo* imaging of internal organs for endoscopic assessment of tissue microstructure. This dissertation is separated into technological developments and biomedical imaging studies.

Technological developments in this dissertation included development of a high speed, ultrahigh resolution distal scanning catheter. This catheter was based upon a miniature DC micromotor capable of rotational velocities in excess of 100 rps, a diffractive compound lens design that minimized chromatic aberrations, and a mechanical assembly that limited field of view blockage to less than 7.5% and maintained an outer diameter of 1.78 mm (with plastic sheath). In conjunction with the algorithm described in chapter 4 to correct for non-uniform rotational distortion, the overall imaging system was capable of high quality endoscopic imaging of internal organs *in vivo*.

Equipped with the ultrahigh resolution endoscopic OCT system, imaging was performed in small airways and colorectal cancer. Imaging results demonstrated the ability to directly visualization of microstructural details such as airway smooth muscle in the small airways representing a major step forward in pulmonary imaging. With the

ability to visualize airway smooth muscle, morphological changes in COPD and related diseases can be further investigated. Additionally, longitudinal changes in an ETBF induced colon cancer model in APC^{Min} mice were studied as well. Quantitative assessment of tissue microarchitecture was performed by measuring the attenuation coefficient to find a bimodal distribution separating normal healthy tissue from polyps.

Finally, results from two additional projects were also demonstrated. Chapter 7 shows some results from vascular imaging in a tumor angiogenesis model and middle cerebral artery occlusion model. Chapter 8 describes an endoscopic multimodal OCT and fluorescence imaging platform with results in *ex vivo* rabbit esophagus.

Advisor:

_____

Xingde Li

Readers:

_____

Wayne Mitzner

DEDICATION

To the Mavadia and Shukla Parivar

ACKNOWLEDGEMENTS

The work performed in this dissertation could not have been accomplished without each lab member in the Biophotonics Imaging Technologies (BIT) Laboratory under the guidance and supervision of Professor Xingde Li. Specifically, working with Dr. Jiefeng Xi, Dr. Kartikeya Murari, Dr. Yuying Zhang, Dr. Huiquan Wang, Dr. Jianlin Zhang, Dr. Yongping Chen, Dr. Carmen Kut, and Wenxuan Liang have comprised of the best learning moments.

Professor Li taught me to have a clear thought process to approach a problem such that it can be rationally thought out and solved. Even with an enormously busy schedule, he has always been interested in the status of our work and never failed to ensure our research was complete and competitive. His instructions and thoughts and critical remarks on my writing forced me to improve immensely and are greatly appreciated.

I have had the great fortune of working with wonderful collaborators such as Professor Wayne Mitzner and Dr. Robert Brown, Dr. Cynthia Sears, Dr. Shaoguang Wu, Payam Fathi, Dr. Raymond Kohler, and Dr. Suyi Cao. These collaborations taught me to appreciate the underlying physiological processes in airway physiology, colorectal cancer, and cerebral hemodynamics. These collaborations also taught me to appreciate the multidisciplinary nature of biomedical engineering. Without a fundamental biomedical problem, engineering has no discernable goal.

I thank the thesis proposal committee members, Dr. Irina Burd and Dr. Stephen Belkoff for their support and encouragement, as well as their time and valuable advice in

strengthening my thesis. I also thank the current thesis committee members who have Dr. Ishan Barman and Dr. Jin Kang. Dr. Barman taught me to dig deeper into the significance of my work beyond engineering for the sake of engineering, and Dr. Jin Kang provided support and advice whenever necessary as well as encouragement to pursue my career goals whatever they might be.

Finally, I want to thank the Mavadia and Shukla families for their unconditional love and support, especially to my brother Jay Mavadia and my husband Sagar Shukla for believing in me and pushing me to be a better person. There are no words to express my love and gratitude to these two people.

Table of Contents

Table of Figures

Table of Tables

Chapter 1 Introduction

1.1 *Overview*

The field of medical imaging strives to visualize anatomical and physiological characteristics of the human body in order to apply it to the study, diagnosis, guidance and treatment of disease. To achieve this goal, over the years, many types of imaging modalities have been invented and developed such as magnetic resonance imaging (MRI), X-ray computed tomography (X-Ray/CT), ultrasound (US), and optical imaging. Each medical imaging modality has a given spatial resolution, penetration depth and field of view as well as a unique mechanism of contrast. High spatial resolution comes at the cost of limited penetration depth or field of view as can be seen from Figure 1.1.

The resolution, penetration depth and especially the mechanism of contrast, govern which modality is used in a particular situation. For example, MRI is exceptionally well suited to visualizing soft tissues like the human brain. Alternatively, CT visualizes bones much more efficiently than surrounding soft tissue due to the fact that bones absorb x-rays more efficiently. In the case of disease diagnosis, confocal microscopy might be better suited to confirm cell type, structure or quantity. Each modality has unique advantages and disadvantages that govern its use in the clinical workspace.

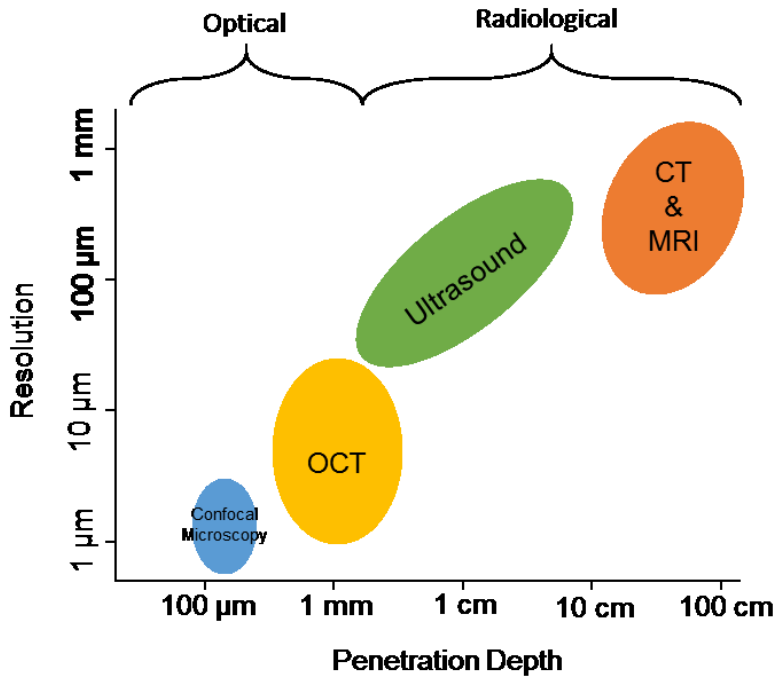

Figure 1.1 Resolution versus imaging depth for various imaging modalities.

This graph is separated into two categories, optical imaging modalities and radiological imaging modalities. Optical imaging modalities include confocal microscopy and optical coherence tomography (OCT). Radiological imaging modalities include ultrasound (US), X-Ray computed tomography (CT), and magnetic resonance imaging (MRI).

Confocal microscopy and optical coherence tomography (OCT) are grouped together as optical imaging modalities, while ultrasound (US), CT and MRI are grouped as radiological imaging modalities. Radiological imaging modalities are more widely used in the clinic for surveillance and diagnosis compared to optical imaging modalities. Optical imaging modalities have many advantages aside from high resolution imaging, such as the ability to perform imaging with non-ionizing radiation, making it safer for *in vivo* use and repeated imaging. Optical imaging is also well suited to imaging soft tissues

due to the way different tissues scatter and absorb light differently. Optical imaging has a rich history leading to development of one of the first optical imaging instruments for *in vivo* imaging of internal organs, an endoscope.

1.2 *Brief History of Microscopy and the First Endoscope*

Optical microscopy has been employed for centuries in the field of biology with the first recorded microscopic observations of the bee and weevil between the years of 1625 and 1630 [1]. Continuing efforts in the field of microscopy led to the discovery of cells in 1665 and development of the fields of bacteriology and cellular pathology in the mid to late 1800's [2]. Rudolph Virchow employed optical microscopy to the field of cellular pathology in order to demonstrate that diseases arise from abnormalities in cellular processes, as well as recognizing the idea of cell division. Virchow's insights led to a new type of pathology where previously understood organ based diseases could now be linked to cell-based diseases [3]. From the 1850's onward, histopathology for disease diagnosis became more important [3] leading to an increased interest in visualization of cells in medical science and emergence of optical microscopy.

Optical microscopy emerged as a popular tool for understanding disease on a cellular basis however, it was not able to be used *in vivo*. In order to be able to someday perform microscopy *in vivo*, it would be necessary to first consider how to find a way to deliver and collect light to the parts of the body that need to be studied. The first foray into such a technology was an endoscope. An endoscope was the first device that was able to deliver light into the human body (through natural orifices) for inspection or diagnosis. The first reports of a functional endoscope were around the early 1800's by Phillip Bozzini. Bozzini developed a rigid endoscope based on varying diameters and

lengths of funnels and an intricate system of flat and curved mirrors with candlelight as a source of illumination. Although there is debate over evidence showing that it was indeed employed in humans, some sources state that it was used to visualize the urethra and urinary bladder [4, 5] and possibly used for rectal and uterine inspection as well [6]. Unfortunately candle light was not bright enough and visualization was still poor. A few decades later, in the mid 1800's, Antonin Jean Desormeaux had made numerous upgrades to the existing endoscope including development of a new light source with greater brightness and improved upon the focusing ability with lenses [6]. Desmoreaux was also one of the earliest physicians to successfully perform surgical procedures endoscopically and is widely considered the father of cystoscopy/endoscopy [4, 5].

A few more key technological developments such as the in the light source, addition of accessory channel, development of a flexible endoscope, and development of a miniature CCD/CMOS sensor (in place of a fiber bundle) would be required to bring endoscopic technology into the 21st century. Through all of these engineering developments, endoscopy was able to perform much higher spatial resolution imaging of the surface of organs. Numerous tools were also developed to help physicians obtain small tissue samples endoscopically, however in order to finally diagnose disease it would be important to perform a histological examination of the tissue sample to visualize the cell structure, organization, number and size. To this effect, many additional technologies were developed such as confocal endomicroscopy, chromoendoscopy, narrowband imaging, and more recently OCT which enables high resolution depth resolved imaging.

1.3 *Confocal Endomicroscopy*

Confocal endomicroscopy is an extension of the confocal microscope which was invented in 1955 by Marvin Minsky [7]. Confocal microscopy illuminates the sample with a point source and employs a pinhole aperture prior to detection in order to reject out of focus light from above and below the focal plane. By scanning the focal spot across the sample, it is possible to form two and three dimensional images with confocal microscopy.

Introduction of a single mode fiber as the point source and pinhole in reflectance confocal microscopy incited development of confocal endomicroscopy, however it was still difficult to produce an entire image because a scanning mechanism was required before or after the fiber [8, 9]. A solution to this challenge was presented in 1993 when a fiber-optic imaging bundle was introduced in lieu of a single mode fiber. Although the paper only demonstrated proof-of-concept, a fiber bundle enabled scanning to be performed proximally with a simple, stationary, robust distal end placed in proximity to the sample [10]. Fiber-optic imaging bundles became very popular and were able to be used in a variety of applications for *in vitro* [11, 12] and *in vivo* imaging [13-15]. Furthermore, with the addition of ultrathin GRIN lenses, the overall size of a confocal endomicroscope was able to be reduced to fit into the accessory port of an endoscope [16].

Confocal endomicroscopy represented a huge change in the way traditional endoscopy was performed and really enabled physicians to perform high resolution optical imaging with near histological resolution. Some of the major drawbacks to this approach are the small field of view that can be captured (usually < 1mm diameter) and

need to scan over the entire field of view. Another optical imaging modality that holds great promise for *in vivo* examination is OCT.

1.4 *OCT*

1.4.1 Background

OCT is an interferometric technique that employs low coherence interferometry (LCI) to perform depth resolved imaging. LCI (also known as white light interferometry (WLI)) employs an interferometer under a low (temporal) coherent light source. Interference fringes are generated from the cross-correlation of light back-reflected (backscattered) from the sample and reference arm mirrors. In LCI, the mirror in the sample arm is replaced by a sample or device under test. Back-reflections present within the coherence length of the light source will generate interference fringes that can be used to locate the position of reflections in the device under test. One of the earliest implementations of LCI was as a displacement sensor as early as 1984 [17].

The beginnings of OCT can be traced back to techniques based on LCI such as optical coherence domain reflectometry (OCDR) and optical frequency domain reflectometry (OFDR). Originally, both techniques were employed as alternative methods for measuring waveguides and fiber optic systems [18-20] [21, 22] due to the ability to obtain high resolution measurements in a non-destructive manner.

Optical coherence domain reflectometry employs LCI with path-length scanning in the reference arm and was able to achieve a resolution of a few tens of microns. In addition, optical coherence domain reflectometry formed the basis for time-domain OCT (TD-OCT), which was presented in the landmark paper in 1991 [23]. This would be the

first time that such techniques were employed successfully in a biomedical application to form images to visualize structural layers in *ex vivo* human retina and coronary artery.

Optical frequency domain reflectometry forms the basis for what is now known as optical frequency domain imaging (OFDI) or swept source OCT (SS-OCT). Optical frequency domain reflectometry differs from optical coherence domain reflectometry by employing a wavelength swept laser in lieu of a broadband laser source and a fixed path-length difference was maintained in place of scanning the reference arm.

SS-OCT is just one of the two categories of Fourier domain OCT systems. The second category is spectral domain OCT (SD-OCT). SD-OCT is another configuration that grew out of a technique called coherent radar where in place of a wavelength swept laser, a broadband light source was used and the interference signal was collected with a high resolution spectrometer. While both SS-OCT and SD-OCT differ in the light sources and detection schemes, both OCT configurations collect interference fringes in the frequency domain and require a Fourier transform to relate to the spatial domain to obtain a depth profile (or A-line).

1.4.2 SD-OCT

SD-OCT was naturally derived from coherent radar [24, 25] and spectral interferometry [26, 27] techniques from which came spectral radar for OCT [28, 29].

As mentioned earlier, SD-OCT systems employ a Michelson or modified Michelson interferometer with a fixed path length delay in the reference arm and a high spectral resolution spectrometer as a detector. Before the development of many modern high speed swept sources, SD-OCT had a significant speed advantage since it collected all wavelengths simultaneously through spectral dispersion.

Currently, SD-OCT systems have been demonstrated with A-scan rates up to 500,000 A-lines-per-second [30, 31] at 800 nm, up to 120,000 A-lines-per-second at 1050 nm [32]and up to 47,000 A-lines-per-second at 1300 nm [33]. SD-OCT systems easily lend themselves to being implemented at 800 nm due to the number of commercially available components such as high speed cameras limiting the number of high speed SD-OCT systems at 1300 nm. Furthermore, SD-OCT systems are more popular today due to availability of a wide variety of broadband sources such as superluminescent diodes (SLDs), supercontinuum, solid state lasers, which will be discussed in more detail in chapter 2.

1.4.3 SS-OCT

As mentioned earlier SS-OCT uses various types of tunable wavelength sources to perform frequency swept interference measurements on an illuminated sample. One of the first implementations of SS-OCT was as early as 1990, though it was not employed for biological imaging [34]. Employing a swept source was thought to be simpler than using a broadband light source due to coupling into a single mode fiber and intricate alignment of a mode-locking laser cavity. Wavelength swept sources have been implemented in many ways over the years, such as, temperature tuned neodymium-doped yttrium aluminum garnet (Nd:YAG) lasers at 1300 nm [34], semiconductor sources [35], superluminescent diodes with a grating and galvanometer mirror to scan wavelengths [36] and tuning laser cavities [37, 38].

Currently, SS-OCT is one of the most popular OCT configurations due to the ability to perform high-speed, real-time imaging with A-scan rates from up to 43,000 A-lines-per-second at 800 nm [39-41], up to 400,000 A-lines-per-second at 1050 [42, 43]

and hundreds to millions of A-lines-per-second at 1300 nm [44-47]. Ultrahigh A-scan rates have also enabled ultrahigh speed endoscopic imaging at 1300 nm with reported frame rates up to 3200 frames-per-second [48-51].

SS-OCT systems have been implemented with single Michelson interferometers or dual interferometers with balanced detection. Performance of balanced detection scheme in SS-OCT has led to a significant signal-to-noise (SNR) advantage over SD-OCT due to the fact that SD-OCT employs a camera based spectrometer as its detector. The high speed camera is the limiting factor for the overall A-scan rate as well as the sampling resolution and detection sensitivity leading to a significantly higher sensitivity roll-off along the imaging depth when compared with SS-OCT [40, 42].

1.4.4 Applications of OCT in Biomedical Imaging

The previous sections focused on a brief history and introduction of OCT, specifically FD-OCT in SS-OCT or SD-OCT format. OCT as a whole since its conception has been applied to biomedical imaging of many different parts of the human body. OCT has evolved since its earliest demonstrations into a high resolution, high-speed, non-invasive, and non-contact imaging modality. This section will discuss some of the key applications that OCT has been applied to since the initial demonstration in 1991.

Ophthalmic imaging, specifically visualization of posterior eye structures such as the retina, optic disc and retinal nerve fiber layer (RNFL) were one of the first biological applications of OCT in the first landmark paper on OCT in 1991 [23]. Since 1991, ophthalmic imaging in the field of OCT has grown significantly and has been highly developed. One of the reasons that OCT has been so well adapted to ophthalmic imaging is due to the fact that it can perform non-invasive, non-contact imaging and quantify

structure thickness. These abilities makes it well suited to imaging and measuring the thickness of RNFL in glaucoma patients were elevated intraocular pressure can compromise the integrity of the RNFL. In addition to posterior eye segments, OCT has also been used to characterize the properties of anterior eye segments such as the cornea, crystalline lens, anterior angle region and iris [52-55]. Finally aside from characterization and measurements of eye segments, OCT is also able to be used for early diagnosis for diseases such as macular edema and age related macular degeneration (AMD) [56].

OCT was also readily adapted to dermatologic imaging due to the ease of accessibility and inability of NIR wavelengths to penetrate deep into the body. OCT is a powerful tool for dermatologic imaging because it provides a high resolution, non-contact imaging method to study milestone changes in wound healing [57] without disruption of the process. Aside from monitoring changes, OCT has been shown to be able to detect skin lesions in a variety of conditions and diseases such as hemangiomas, pemphigus diseases and epithelial skin cancer [58].

Initial efforts in the field of OCT used benchtop systems since it was relatively easy to access structures within the eye and skin, however in order to image structures deep within the body it was necessary to develop a way to deliver light into the body for imaging. In conjunction with fiber-optic interferometers, endoscopic OCT was first introduced in 1996 [59] to visualize a human vein *in vitro*. This was a major breakthrough in the field of OCT, mapping a way to perform imaging of internal organs and since this time an entire subfield of OCT has been devoted to the development of endoscopic OCT probes and portable OCT systems as well as exploration of endoscopic OCT for use in surveillance, guidance and diagnosis.

One active area of research is intravascular imaging of coronary arteries to visualize thin fibrous caps [60] and identify intimal hyperplasia which leading to restenosis [61]. Another area of interest in cardiovascular imaging is evaluating stent placement in coronary arteries. The significantly higher axial resolution of OCT compared with intravascular ultrasound (IVUS) has proved to be a significant advantage to be able to more clearly delineate tissue prolapse, dissection and irregularity of stent struts [62] Cardiovascular imaging with endoscopic OCT is challenging due to the fact that endoscopic probes need to be small enough to fit within the coronary arteries and that blood results in significantly high attenuation to NIR wavelengths. Overcoming these challenges has easily enabled endoscopic OCT to be lent to other areas of the body such as pulmonary imaging.

Pulmonary imaging has been another active field of study in the OCT world. Recently there have been groups interested in studying the changes in airway wall in obstructive lung disease (OLD) and chronic obstructive pulmonary diseases (COPD). It is currently believed that airway smooth muscle in small airways (<2 mm) may be the main players in OLD. Since it has been difficult to access small airways over the years, OCT provides a quaint solution to study and understand airway wall morphology such as airway wall remodeling [63] and identification of malignant airways via thickened mucosa [64].

In addition to cardiovascular and pulmonary imaging, gastrointestinal (GI) imaging is another large area of active research in the field of OCT, specifically for guidance and surveillance of morphological changes in tissue structures that could lead to cancers. Barrett's esophagus (BE) is a condition where the stratified squamous cells

lining the epithelium of the esophagus change into columnar cells due to breakdown and regrowth of the epithelial lining from chronic gastroesophageal reflux (GERD). BE is thought to be a precancer state where a subset of patients exhibiting dysplasia (~14% with low grade dysplasia and ~34% with high grade dysplasia) will develop esophageal adenocarcinoma (EAC) [65] making surveillance and guided biopsy procedures exceedingly important. Furthermore, OCT has been shown to detect subsquamous BE along with normal tissue structures [66] proving its importance in detection of BE and EAC as well guiding and assessing biopsy or ablative treatment procedures [67].

While there has been a significant focus on the upper GI tract in OCT, there has also been some research done on imaging of the lower GI tract. OCT imaging has been shown to delineate normal tissue microarchitecture in the colonic mucosa [68] as well as visualize disruption of normal architecture in colon cancer [69, 70] and inflammatory bowel diseases (i.e. ulcerative colitis, Crohns disease) [71-73].

1.5 *Current Trends in OCT*

As discussed in the previous section, there are many subfields within the field of OCT. Some of these subfields are dedicated to engineering efforts to expand and enhance OCT technologies and others are dedicated to the study of biomedical applications. These two avenues of research enable one another. In order to provide high quality imaging of internal organs *in vivo*, it is necessary to develop high quality OCT systems. One of the most interesting avenues of research today is achieving ultrahigh axial resolution endoscopically while performing high speed imaging.

Ultrahigh axial resolutions (< 3.0μm) were able to be achieved as early as 1999 using 800 nm mode locked lasers [74] and 2001 with continuum generation [75]. It was

known that in order to optimize the axial resolution it was necessary to take advantage of the quadratic relationship between the central wavelength and the axial resolution, with a broadband source. Thus, moving to OCT systems at 800 nm yielded the highest known axial resolutions of 3 μm and 2.5 μm in air, respectively.

Achieving ultrahigh axial resolution endoscopically, however, still had many challenges to overcome due to the due to the lack of commercially available fiber-optic components and significant chromatic aberration issue at 800 nm. The first 800 nm endoscopes were demonstrated for ultrahigh resolution imaging of *in vivo* mouse colon [76, 77] in 2006. These endoscopes were not able to perform circumferential scanning (only pull-back) limiting widespread use in OCT imaging. Nearly a decade later an ultrahigh resolution OCT catheter for volumetric imaging was introduced [78], enabling high resolution OCT to be performed in internal organs *in vivo.* While this paper demonstrated an ultrahigh resolution catheter with volumetric imaging, the imaging speed was limited to 10 frames-per-second or less due to the mechanical instability of the home-built fiber-optic rotary joint for the proximal scanning catheter. In order to be able to push the technology towards translational and clinical imaging *in vivo* it will be necessary to address the challenges of high speed scanning for ultrahigh resolution endoscopic imaging.

1.6 *Scope of Dissertation*

The goal of this dissertation is develop ultrahigh resolution and high speed Oct endoscopy technology operating at 800 nm and demonstrate its capability for endoscopic assessment of tissue microstructure *in vivo*. This thesis comprises of the technological

development of an ultrahigh resolution, high-speed OCT system at 800 nm and some of its biomedical applications with potential for clinical imaging.

The first part of this dissertation will focus on technological development while the latter part will address the applications of this technology and potential for future clinical use. Chapter 2 will lay the foundation for the development of the high resolution endoscope by discussing the 800 nm SD-OCT system. The interference signal in an SD-OCT system as well as the system components such as a light source, interferometer and imaging spectrometer will be described with emphasis on the linear-wavenumber spectrometer designed. Chapter 3 will describe the challenges and associated solutions to overcome the challenges in order to implement a high-speed, ultrahigh resolution distal scanning endoscope at 800 nm. Chapter 4 will introduce some image processing algorithms implemented in conjunction with the ultrahigh resolution imaging system. Specifically an algorithm developed to correct for non-uniform rotational distortion (NURD) which can occur in distally scanned systems is described.

Finally chapters 5 and 6 will detail the investigation of this ultrahigh resolution endoscopic OCT system at 800 nm for visualization of microstructural details in pulmonary imaging in sheep and colorectal cancer imaging in mice. Chapter 5 will focus on imaging small airways in sheep and the efforts to delineate and directly visualize airway smooth muscle by correlating endoscopic OCT images with histological sections of the same airway. Chapter 6 will focus mainly on the application of this ultrahigh resolution imaging system to study longitudinal morphological changes in a colon cancer model in mice *in vivo*. Specifically by inoculating mice with enterotoxigenic *Bacteriodes fragilis* (ETBF) in APC^{Min} mice, the colon undergoes many changes including chronic

colitis which can in turn lead to growth of polyps which can lead to tumors within several weeks.

In addition to these applications, chapter 7 and 8 will focus on other OCT projects. Chapter 7 is dedicated to image processing algorithms that have been widely developed for vascular visualization will be briefly discussed with some imaging results in tumor angiogenesis in a nude mouse ear and a middle cerebral artery occlusion stroke model in mice. Chapter 8 will describe a multimodal endoscopic imaging with swept source OCT (SS-OCT) and fluorescence imaging with results in *ex vivo* rabbit esophagus.

Chapter 2 SD-OCT System

2.1 *Introduction*

This chapter will focus on spectral domain optical coherence tomography (SD-OCT). The first section in this chapter will describe light tissue interactions which will be discussed prior to a brief derivation of the generation of an OCT A-line (depth profile). The latter part of the chapter will introduce SD-OCT and focus on the decisions required to appropriately choose individual components that makeup an SD-OCT system. Specifically, there will be a discussion on the requirements of a light source, the variety of light sources currently available, and the requirements for an imaging spectrometer. Finally, the chapter will be concluded with a brief outlook towards Chapter 3.

2.2 *Light Tissue Interactions*

Scattering and absorption are the most fundamental light-tissue interactions with which an image can be created by an optical imaging modality. This section will briefly discuss optical scattering as related to biological sample imaging.

Scattering behavior depends greatly on the size of the object with respect to the wavelength. For example, Mie scattering is the dominant mode of scatter when the wavelength is comparable to the object size and Rayleigh scattering is dominant when the object size is much larger than the wavelength.

In biological tissues, scattering is dependent on the composition of the tissue, i.e. water, fat, oxy- or deoxyhemoglobin, melanin, or in more general terms, types of cell

layers and specific organelles [79]. OCT typically employs a broad range of near infrared (NIR) wavelengths from 800 to 1550 nm and scattering that contributes to OCT backscattered light occurs from specific organelles, cells and cell layers where the range of sizes vary greatly (i.e. cell nuclei ~5-10 μm, mitochondria 0.1 – 2 μm, cell membranes 6-10nm [80]), so we characterize OCT as operating in the Mie scattering regime.

The Beer-Lambert law describes the relationship between scattering and absorption in the sample to the amount of light transmitted through it:

$$I(d) = (1 - R_F) I_0 e^{-u_t d}. \tag{2.1}$$

In equation 2.1, I_0 is the intensity of the incident beam, R_F is the coefficient of Fresnel reflection and u_t is the total attenuation coefficient. The term of interest in this relationship is the total attenuation coefficient, u_t. The total atenuation coefficient is dependent on the density of particles and the extinction cross-section which is a combination of the scattering and absorption cross-sections. Finally, the scattering and absorption cross-sections are governed by the size and shape of the tissue constituents causing scattering, such as the aforementioned organelles as well as the chromophores and the refractive index mismatch which surrounds the tissue constituents.

The type of scattering of interest in OCT is backscattering, essentially the portion of light that is scattered in the backwards direction (towards direction of illumination). In this case, another important parameter is the scattering anisotropy factor, *g,* which describes the scattering directionality (i.e. $-1 \leq g \leq 1$ where -1 represents total backward scattering, 1 represents total forward scattering and 0 is isotropic scattering (Rayleigh

scattering)[80]) . In general, most biological tissues have a high a forward scattering distribution with an anisotropy factor less than or very close to 1 [80, 81].

Now we can consider u_b the backscattering coefficient which is defined as $\mu_b = \rho\sigma_b$, where ρ is the density of particles and σ_b is the backscattering cross-section. The backscattering cross-section is given by [82, 83]:

$$\sigma_b = \frac{4\pi|X(180°)|^2}{k^2}, \qquad 2.2$$

and is dependent on $X(180°)$ which is the vector scattering amplitude or the phase scattering function for the particle for a wavenumber, *k.* The corresponding backscattered energy will be given by $W_{sca} = I_i\sigma_b$ [82]. Where the total amount of energy scattered is W_{sca} and I_i is the incident intensity. Although, upon first inspection Equation 2.2 seems to show that the backscattering increases with increasing wavelength, this is a misconception because the phase scattering function is complicated and is a function of the wavenumber and is highly dependent upon the size particle.

In essence, the scattering efficiency increases with the size parameter $x=ka$, where k is the wavenumber and *a,* is the radius of the particle [81]. This is known to result in an improved image contrast for OCT at shorter wavelengths. The tradeoff for having an improved imaging contrast is that increased scattering results in shallower penetration depth compared with longer wavelengths.

2.3 *Generation of an OCT A-line [84]*

The fundamental unit in OCT is an axial line or an A-line. An A-line is the intensity distribution of backscattered light, due to refractive index mismatches at sample

interfaces. OCT employs low coherence interferometry (as discussed in the introduction) to generate an interference signal which will ultimately result in the intensity distribution that is coined an “A-line”.

In OCT, the interference signal is generated from the superposition of planar waves returning from two arms of an interferometer, the sample and reference arm. An example of a fiber-optic SD-OCT system with a fiber-optic Michelson interferometer is shown in Figure 2.1. The Michelson interferometer is an optical coupler with a 50/50 splitting ratio. Interference will occur when light from the sample and reference arms are reflected back through the coupler towards the detector. In order to obtain an interference signal with a low temporally coherent light source, the optical path length difference between the sample and reference arms must be less than the coherence length of the light source.

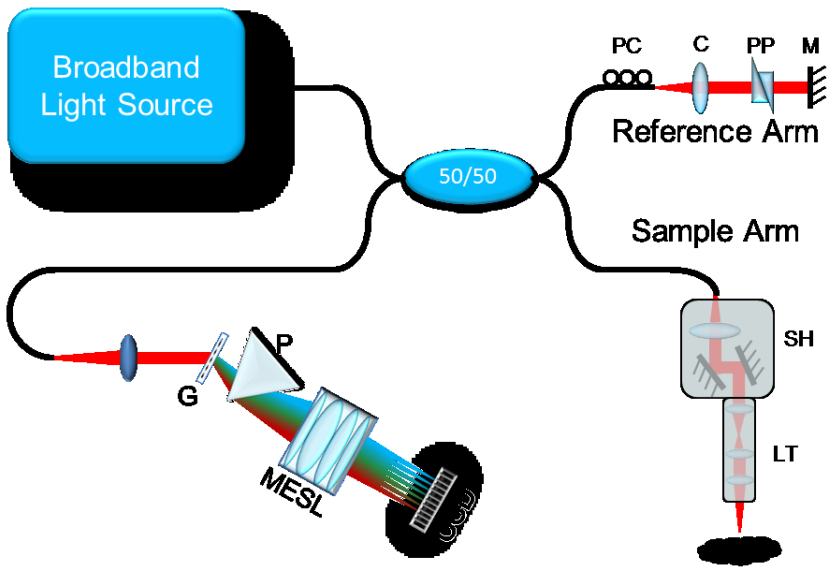

Figure 2.1 Generic schematic of SD-OCT system.

Schematic of Michelson interferometer based OCT system. Reference

arm: PC: polarization controller; C: collimating lens; PP: prism pair; M: mirror. Sample arm: SH: scan head; LT: lens tube.

The system in Figure 2.1 shows a typical setup for a hand-held probe. The sample arm consists of a scan head and a lens tube for imaging. The scan head incorporates two galvanometer mirrors to scan the laser beam in the X and Y directions for three dimensional scanning. The reference arm has a collimating lens, prism pair and a mirror. Since this is an FD-OCT system, the reference arm is stationary at a fixed path length difference. In order to compensate for path length mismatch, the reference arm has incorporated a prism pair.

In order to gain a better appreciation for the origin of the interference signal and corresponding depth profile, the relationships shall be derived in this section. We shall begin with the electric field of the light source, $E_{LS}(k) = E_0(k)e^{-j(kz-\omega t)}$, where $E_0(k)$ is the complex amplitude of the electric field. The corresponding intensity can be written as, $I \propto |E_{LS}(k)|^2$, where the intensity is proportional to the square of the electric field. Using this convention, the electric field returning to the detector from the reference arm can be written as,

$$E_R(k,t) = r_R E_0(k)e^{j(2kz-\omega t)}. \qquad 2.3$$

In Equation 2.3, r_R, is the reflectivity of the mirror in the reference arm and is assumed to be perfectly reflective ($r_R = 1$). Due to the fact that the light travels to and from the

optical coupler and reference mirror, there is a factor of 2 in front of kz. Similarly the electric field returning to the detector from the sample arm can be written as:

$$E_s(k,t) = E_0(k)\int r_s(z)e^{j(2kz-\omega t)}dz. \tag{2.4}$$

Here, $r_s(z)$ represents the spectrum of backscattered light from the sample and $E_s(k,t)$ is the sum of the electric field of light returning from different depths in the sample.

The superposition of the electric field from the reference and sample arm as measured by the detector is:

$$\begin{aligned} E_D(k,t) &= E_R(k,t) + E_s(k,t) \\ &= E_0(k)\left\{r_R e^{j(2kz-\omega t)} + \int r_s(z)e^{j(2kz-\omega t)}dz\right\} \end{aligned} \tag{2.5}$$

The measured quantity at the detector is not the electric field, but, the intensity $I_D(k) \doteq \langle Re\{E_D(k,t)\}^2\rangle_T$, where T is the exposure time of the camera. Hence, the detected interference signal is:

$$\begin{aligned} I_D(k) = S_0(k)\Big\{r_R^2 &+ \iint r_s(a)r_s(b)e^{j2k(a-b)}dadb \\ &+ \int r_R r_s(z)e^{-j2k(z_r-z)}dz + \int r_R r_s(z)e^{j2k(z_r-z)}dz\Big\}. \end{aligned} \tag{2.6}$$

In SD-OCT, this detected interference signal will be spectrally dispersed throughout the spectrometer, with respect to wavelength or wavenumber (in the case of a linear wavenumber spectrometer). The spectrally dispersed signal is comprised of the sum of interference signals at all the path lengths within the sample where backscattered light returns to the detector. In order to obtain the depth resolved information from the

detected interference signal, the Fourier transform must be applied to the detected interference signal, $I_D(z) = FT\{I_D(k)\}$, where, z, is depth position within the sample. The Fourier transform will be able to plot the frequency distribution with respect to the imaging depth, where higher frequencies correspond to a larger path length difference. After some algebraic manipulations we can obtain the form for an OCT A-line:

$$I_D(z) \propto \underbrace{\delta(z) r_R^2}_{DC} + \underbrace{\int r_s(a) r_s(a-z) da}_{Autocorrelation} + \underbrace{r_r r_s(z_R + z) + r_R r_s(z_R - z)}_{Depth\ Profile\ (Mirror\ Images)}. \qquad 2.7$$

Here we approximate $\widehat{S_0}(z) = FT\{S_0(k)\} \approx \delta(z)$ to better understand how the depth profile arises from $I_D(z)$. In Equation 2.7 there are four terms, the first term $\delta(z) r_R^2$ is a large term at z=0. This term is often coined the DC signal in SD-OCT and is eliminated by acquiring the reference arm spectrum while blocking any light returning from the sample arm and subtracting it from the interference signal. The second term, $\int r_s(a) r_s(a-z) da$, is the autocorrelation of the sample reflectivity profile which is centered around z=0 path length. The last two terms are mirror images of one another and either could be used to recover the depth profile, $r_s(z)$. It is important to note that each mirror image is translated to either the left or the right of z_R, respectively. In order to avoid aliasing, it is important to ensure that $r_s(z) = 0$ for $z < z_R$, physically this means that is that the reference arm is shorter than the sample arm (when the sample arm is at the focal plane of the probe).

2.4 *Key parameters*

2.4.1 Axial Resolution, Spectral Shape, Side Lobes, Dispersion Mismatch

The axial resolution in OCT determines the depth resolving capabilities of the system and the corresponding point spread function (PSF) is the shape of the beam interrogating the sample. In order to clearly visualize tissue microstructures of interest it is important to have an axial PSF that has a small full-width-at-half-maximum value and minimal side-lobes. The axial resolution is calculated as:

$$\delta_z = \frac{2\ln(2)}{\pi} \cdot \frac{\lambda_0^2}{\Delta_\lambda}, \tag{2.8}$$

if the light source is assumed to have a Gaussian shape with a FWHM spectral bandwidth of Δ_λ, and a central wavelength of λ_0. The axial PSF is given by the following relation [85]:

$$I(\Delta z) \propto Re\left\{\int S(k) e^{ik\Delta z} dk\right\}. \tag{2.9}$$

Since the axial PSF is proportional to the Fourier transform of the source spectrum, non-Gaussian spectral shapes result in side-lobes that will cause ghost reflections and mask reflections near strong reflectors [85, 86]. Thus having a high axial resolution with side-lobes can significantly deteriorate image quality by making it appear "fuzzy". Unfortunately, many sources for OCT have non-ideal source spectra, however these sources can still be used by performing spectral shaping.

Spectral shaping can be performed in two ways, by physically altering the spectral shape through optical components or through digital spectral shaping after acquisition. Each method has its own advantages and disadvantages. Most notably, hardware or

optical spectral shaping can require complicated equipment and lead to loss of power prior to the sample arm. The main advantage to this approach is that there would be minimal axial PSF broadening and a significant reduction of the side lobes [86].

Alternatively, digital spectral shaping can be done by forming a spectral correction curve to reshape the interference signal into a nearly Gaussian shape. While this method requires no additional instrumentation, it costs an extra computational stage. One of the downsides to this method is that side-lobe suppression through digital methods can lead to a broader axial PSF and higher noise floor [85].

Other factors that can equally influence the axial resolution are the optical path length or dispersion mismatch between the sample and reference arms. A major focus of this dissertation is endoscopic imaging and in the case of endoscopic imaging there are many different materials in the sample arm, (optical fiber, glass rod, gradient index (GRIN) lens, plastic tubing, and air space) making it challenging to adequately match the optical path length in the reference arm. The equation below is the Taylor series expansion of the propagation constant, $\beta(\omega)$ [87].

$$\beta(\omega) = \underbrace{\beta(\omega_0)}_{phase\ velocity^{-1}} + \underbrace{\left.\frac{\partial\beta}{\partial\omega}\right|_{\omega_0}(\omega-\omega_0)}_{group\ velocity^{-1}} + \underbrace{\left.\frac{1}{2}\frac{\partial^2\beta}{\partial\omega^2}\right|_{\omega_0}(\omega-\omega_0)^2}_{group\ velocity\ dispersion\ (GVD)} + \underbrace{\left.\frac{1}{6}\frac{\partial^3\beta}{\partial\omega^3}\right|_{\omega_0}(\omega-\omega_0)^3}_{third\ order\ dispersion\ (TOD)} + \cdots \quad 2.10$$

The first term is propagation constant at the central frequency, ω_0, and is the reciprocal of the phase velocity. The second term is the inverse of group velocity which is the speed at which the wave packet travels. The third and fourth terms are second and third order dispersion which cause symmetric and asymmetric broadening of the axial PSF, respectively. These terms need to be compensated through physical or digital dispersion compensation methods.

In the case of physical dispersion matching, an example is shown in Figure 2.1, where a prism pair is inserted into the reference arm. Prism pairs are available in many different materials, and can be inserted to match material dispersion (GVD) in the reference arm for materials that have been inserted within the sample arm. Even higher orders of dispersion can be matched with an optical delay line in the reference arm

Digital or numerical dispersion compensation has been performed in a variety of ways from the addition of a phase term to the interference signal [87], using a fractional Fourier transform [88], iterative depth correction [89] and depth variant kernel correlation of depth scan [90] .

At longer wavelengths such as 1300 nm where it is a known zero-dispersion point for optical fibers, dispersion is often times not a significant issue impeding axial resolution, however at shorter central wavelengths such as 800 nm where refractive index changes much more rapidly, dispersion can significantly contribute to deteriorating axial resolution and image quality, and must be compensated.

2.4.2 Lateral Resolution

One of the great features of OCT is the fact that the axial and lateral resolutions are decoupled. The lateral resolution in OCT depends solely on the imaging optics used in the sample arm, whether that is an endoscope, benchtop system, or a hand held probe. The lateral resolution is given by:

$$\delta_x = \frac{4\lambda_0}{\pi} \cdot \frac{f}{d}. \tag{2.11}$$

Here, λ_0, is the central wavelength of the light source, *f*, is the focal length of the objective lens and *d,* is the spot size of the beam on the objective lens.

2.5 *Light Source*

In order to choose the appropriate light source for an OCT engine, several factors need to be considered, such as the choice of central wavelength, spectral bandwidth, spectral shape, output power, and noise. In the following sections these parameters are discussed in further detail.

2.5.1 Wavelength

OCT light sources are available at a wide range of wavelengths available in the near infrared (NIR) region around 800 nm, 1060 nm and 1300 nm, each of which have its own advantages. The choice of central wavelength for OCT is generally depends upon the application, desired axial resolution and imaging depth.

Since scattering is higher at shorter wavelengths, sources at 800 provide an improved imaging contrast at the cost of limited penetration depth. Additionally, lower water absorption at this wavelength is beneficial for posterior eye imaging where the long path length of the eye would not pose a concern. Furthermore, sources at 800 nm are able

to achieve an overall higher axial resolution for a given bandwidth, due to the quadratic dependence of the axial resolution on the central wavelength.

Another range of sources are readily available at 1300 nm. Although water absorption is higher, the total optical attenuation is low enough to provide sufficient image contrast for OCT while enabling greater depth penetration. Additionally, the wide variety of off-the-shelf optical components, assemblies, and light sources enable 1300 nm imaging to be easy to implement.

Finally, another promising wavelength range that is not as frequently used is 1060 nm. 1060 nm may provide the optimal compromise between high scattering and low water absorption to provide improved image contrast (compared to 1300 nm) and a greater depth penetration (compared to 800 nm). In this dissertation, we aim to achieve ultrahigh resolution imaging and have chosen to take advantage of light sources at 800 nm which will be discussed further below.

2.5.2 Power

The signal-to-noise ratio in an OCT system is related to the available (or permissible) source power, i.e. [91]:

$$\frac{SNR v_s}{P_s L_C} = const. \tag{2.12}$$

SNR represents the signal-to-noise ratio, P_S is the maximal power, v_S is a parameter proportional to the scanning rate or imaging speed, and L_C is the coherence length of the light source. The key outcome of this relationship is that in order to preserve the SNR at higher image acquisition rates, the optical power must be increased. This point is

especially critical in endoscopic OCT systems where dwell time decreases with increasing frame rate, making it important to increase the incident power on the sample.

2.5.3 Types of Sources

The first light source used to demonstrate OCT was a superluminescent diode (SLD) with a central wavelength around 830 nm [23]. Since 1991, a variety of light sources have been discovered and developed for OCT. Appropriate sources range from femto-second light sources, semiconductor sources, supercontinuum sources, to swept sources for swept source OCT. In this chapter we will focus mainly on SD-OCT and restrict our discussion to femtosecond light sources, semiconductor sources (superluminescent diodes) and supercontinuum sources (SC). The three major characteristics that will be focused on are the ability to provide a broad spectral bandwidth, the ability to provide sufficient optical power, and the relative size or ease of use.

2.5.3.1 Superluminescent diode (SLD)

The SLD was the first to be demonstrated for OCT partially due to availability and ease of use [23]. The major advantages of choosing SLDs as light sources are that they are turnkey, inexpensive, compact, and can be combined to provide broad spectral bandwidths [92] around many different wavelength bands from 800nm -1600 nm. These abilities have also led to widespread use of SLDs in commercial systems i.e. Carl Zeiss [93, 94] and Leica Microsystems [95].

Although SLDs have been widely employed, the lack of optical power represents a major disadvantage preventing SLDs from further widespread use in non-ophthalmic applications and endoscopic imaging systems where high speed scanning is a priority.

According to Equation 2.12, as A-line rates increase, to maintain SNR it is important to increase the source power, making the low output power of SLDs a disadvantage that would be solved with femtosecond and supercontinuum lasers or swept sources and SS-OCT in the lab and commercially.

2.5.3.2 Solid State and Femtosecond Light Sources

Femtosecond lasers employed for OCT are usually mode-locked laser systems that emit high power optical pulses with a duration of femtoseconds. It was quickly discovered that mode-locked femtosecond lasers are able to provide broad bandwidths with high optical power and superb stability, making them a popular option for OCT light sources. Using Kerr-lens-mode-locked (KLM) Ti:Sapphire lasers, broad spectral bandwidths and resulting high axial resolutions of 3.7 μm [96] and 1.5 μm [97] were achieved. In addition to femtosecond sources at 800 nm, KLM mode-locking was applied to Cr^{4+}:Forsterite to generate a broad spectral bandwidth around 1.28 μm achieving an axial resolution of 5.7 μm, demonstrating another biologically relevant optical window for imaging [98].

Unfortunately, due to the bulky and complicated setup of mode-locked femtosecond light sources, the technology has not been applied to commercial systems. Nevertheless, these sources have been employed in numerous benchtop [96-98] and some endoscopic OCT systems [76-78, 99].

2.5.3.3 Supercontinuum

Supercontinuum (SC) light sources present an interesting alternative to SLDs and femtosecond light sources as they can achieve broad spectral bandwidths with high

optical power at the cost of increased laser noise. SC sources were initially demonstrated in 2001 for ultrahigh resolution imaging of hamster cheek pouch [75]. Since 2001 there have been many developments leading to compact, turnkey SC sources that are readily available from companies such as NKT Photonics (www.nktphotonics.com), Fianium (www.fianium.com), and YSL Photonics (www.yslphotonics/en).

The major drawback of SC sources is the increased laser noise and suboptimal spectral shape, however the advantages in power and spectral bandwidth of SC light sources generally outweigh by the aforementioned disadvantages. With more SC sources becoming commercially available, understanding how to minimize noises due to SC generation in an OCT system became more necessary, and it was shown that as long as the source are operated within the shot noise limited range of the OCT system image quality comparable with femtosecond light sources can be achieved [100].

2.6 *Interferometer*

The interferometer is perhaps the most important component in the OCT system, without which an interference signal could not be acquired. In order to construct an endoscopic OCT system, it is important to choose components that could be easily translated into a portable form so that it can be translated for use in a clinical setting.

There are many different interferometer configurations for OCT, some of which are Michelson (MI), Mach-Zehnder (MZI), modified Michelson and Linnik. The Michelson interferometer was the first employed for time-domain OCT in 1991[23]. Later, a version of the Mach Zehnder interferometer that performed OCT imaging using trans-illumination of the sample was introduced[101] and became more popular due to its

ability to conserve optical power compared to a Michelson interferometer[102, 103]. Along the same premises, a modified Michelson interferometer was introduced. The modified Michelson interferometer employed an optical circulator in between the light source and interferometer so that the interference signal back-reflected towards the light source can be redirected to one arm of a balanced detector[103]. Around the same time, full-field optical coherence tomography using a Linnik interferometer was demonstrated[104, 105]. A Linnik interferometer is a free-space Michelson interferometer with the same optics in the reference and sample arm, thus minimizing chromatic aberrations and other optical aberrations.

Moving forward, we will focus on two of the main configurations, Michelson and Mach-Zehnder, which are shown in Figure 3.6 A and B respectively. 800 nm SD-OCT systems usually employ a Michelson interferometer for several reasons, 1) broadband optical components such as circulators for 800 nm are not readily available in the market and 2) balanced detection is not possible with a spectrometer as the detector[1].

[1] Strictly speaking with the use of one spectrometer balanced detection is not possible, however it has been shown that using two spectrometers 106. Kuo, W.C., et al., *Balanced detection for spectral domain optical coherence tomography.* Optics express, 2013. **21**(16): p. 19280-19291., balanced detection can be performed.

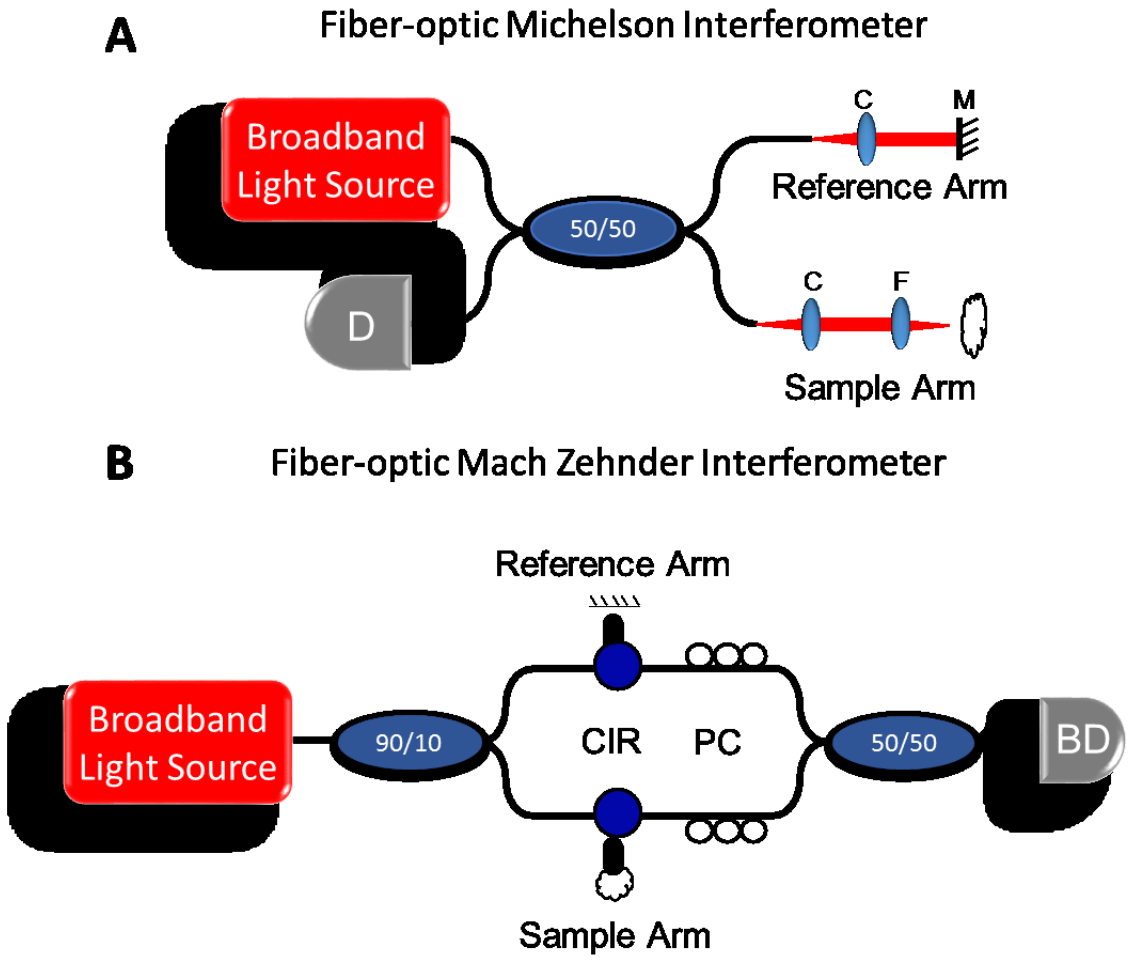

Figure 2.2 OCT interferometer configuration.

(A) An example of a 50/50 fiber-optic Michelson interferometer. The broadband light is split into the reference and sample arm by the coupler and returning light will interfere at the 50/50 coupler before being detected by the detector arm. (B) An example schematic of a fiber optic Mach-Zehnder interferometer. The interferometer is a 90/10 optical coupler which splits the broadband light into the reference and sample arms. Each arm has a circulator where the light leaves the interferometer and returns to another optical coupler

(50/50) where the light from sample and reference arm are combined and split in half and sent to a balanced detector. (A) C: collimating lens, M: mirror, F: focusing lens and D: detector. (B) CIR: circulator, PC: polarization controller, and BD: balanced detector.

2.7 *SD-OCT Spectrometer*

In SD-OCT, an imaging spectrometer is used to spectrally disperse the interference signal in space and detect all wavelengths simultaneously. In order to be an effective detector, the spectrometer must be able to accommodate broad spectral bandwidths and perform high speed acquisition. The ability to detect broad spectral bandwidths will be determined by the spectrometer design and the high speed acquisition shall depend upon the acquisition speed of the camera, all of which shall be discussed in further detail in this section.

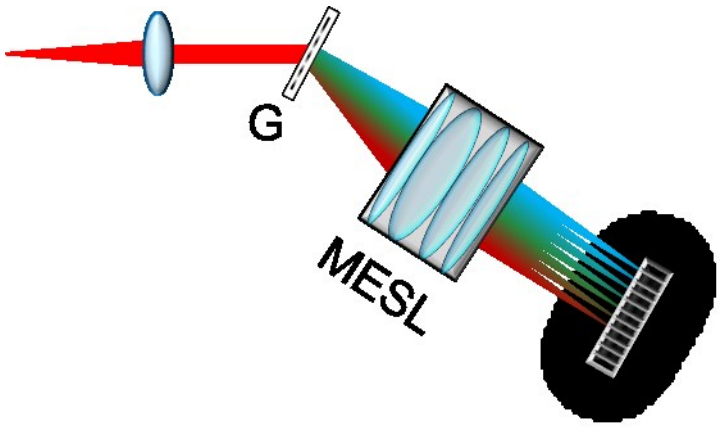

Figure 2.3 Example of linear-wavelength spectrometer design.

G: volumetric transmission grating, MESL: multi-element scan lens,

CCD: linear CCD array.

2.7.1 Spectrometer Design, Signal Roll-Off, Calibrated Imaging Depth

An OCT imaging spectrometer is a high spectral resolution imaging spectrometer, which is schematically shown in Figure 2.1 (linear wavenumber spectrometer) and Figure 2.3 (linear wavelength spectrometer). The interference signal acquired from the interferometer is generally coupled into the spectrometer through a single mode fiber. The light will first be collimated using an achromatic doublet to minimize chromatic aberrations and will then sent through a dispersive optical element such as a transmission diffractive grating as shown in Figure 2.3.

$$\theta_m = \sin^{-1}\left(\frac{m\lambda}{d} - \sin\theta_i\right) \tag{2.13}$$

Equation 2.13 is the grating equation where d is the groove separation of the grating, m is the order of diffraction, λ is the wavelength of light, θ_i, is the angle of incidence upon the grating, and θ_m is the diffraction angle for wavelength λ, with a grating whose groove separation is d.

After the diffraction grating a lens is installed to focus all wavelengths to the same focal plane on the sensor array. A scan lenses such as F-theta lenses are usually preferred due to the fact that the position of the focal spot on the focal plane is dependent upon the focal length of the lens and off-axis angle of incidence. The focusing lens must be its able to compensate or minimize chromatic aberrations due to the broad bandwidth of the light source and ability to maintain a flat focal plane such that all the wavelengths can be adequately detected by the pixels on the image sensor (i.e. linear CCD or CMOS array).

Finally, a linear sensor array is installed to acquire the spectrally dispersed interference signal. The diffraction grating will determine the spectral resolution while the lens will determine the spot size and allowable bandwidth. In an SD-OCT system, the sampling frequency for the interference signal is a fixed by the spectral resolution and camera pixel size. This fixed sampling frequency determines the highest measurable fringe frequency which corresponds to the maximum imaging depth, $z_{RD} = \frac{\lambda^2}{4n\delta\lambda}$ [28, 29] where $\delta\lambda$ is the spectral resolution, λ the central wavelength, and n is the refractive index of the medium.

One major disadvantage of SD-OCT is the fact that there is large detection sensitivity roll-off along the imaging depth, due to the finite size of the camera pixel, the focused spot size of the beam after the scan lens, and the finite spectral resolution. The relationship has been previously described as [107]:

$$R(z) = \left(\frac{\sin(\zeta)}{\zeta}\right)^2 e^{\left[-\frac{w^2}{2\ln 2}\zeta^2\right]}, \tag{2.14}$$

where $\zeta = \frac{\pi}{2} \cdot \frac{z}{z_{RD}}$ the normalized imaging depth and $w = \frac{\Delta\lambda}{\delta\lambda}$ where $\Delta\lambda$ is the full-width-half-maximum spectral bandwidth accommodated by the spectrometer.

The above analysis shows that the optical design parameters determine the sensitivity roll-off at higher frequencies, however, another factor that affects the sensitivity roll-off even further is linear-wavenumber sampling. To finally acquire an A-line, a Fourier transform (FT) must be performed on the interference signal. In order to perform the FT, the interference signal must be linear with respect to wavenumber and not wavelength. Since the spectrometer shown in Figure 2.3 is linear with respect to

wavelength, the interference signal must be digitally resampled prior to the Fourier transform. This methodology has its own advantages and disadvantages compared to optically remapping the wavelengths linearly in wavenumber within the spectrometer design. Both methods shall be discussed further in the next section.

2.7.2 Linear K Sampling

As mentioned above, in order to recover the depth profile from the interference signal it is necessary to take the Fourier transform of the interference signal. The first available OCT imaging spectrometers employed an optical design where the wavelengths were mapped linearly in wavelength (e.g. Figure 2.3). This required remapping the wavelengths linearly in wavenumber with post-processing algorithms such as non-uniform Fourier transform, or resampling, prior to applying the Fourier transform [108-111].

Another method to obtain an interference signal linearly in wavenumber was through the combination of a grating and a prism [112], a concept that was discussed relatively early in literature. Only in 2007 [113] was this concept demonstrated in an OCT imaging spectrometer, enabling direct application of the Fourier transform to the acquired interference signal. This section will briefly discuss the numerical (software) or optical (hardware) methods available for mapping wavelengths linearly in wavenumber.

2.7.2.1 Digital Resampling

One of the first digital resampling methods implemented on SD-OCT acquired data was non-linear resampling or rescaling of the interference signal [114]. Currently, there are an abundance of software resampling methods including implementation of direct non-

uniform fast Fourier transform (FFT) and interpolation prior to FFT, aimed at reducing detection sensitivity roll-off and preventing deterioration of the axial PSF.

The simplest method is to perform a uniform FFT after resampling (linear interpolation) the interference signal. This method reduces the computational time at the cost of increased sensitivity fall-off due to errors in resampling at higher frequencies. Two approaches were developed in order to overcome the errors in linear interpolation, zero-padding and cubic spline interpolation. The zero padding method enabled correction of the increased background noise and reduction of side-lobes [108], while, cubic spline interpolation achieved similar results at the cost of computational time [110]. Regardless of the method, interpolation techniques generally degrade with increasing frequency leading to a greater sensitivity roll-off, motivating development of additional algorithms.

More sophisticated algorithms to remap wavelengths include employing a non-uniform discrete Fourier transform (NDFT) or a non-uniform FFT (NFFT). The NDFT algorithm was able to perform better image reconstruction compared to an FFT applied after cubic spline interpolation and resulted in a successfully low signal fall-off at the cost of significant computational time [111]. Contrastingly, the NFFT method is much better overall solution since it is faster than cubic spline interpolation (with FFT) and NDFT, has a better sensitivity roll-off performance, and reduced side-lobes. The algorithm has also been successfully demonstrated in other medical imaging modalities such as MRI, CT, and US. Although there are a few drawbacks, one of the main drawbacks would be aliasing artifacts that could potentially contaminate the image, however, by increasing the number of sampling points this could be alleviated as well [110].

Digital resampling and non-uniform FFT algorithms can be applied to any interference signal acquired from an SD-OCT system, however there will always be some signal sensitivity roll-off and axial PSF deterioration compared to optical (hardware) resampling methods due to the physical integration of non-uniform wavenumber bands at the image sensor in the spectrometer. These disadvantages champion implementation of optical resampling prior to data acquisition.

2.7.2.2 Optical Resampling

Optical resampling to map wavelengths linearly in wavenumber presents a more ideal solution to linear-wavenumber mapping due to the benefits of decreased detection sensitivity roll-off and limited PSF broadening along the imaging depth at the cost of an additional optical element in the spectrometer design.

Shortly before the first paper on OCT in 1991, a new linear-wavenumber spectrometer design was demonstrated with the combination of a grating and prism, coined "grism" [112]. It was demonstrated that by combining a prism after a grating, constant wavenumber dispersion could be achieved in a region from 450nm to 800 nm. Approximately a decade later a linear-wavenumber spectrometer was demonstrated for SD-OCT imaging [113, 115]. A customized prism was inserted into the beam path of the spatially diffracted wavelengths to provide constant angular dispersion with respect to wavenumber. An ~7 dB improvement in the detection sensitivity roll-off was observed at the folding range with a reduction in computational cost [113] for a 1300 nm SD-OCT system. Subsequently, in 2009, Gelikonov *et al*. demonstrated how a grating and prism could be paired together for either 800 nm or 1300 nm imaging spectrometers to perform

constant wavenumber dispersion imaging. By performing rigorous analysis it was determined that the apex angle of the prism and the angular separation between the grating and prism were the two controlling factors for linear wavenumber mapping as described by the equations below[115]:

$$sin\Psi(k) = n(k)\left(\alpha - arcsin\left\{\frac{\sin[\theta(k) - \beta]}{n(k)}\right\}\right). \quad 2.15$$

In this equation, α is the apex angle of the prism, β, is the angular separation between the grating and prism and $n(k)$ the refractive index function of the material and $\theta(k)$ the angular dispersion of wavenumbers after the grating. $\Psi(k)$, would be the final function that should have constant wavenumber dispersion into the imaging (scan) lens such that each wavenumber would be mapped to a spatial location *x* on the image sensor [115]:

$$x(k) = \frac{F}{D}tan[\Psi(k) - \Psi(k_0)] + x(k_0). \quad 2.16$$

Through this analysis, a linear wavelength spectrometer could now be modified to a linear wavenumber spectrometer resulting in improved system performance and enhanced image quality.

2.8 *Conclusions*

In this chapter, SD-OCT has been discussed in detail beginning with light-tissue interactions which result in backscattered light that is used in OCT, to the description of a generic SD-OCT system, discussion of the individual components in an SD-OCT system with the requirements for the imaging spectrometer. This chapter is a prelude to the following chapters to come, specifically chapter 3. Chapter 3 will discuss the ultrahigh

resolution, high speed endoscopic OCT platform that is based on an 800 nm SD-OCT system and will discuss the details of the specific system employed in this dissertation.

Chapter 3 Ultrahigh Resolution Endoscopic OCT System

3.1 *Introduction*

This chapter will focus on the implementation of an ultrahigh resolution endoscopic OCT system with a distal scanning catheter. The first half of the chapter will focus on a brief discussion of endoscopic OCT, types of catheters, and the challenges associated with designing a high resolution catheter for OCT. Following the general discussion, the design details and fabrication steps for the distal scanning catheter will be revealed.

The second half of the chapter will rationalize the choice of individual components employed in the SD-OCT engine, specifically the interferometer, the spectrometer and choice of light source. Two light sources will be described, a home built mode-locked Ti:Sapphire laser and a compact supercontinuum (SC) source from NKT Photonic (EXW-4). The system performance and noise characteristics for these sources will also be described. Following this discussion will be results demonstrating the capability to perform endoscopic imaging with both light sources. Finally, the chapter will conclude with comments on the future improvements for this ultrahigh resolution endoscopic OCT system.

3.2 *OCT endoscopy*

One of the most fundamental limitations for OCT is the shallow imaging depth (in comparison to other imaging modalities. The shallow imaging depth represented a major obstacle for OCT technology to be translated into the clinic for imaging internal organs *in vivo*. In order to

overcome this major limitation it was discovered that through the use of fiber-optics and miniature lenses[59], OCT could be packaged into an endoscopic platform for imaging. The ability to package OCT in this way gave rise to a new array of biomedical

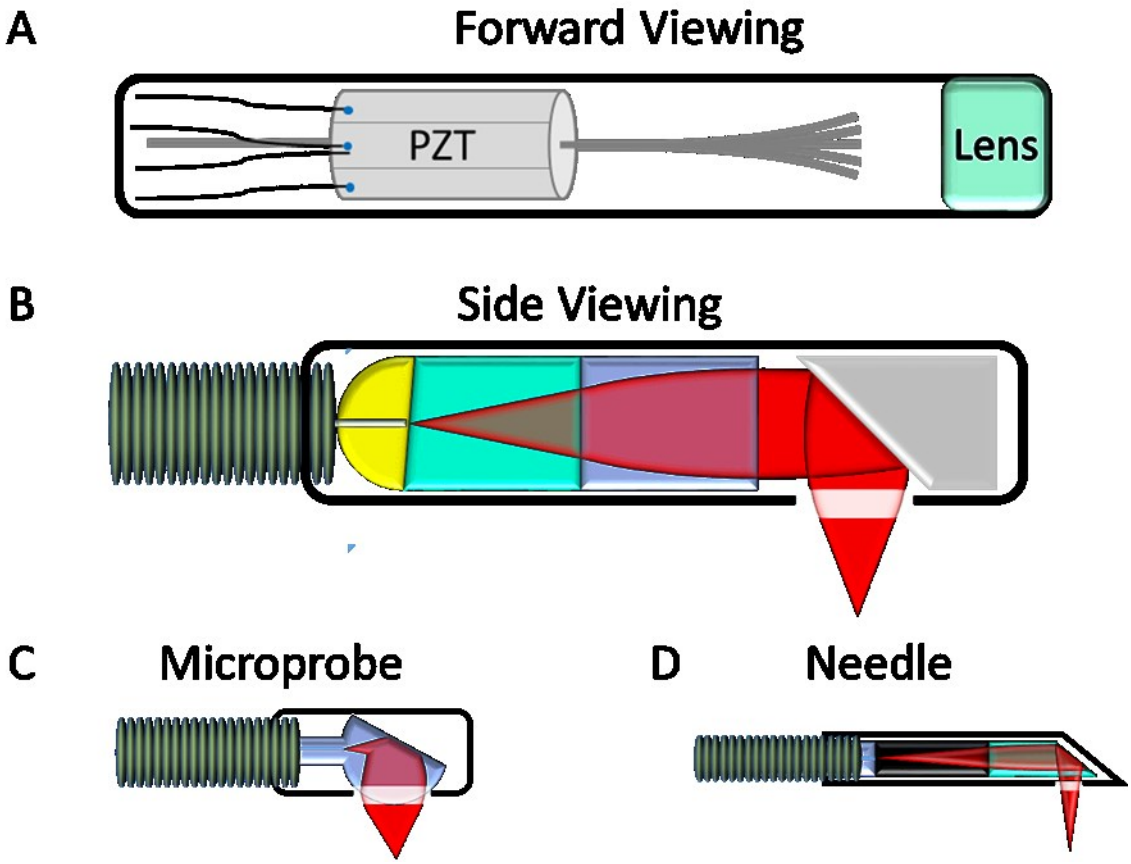

Figure 3.1: Types of OCT Catheters.

(A) An example of a forward-viewing resonant scanning catheter based on a piezoelectric (PZT) actuator[116]. (B) Example of proximal scanning side viewing catheter[59]. (C) and (D) are examples of miniature or ultrathin OCT catheters. (C) is an example of a microprobe based on a ball-lens [117] and (D)

is an example of a needle probe based on a GRIN lens design[118, 119].

applications and engineering challenges to solve. Since the first OCT catheter was demonstrated, numerous types of catheters have been developed for different biomedical applications.

Figure 3.1 shows an example of the three categories of catheters were developed, forward viewing, side viewing and imaging needles or microprobes, each of which have their own advantages and niche applications.

3.2.1 Forward Viewing Catheters

Forward viewing catheters are designed to image the tissue directly in front of the catheter, thus, these catheters are well suited to visualize walls of hollow organs such as the stomach [120] or bladder [121, 122]. Development of forward viewing catheters for endoscopic imaging has several challenges such as maintaining a small size and maintaining a maximal field of view with minimal image aberrations.

A few ways in which forward viewing catheters have been implemented are through resonant fiber scanning using a ceramic piezoelectric (lead zirconate titanate – PZT) actuator [116, 123], as shown in Figure 3.1 A, or alternatively scanning can also be performed by integrating a two axis microelectromechanical systems (MEMS) device [121, 124-127] into the catheter. One of the reasons that PZT based forward viewing catheters are more popular is due to the size and ability to be downscaled in comparison to MEMs devices which are usually the limiting factor in terms of size.

3.2.2 Side Viewing Catheters

Side viewing catheters are designed to deflect the laser beam 90° so that beam scanning can be performed radially, resulting in circumferential images of luminal organs. Figure 3.1 B shows an example of a proximal scanning, side-viewing catheter consisting of an optical fiber, compound lens and miniature reflector. These catheters have been used to image many luminal organs such as coronary arteries[50, 62, 128, 129], esophagus [65, 68, 69, 130] , colon [70, 71, 73, 130], and lungs[63, 64, 131].

Some of the major challenges associated with developing side viewing catheters, are designing a beam scanning mechanism that can operate at high rotational frame rates with minimal image distortion and maintaining a small size. There are two ways that circumferential scanning is performed, proximally and distally. Proximal rotation involves rotation of the entire OCT catheter through a torque applying mechanism such as a torque coil. Distal scanning rotation employs a miniature micromotor located at the distal end of the endoscope. Each of these approaches has their own advantages which will be discussed further, later in this chapter.

3.2.3 Needle Catheters and Microprobes

The last category of OCT catheters is needle catheters and microprobes because they are employed to image tumors in solid organs such as breast tumor [132, 133] or pancreas [134], or imaging alveoli or small airways in lungs [135-137]. Since needle probes are more invasive than forward viewing or side-viewing probes, the major design considerations are minimizing the overall size and ensuring a scanning mechanism that would allow for the formation of a meaningful image. Figure 3.1 C and D show a microprobe based on a fused fiber ball lens and a needle catheter based on a thermal fusion of a single mode fiber, multimode fiber and gradient index (GRIN) fiber. The main distinction shown between the needle catheter and microprobe is

that the needle catheter has an outer housing capable of piercing through tissue, demonstrated by the angular tip of the enclosure in Figure 3.1 D. Regardless of this difference; both optical designs can be employed as either needle catheters or as microprobes.

One of the advantages of thermally fusing single-mode, multi-mode and GRIN fiber together is that the overall size can be made as small as possible since the limiting factor is the diameter of the optical fiber. Alternatively, a ball lens approach is much simpler in construction and implementation, however can result in significant, spherical aberration, astigmatism and coma if the ball-lens is not perfectly spherical or polished properly [117].

3.2.4 Ultrahigh Resolution OCT Endoscopy

In this dissertation, we will focus on high resolution side-viewing probes for pulmonary imaging in small airways and imaging of the gastrointestinal tract in small animals, where the goal will be to visualize the wall structures of luminal organs.

Thus far, most endoscopic OCT systems have been implemented at 1300 nm, limiting the maximum achievable axial resolution to 4-20 μm [48, 138, 139]. One of the major efforts in the field of OCT is to increase the axial resolution of OCT systems in order to delineate fine microstructures such as airway smooth muscle, visualize intestinal crypts in small animals, and potentially detect early morphological changes in diseases for diagnosis or staging. In order to increase the axial resolution in OCT, we briefly revisit Equation 2.8 in chapter 2 which relates the axial resolution to the central wavelength and spectral bandwidth of the source, $\delta_z = \frac{2\ln(2)}{\pi} \cdot \frac{\lambda_0^2}{\Delta_\lambda}$. Through this equation, it becomes obvious that by taking advantage of the quadratic dependence on the central wavelengths the axial resolution can be much higher at shorter

central wavelengths, for a given spectral bandwidth. This phenomena has been well known in benchtop OCT systems where using broadband lasers at 800 nm resulted in axial resolutions of 1.5-2.5 μm in air [75, 97, 140].

Translating this known phenomena to an endoscopic setting has had limited success due to engineering challenges at 800 nm. Specifically the challenges in building a catheter at 800 nm are: 1) correcting chromatic aberrations in the distal end imaging optics and 2) implement a scanning mechanism capable of high speed volumetric imaging.

Over the past decade there have been a couple of attempts to implement ultrahigh resolution endoscopic OCT at 800 nm [76, 77, 99]. These designs presented the first foray into ultrahigh resolution endoscopic OCT imaging at 800 nm. The first catheter was a common path OCT probe which incorporated an interferometer in the distal end optics achieving an axial resolution of ~3.3 μm (in air)[76]. The main drawbacks of this design were the low signal-to-noise ratio due to inadequate collection efficiency from the reference reflection and insufficient dispersion mismatch. Although the common path design accounts for much of the dispersion occurring from path length mismatch, the fused silica window through which the beam exited was not compensated. The combination of dispersion mismatch and lack of chromatic aberration compensation in the lens design ultimately lead to a suboptimal axial resolution. The second design improved upon the first by eliminating the common path design (using a dual arm configuration) and employing doublets to compensate for chromatic aberration [77]. Unfortunately, poor dispersion mismatch resulted in only ~10-15 nm improvement in the axial resolution (3.2 μm in air). Finally, the major drawback of both designs was the lack of

circumferential scanning mechanisms limiting the catheter to 2D images through a push-pull mechanism.

More recently, a proximal scanning diffractive catheter for volumetric imaging was demonstrated by our lab [78]. The key design elements incorporated a diffractive lens for compensation of chromatic aberrations, resulting in a 3.0 μm (in air) axial resolution and engineering a home-built fiber optic rotary joint for circumferential scanning. Both of these innovations enabled volumetric ultrahigh resolution endoscopic imaging to be performed. Through further innovation and employment of a broadband supercontinuum an even higher axial resolution of 2.7 μm (in air) was achieved [100].

Although a high axial resolution was achieved endoscopically, there are still several drawbacks to this approach. The employed home-built rotary joint is based upon a capillary tube design. In this design two bare fibers are inserted into the two opposite ends of the capillary tube. One fiber will remain stationary while the other will rotate; and the rotating fiber can be connected to a catheter through a mechanical assembly and bulk mating sleeve. This approach suffers from several disadvantages such as 1) limited lifetime, 2) easily misalignment at high speeds due to small core size (4.0 μm) of single-mode fiber at 800 nm resulting in 3) intensity and spectral modulations. These challenges limited the overall imaging frame-rate to less than 10 frames-per-second making it too slow for practical imaging in live specimens and eventual translation into clinical imaging. In order to solve these challenges we have chosen to implement a distal scanning OCT catheter design, which will be discussed further in the following section.

3.3 *Catheter design*

This section will be dedicated to the mechanical and optical design considerations employed in order to engineer a high speed, ultrahigh resolution, distal scanning, side-viewing catheter for volumetric imaging.

3.3.1 Distal Scanning Mechanism

In order to perform circumferential scanning with a distal scanning catheter, a miniature micromotor needs to be incorporated into the catheter design. The first distal scanning endoscope was demonstrated in 2004 with a 1.9 mm MEMS micromotor [141]. The MEMS micromotor has great advantages such as high speed (up to 1000 frames-per-second) and low drive voltage (< 5 volts) however the one major drawback is that it was difficult to further reduce the size. Thus an alternative to a MEMS micromotor was demonstrated soon after the aforementioned probe using a 3 phase DC brushless micromotor from Micro Precision Systems AG (now Faulhaber) [142]. DC micromotors are still a popular option due to the availability, small size (> 1 mm), and ability to achieve high rotational velocities up to 400 frames-per-second [130, 143].

Another type of miniature micromotor that is becoming popular is a 2 phase miniature AC micromotor by Kinetron [50, 129, 144]. This motor has a small footprint (1 mm diameter x 2 mm length) and is capable of reaching rotational speeds up to 3200 frames-per-second. One of the major drawbacks is that this motor is sensitive to magnetic fields. The alternating current drive waveforms to the motor are capable of magnetizing

the mechanical enclosure[2] and once the enclosure is magnetized, the AC motor can no longer rotate within the enclosure. Hence, using this motor requires additional concern for the enclosure materials when considering the mechanical design of the catheter.

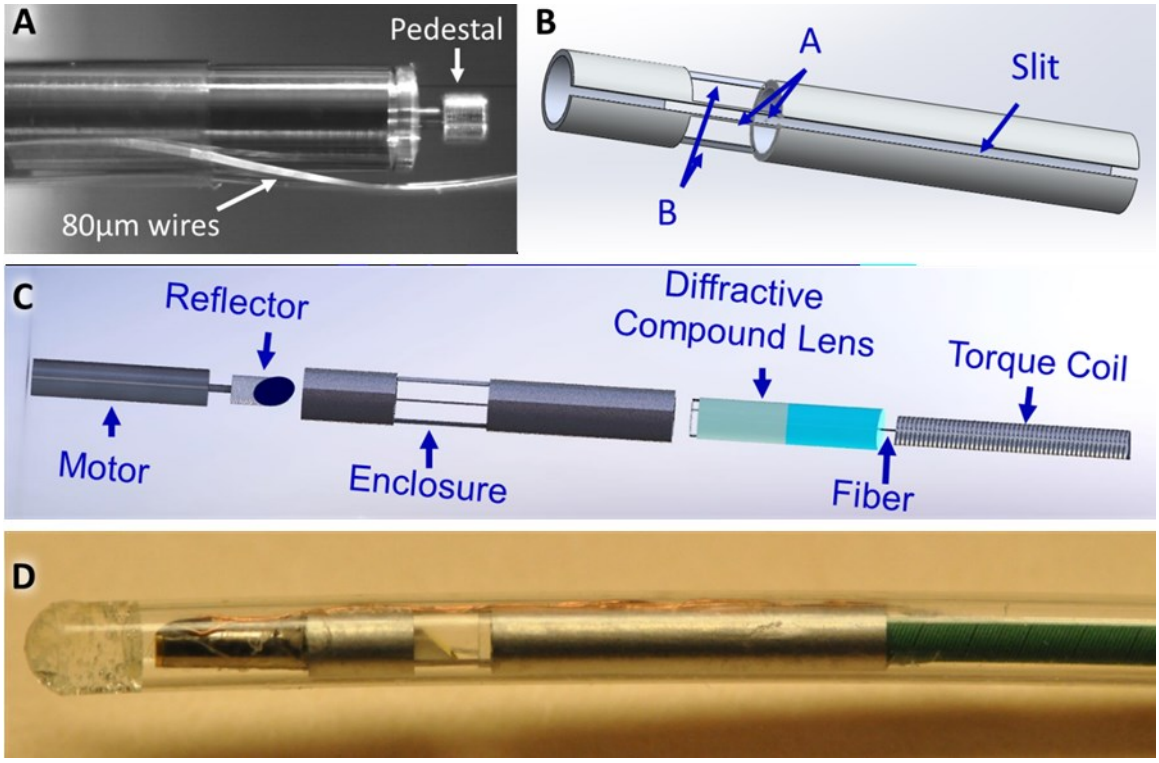

Figure 3.2 Miniature micromotor, distal enclosure and mechanical design schematic.

(A) Photograph of customized 900µm diameter DC micromotor. (B) 3D drawing of laser cut enclosure. A: 2 struts supporting the slit running along the length of the enclosure, B: 2 remaining struts for mechanical

[2] Although stainless steel is non ferromagnetic, under certain conditions such as after machining, the material can become magnetized. This small amount of magnetization can easily prevent the AC motor from rotating.

integrity placed ±108° from support struts in A. (C) Blow-out view of schematic of high speed, ultrahigh resolution distal scanning catheter. (D) Photograph of assembled catheter inside protective plastic sheath (outer diameter 1.78 mm).

In this dissertation the distal end scanning catheter employs a customized 0.9 mm diameter 3 phase DC micromotor by Namiki as shown in Figure 3.2 A. The motor is capable of rotating at 200 rotations-per-second with no load. The micromotor is 4 mm long with a 200 μm diameter shaft and was customized to have forward feeding ultrathin signal drive wires and a small pedestal mounted on the reflector shaft.

The 3 ultrathin wires are each 80 μm in diameter with 1 wire per phase winding of the motor. It was necessary to customize the wires to ensure they are ultrathin to ensure that the field of view blockage due to the wires impeding the beam path is as minimal as possible. The forward-feeding configuration eliminated the need to bend the wires backwards along the axis of the optical fiber, preventing any damage to the wires during backward bending. Finally, the small pedestal as pictured in Figure 3.3 A is 500 μm in diameter. The pedestal helps to increase the contact area to adhere a rod reflector or prism to the shaft. The increased contact area ensures that the reflector base is flush against the pedestal minimizing risk of unwanted angular displacement.

3.3.2 Mechanical Design

The mechanical design of a distal scanning endoscope needs to take into consideration factors such as mechanical strength, overall size of distal end of catheter and ways to minimize the field of view blockage.

In a distal scanning endoscope the miniature micromotor sits opposite the distal optics, requiring a way to align and center the reflector with the optics. While there have been numerous distal scanning catheters, alignment and centering has mostly been performed by using multiple concentric pieces [142] or a single piece of hypodermic tubing [130, 143, 145, 146] with a window to allow the optical beam to exit. Hypodermic tubing provides the rigidity and mechanical support needed to avoiding bending and buckling near the optical window. In the case of an AC micromotor, as described in the previous section, heat shrink plastic tubing [50, 129, 144], a glass capillary tube or a combination of both could be used to avoid susceptibility to magnetizing the hypodermic tubing.

Using hypodermic tubing for the distal enclosure has several benefits such as the fact that it is inexpensive, comes in a variety of sizes and wall thicknesses, can customized at a relatively low cost. In terms of machinability, hypodermic tubing is that it can be machined by hand or by laser cutting, allowing for simple or sophisticated distal enclosures to accommodate a range of designs.

In this dissertation, we chose to manufacture the distal enclosure from a single piece of 18 gauge extra-thin-wall stainless steel hypodermic tubing. The hypodermic tubing had an outer diameter (OD) of 1.27 mm and an inner diameter (ID) of 1.1 mm. The overall mechanical design is shown in Figure 3.2 B. In order to maintain mechanical

and structural integrity while minimizing the field of view blockage, the enclosure was designed with three windows, 1.5 mm long and ~1.22 mm wide, separated by struts ~35 μm wide (labeled *A* and *B* in Figure 3.2 B). The distal end of the enclosure was 1.5 mm in length providing enough contact area for the micromotor to be inserted and fixed (to the enclosure), without impeding the forward feeding wires. The proximal end was 6 mm long to ensure that the optical assembly and the junction between the optical fiber and lens could be inserted into the enclosure for full protection.

A key feature of this design is the small slit, ~160 μm wide, running down the full length of the enclosure as seen in Figure 3.2 B. Due to the small slit, there are 4 total struts bordering the three windows; the first and last struts run along-side the slit and are labeled as *A* and the remaining two struts are labeled as *B*. This slit is the ideal width to fit the ultrathin motor drive wires such that the wires are flushed with respect to the enclosure. Ensuring the wires are flushed with the outer diameter of the enclosure has two benefits, 1) there is no increase in the outer diameter of the distal end of the probe and 2) the wires are protected from breaking, at the solder junction on the motor, during insertion into the protective plastic sheath. Finally, the enclosure design was able to maintain a minimal field of view blockage to 7.5%, this includes blockage from 4 struts of the enclosure as well as the slit where drive wires would be inserted.

Figure 3.2 C shows the schematic of the distal end of the catheter, with the motor, reflector, enclosure, compound lens, fiber and protective torque coil, and Figure 3.2 D is a photograph of the fully assembled distal scanning catheter. With the transparent protective plastic sheath, the entire catheter has an outer diameter of 1.78 mm.

3.3.3 Distal End Optics

In general, the optical design of an catheter includes a fiber optic component and imaging optics at the distal end with some type of reflector to deflect the beam 90° to exit orthogonal to the optical axis of the catheter. The optical design of the catheter governs the achievable lateral resolution however, can also affect the axial resolution as will be discussed in the next section.

Distal end optics designs are governed by size and resolution requirements. Generally speaking, side-viewing OCT catheters that are employed in conjunction with a standard clinical endoscope require the catheter to fit into the working channel of the clinical endoscope which range from ~1.2 mm [147] to 3.7 mm [148] for bronchoscopes to colonoscopes. The small diameter of the working channel limits the overall catheter sizes and in turn the allowable size of the distal end optics.

Despite size constraints, numerous distal end optics designs have been developed for OCT catheters and can be separated into two categories, 1) single lens and 2) compound lens designs. The designs that are compound lenses will include multiple components as opposed to a single lens design where a focusing lens is employed directly after the optical fiber.

Single lens designs such as thermally fused spherical lenses [117] or gradient index (GRIN) fibers [118, 149] and optically cemented GRIN lenses [59, 141, 150] are among the most popular options due to simplicity and ease of implementations. One of the major drawbacks with a single lens design is that the lateral resolution must be sacrificed in order to achieve a longer focal length. Additionally, ball lenses can suffer

from spherical aberrations and astigmatism if not perfectly spherical and GRIN lenses can suffer from severe chromatic aberrations for broad spectral bandwidths.

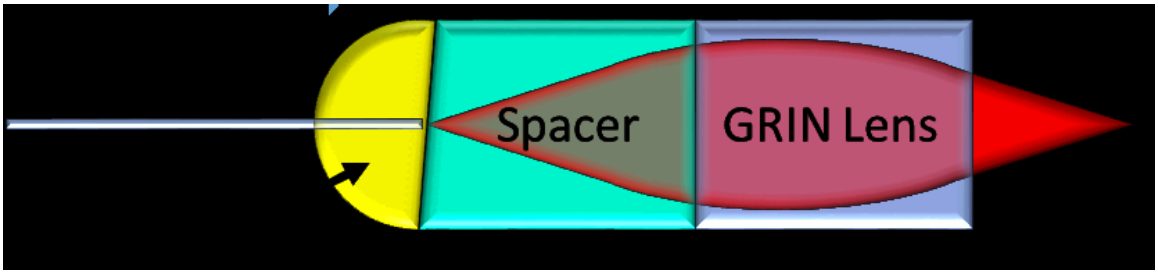

Figure 3.3 Schematic of OCT catheter optics.

Schematic of general distal end optics for an OCT catheter. W.D.: working distance.

Compound lens designs with multiple optical elements can be employed to solve some or all of these issues. Compound lens designs incorporate more than one optical element in the lens design as shown in Figure 3.3. The basic concept involves using a spacer material to expand the optical beam prior to a focusing element such as a GRIN lens in order to achieve a higher numerical aperture beam resulting in a higher lateral resolution. This design has been employed in numerous OCT catheters and has become particularly useful for long working distance probes such as balloon catheters for esophageal imaging [138, 139]. This design has also been implemented using a step index multimode fiber for a spacer and GRIN fiber as a focusing element for ultrathin needle probes [119, 135, 149] with an outer diameter from ~310 μm to 410 μm. Other compound lens designs employed a GRIN lens as a collimator and an off-the-shelf achromatic lens as the focusing element so that the focal position inside the tissue could be adjusted by moving the doublet towards the reflector [142]. Finally, another design

employed a pair of doublets to compensate for chromatic aberration at the 800 nm wavelength range [77].

In this dissertation, the goal was to have an optical design that was able to compensate for chromatic aberration in the lens design enabling us to achieve ultrahigh axial resolution. Our group has demonstrated another way to achieve ultrahigh axial resolution was through the use of diffractive optics to compensate for chromatic aberration [78, 100] achieving an overall axial resolution of 2.7 μm with a broadband supercontinuum. The design employed a compound lens design with a standard glass rod as a beam expander and a GRIN lens as a focusing element with an additional miniature diffractive microlens to compensate for chromatic aberration. The aforementioned design will also be implemented in this dissertation and will be discussed briefly below.

A Corning HI 780 single-mode fiber was used to deliver light to the catheter optics which consisted of a 1 mm diameter glass rod and a 1 mm SLW (wide angle) gradient index (GRIN) lens from GoFoton. The target beam focus position was ~1.9 mm away from the GRIN lens surface, yielding a design with a 3.1 mm long glass rod and 0.14 pitch GRIN lens.

3.3.4 Chromatic Aberrations

Use of conventional refractive optics, such as the glass rod and GRIN lens described above, rely on the refractive index of the lens material and the curvature of the lens surface. However since refractive index is wavelength dependent, not all wavelengths will focus to the same point on the optical axis, leading to chromatic aberration. In chromatic aberration, short wavelengths will focus closer while long wavelengths will focus farther away on the optical axis.

In general, chromatic aberration can lead to blur, or fringing of colors in photographs. OCT needs to employ broadband light source to achieve high axial resolutions, making chromatic aberration an issue in the spectrometer design (discussed in chapter 2), reference arm, and sample arm optics. In the sample arm, chromatic aberration can change the spectral throughput, leading to a narrower bandwidth and reduction of the axial resolution along the imaging depth. In order to reduce chromatic aberration to preserve the axial resolution there are a few options, 1) use lens materials that have little variation in refractive index with respect to wavelength, or 2) use achromatic lenses, or 3) employ diffractive optics.

Using lens materials that are less sensitive to wavelengths, such as calcium fluorite (CaF_2), is difficult due to the limited options in available focal lengths and sizes. Alternatively, the catheter optics could employ achromatic lenses[77], however this would make the optical design more expensive, complex and further reduction of size would be difficult. The third option is to employ diffractive optics.

Diffractive optics manipulates wavefronts through interference and diffraction for focusing or spectral dispersion. Alternatively, weakly focusing diffractive optics can be used in conjunction with a normal refractive element to correct for chromatic aberration [151]. In this dissertation, we chose to employ a customized, miniature diffractive lens to compensate for chromatic aberration incurred from the compound lens described in the previous section[78, 100].

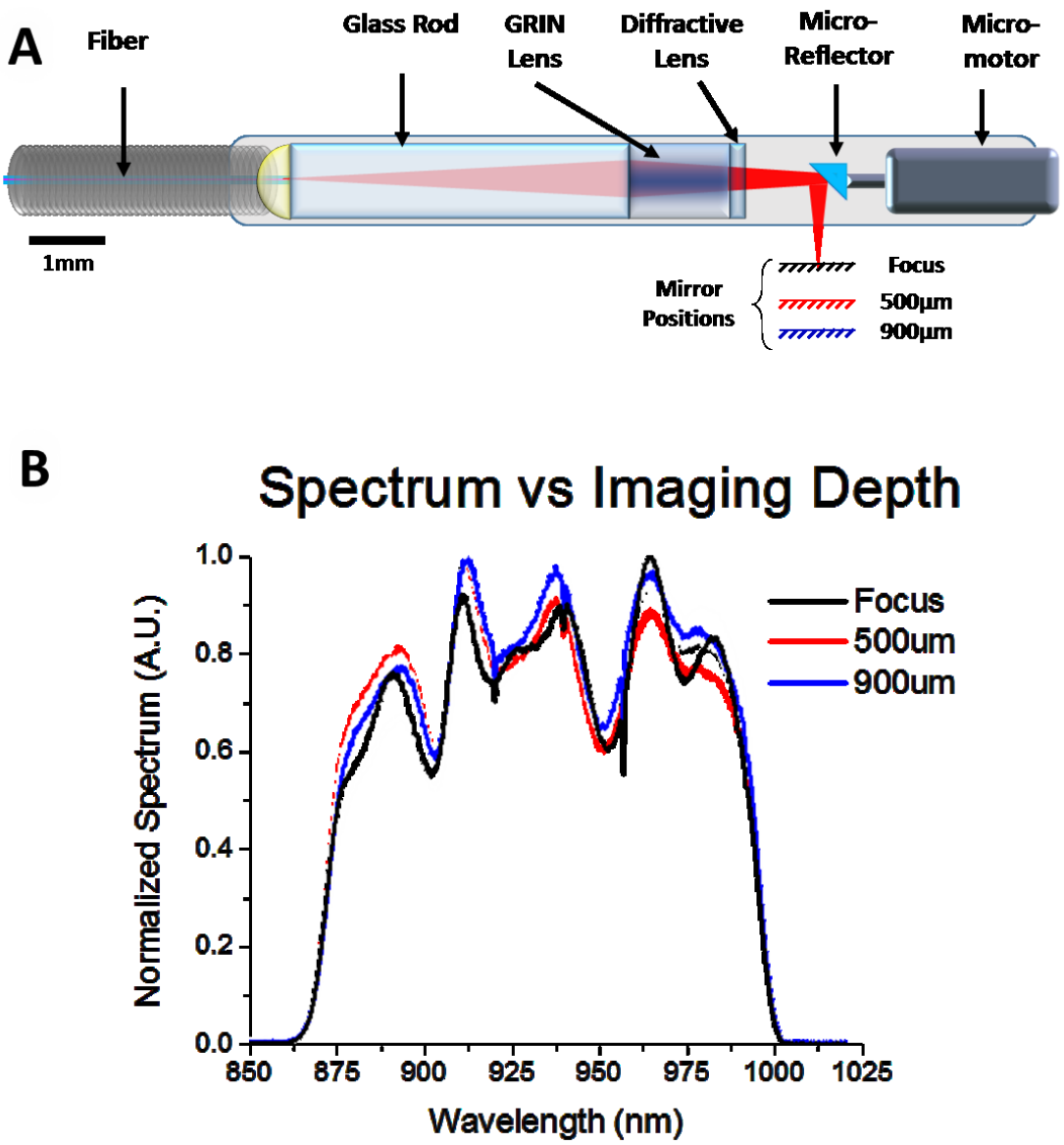

Figure 3.4 Performance of diffractive element.

Verification of achromaticity of imaging optics. (A) Schematic of the distal end optics of the ultrahigh resolution endoscope showing three mirror locations (i.e. focal plane in black(~260 µm from the protective plastic sheath), 500 µm away from focal plane in red, and 900 µm away from the focal plane in blue). Each mirror location corresponds to the

back-reflected spectra shown in (B).

The customized diffractive element was designed for a wavelength range from 700 to 1000 nm and had a diameter of size of 900 μm.

To verify the performance of the diffractive compound lens, we measured the back-reflected spectra from the finished catheter with respect to the imaging depth by moving a mirror to different positions along the imaging depth (e.g. the focal plane, and 500 μm and 900 μm away from the focal plane) as shown in Figure 3.3 A. For this measurement we used a broadband superluminescent diode (SLD) (Superlum Broadlight T870). The SLD had a central wavelength of 880 nm and a 10 dB spectral bandwidth of 182 nm. Figure 3.4 B shows the nearly unchanged back-reflected curves from the OCT catheter at the focal plane, and 500 μm and 900 μm away from the focal plane, demonstrating superb achromatic performance.

3.4 *Interferometer*

Interferometer configurations for an SD-OCT system were discussed previously in chapter 2. It was stated that for an 800 nm SD-OCT system a Michelson interferometer is ideal. In order to make it a portable for translational and clinical endoscopic imaging, a fiber-optic Michelson interferometer can be employed.

In this dissertation, the fiber optic coupler used for the SD-OCT system is an ultra-wide bandwidth 50/50 optical coupler from Gould Fiber Optics (GFO). The coupler has been manufactured from Nufern 630 HP fiber and was tested at a design wavelength of 856 nm.

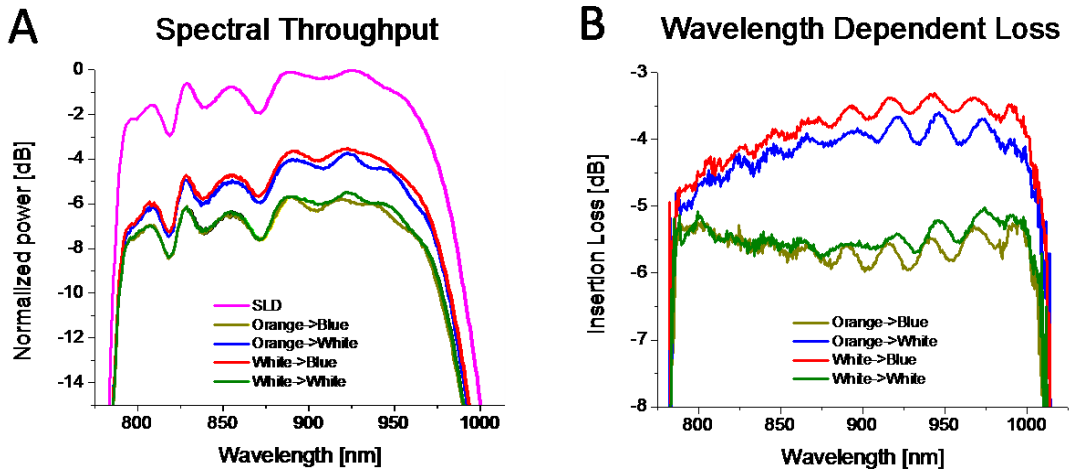

Figure 3.5 Performance characteristics of broadband coupler.

(A) Spectral throughput measured by checking the output from each interferometer arm for each input arm, using broadband SLD. (B) Wavelength dependent loss calculated from the ratio of the output to the input spectra from SLD.

In order to determine whether or not the performance of this optical coupler was sufficient, the spectral throughput and wavelength dependent loss were measured using a broadband SLD, with a central wavelength of 882 nm and a spectral bandwidth of 182 nm. Figure 3.5 A shows the original spectrum in magenta, labeled SLD, and four output spectra generated from fiber coupling the SLD output into each input arm sequentially. As can be seen, the spectral shape is not significantly altered, and this is confirmed by the wavelength dependent loss shown in Figure 3.5 B, where the loss is relatively uniform across the bandwidth from ~ 750 nm to 1000 nm.

Input → Output	Insertion Loss	Interferometer Configuration
Orange – Blue	- 4.85 dB	Light Source – Sample Arm
Orange – White	- 3.27 dB	Light Source – Reference Arm
White – White	- 4.16 dB	Detector – Reference Arm
White – Blue	- 2.55 dB	Detector – Sample Arm

Table 3-1 Test data for Gould Fiber Optics ultra-wide band coupler.

Furthermore, the coupler test data is shown in Table 3-1 with the interferometer configuration is shown in the third column. It is important to note that while the insertion loss to the sample arm is higher than for the reference arm, the return loss to the detector is the lowest. This configuration ensures that there is no unnecessary loss in the sample arm and maximal backscattered photons are coupled into the fiber to be collected, resulting in higher detection sensitivity.

3.5 *Reference arm*

The reference arm is an important part of the OCT system and there are a three main concerns when designing a reference arm. Firstly, the reference arm optics must be able to accommodate the broad spectral bandwidth from the source due to the fact that any deterioration of the spectral throughput in the reference arm can lead to degradation of the axial resolution. Secondly, the path length in the reference arm must match the path length in the sample arm in order to be able to achieve interference with minimal material dispersion Thirdly, the power level in the reference arm needs to be set at an appropriate

level in order to ensure that the system is operating within the shot noise limited region, while allowing for maximal gain without saturating the CCD in the spectrometer.

In order to address these concerns, the reference arm optics consist of an apoachromatic collimating lens and dispersion compensating prism pair. The apoachromatic collimating lens ensures that focal lengths of the wavelengths are as close as possible so that there is no spectral distortion when the return light is coupled back into the lens and fiber. The dispersion compensation prism pair was made from SF-11 to compensate the higher material dispersion at shorter central wavelengths, and was adjusted as needed to match the path length due to the OCT imaging catheter. Finally, the OCT system noise level was measured with the light sources that are discussed in section 3.7 and the shot noise region for each light source was determined (shown in Figure 3.10). In order to reduce light intensity in the reference arm to ensure it is within the shot noise range, a variable neutral density filter wheel was used. An example of the reference arm configuration is shown in Figure 3.6 A.

3.6 *Spectrometer*

The specific requirements for an imaging spectrometer in a SD-OCT system were described earlier in chapter 2. In this dissertation, the imaging spectrometer employed in the SD-OCT engine is a linear-wavenumber spectrometer.

The spectrometer design is shown in Figure 3.6 A with a general schematic of the SD-OCT system. The light from the interferometer is first collimated through an achromatic doublet. A volumetric transmission grating with 1200 line-pairs-per-mm and a design wavelength of 830 nm is employed to spectrally disperse the wavelengths in the

interference signal. A BK-7 prism was customized with a specific apex angle (~57°) to ensure that when it is placed in the optical beam path, the wavelengths are able to map linearly with respect to wavenumber. After the wavelengths have been remapped, a multi-element F-theta scan lens with a focal length of ~50.8 mm is employed to focus angularly dispersed wavelengths to points on a focal plane. Finally, a linear CCD array with 2048 pixels and a 12 bit resolution is placed at the focal plane of the multi-element scan lens, to collect the interference signal. The linear CCD array is able to acquire data at a maximum A-scan rate of 70,000 A-lines-per-second with an exposure time of 12 µs and a line period of 14.28 µs.

The overall spectrometer design enabled accommodation of a spectral bandwidth of 240 nm with a spectral resolution of 0.121 nm-per-pixel, enabling a calibrated imaging depth of 1.23 mm and a sensitivity roll-off of -16 dB over the full imaging depth, as shown in Figure 3.6 B.

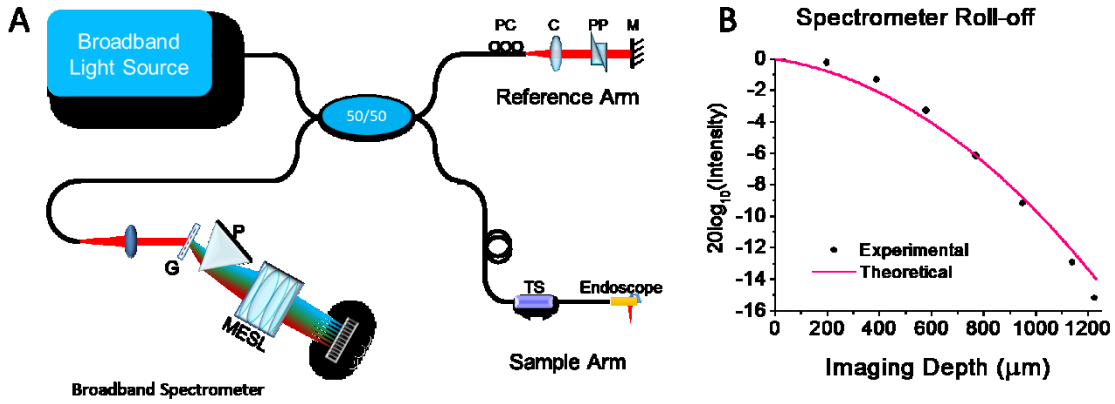

Figure 3.6 SD-OCT system schematic and spectrometer signal-off.

(A) Ultrahigh-resolution endoscopic SD-OCT system. Linear-k-

spectrometer: G: volumetric transmission grating, P: prism, MESL: multi-element scan lens. Reference arm: PC: polarization controller, C: collimator, PP: prism pair, M: mirror. Sample arm: TS: linear translation stage. (B) Detection sensitivity roll-off over the calibrated imaging depth of 1.23 mm.

The sensitivity roll-off of -16 dB depends upon the spectrometer design and was previously described in chapter 2. We revisit the sensitivity roll-off here, with the intent to describe practically which factors of the spectrometer design contribute to the roll-off. The relationship has been previously described as [107]:

$$R(z) = \left(\frac{\sin(\zeta)}{\zeta}\right)^2 e^{\left[-\frac{w^2}{2\ln 2}\zeta^2\right]}. \quad 3.1$$

In equation 3.1, ζ is the normalized imaging depth, given as $\zeta = \frac{\pi}{2} \cdot \frac{z}{z_{RD}}$ and w is the fraction of the spectrum which illuminates each detector pixel, defined by $w = \frac{\Delta\lambda}{\delta\lambda}$, where $\Delta\lambda$ is the full-width-half-maximum spectral bandwidth accommodated by the spectrometer and $\delta\lambda$ is the spectral resolution of the spectrometer. Equation 3.1 consists of two parts, a Sinc function multiplied by a Gaussian function. The Sinc function is the contribution due to the rectangular CCD pixel array and is the result of the Fourier transform of the Rectangular function[152]. The Gaussian portion of the signal describes the overall spectral shape incident on the CCD array as well as the finite sampling of the interference signal, encoded in *w*. Finally it is the finite sampling of the interference signal makes it difficult to resolve high fringe frequencies leading to sensitivity roll-off.

3.7 *Light source*

This chapter is focused on achieving ultrahigh resolution. The ideal properties of a light source for OCT, as discussed in chapter 2, are providing a broad spectral bandwidth, high output power, low laser noise, and operating in the wavelength range of interest (in this chapter it is ~800 nm).

This section will focus on the two light sources that have been used in this dissertation for ultrahigh resolution endoscopic OCT. The first will be a benchtop home-built Ti:Sapphire laser, while the other a portable supercontinuum source enabling translation into the clinic.

3.7.1 Ti:Sapphire Laser

Solid state lasers provided an ideal solution to a low temporally coherent light source with high optical power and low noise. Thus we chose to use a Kerr-lens mode-locked Ti:Sapphire laser with a central wavelength of 830 nm and a bandwidth of ~ 150 nm. The broadband Ti:Sapphire provided us enough output power (greater than 80 mW to the interferometer) as well as linear output polarization. The source spectrum was also able to be adjusted to provide a near Gaussian spectrum at the spectrometer which is shown in Figure 3.7.

Figure 3.7 Ti:Sapphire spectra and axial resolution measurement.

(A) Spectrum of Ti:Sapphire directly and (B) at spectrometer CCD. SD-OCT spectrometer performance graphs. (C) Axial resolution measured with respect to the imaging depth. Graph shows that there is minimal broadening of the axial PSF along the imaging depth.

This source in combination with the spectrometer design enabled us to achieve an axial resolution of 2.8 μm with minimal variation along the imaging depth. Furthermore, the performance of spectrometer sensitivity roll-off is shown in Figure 3.6 B. Although, the sensitivity roll-off is almost purely a factor of the spectrometer design, the roll-off has been shown here in order to demonstrate that the spectrometer alignment allowed the spectrometer to perform close to the theoretical predictions.

While this source represents a myriad of good performance characteristics, it is big, bulky, difficult to transport and lacks a turnkey operation. For this reason alternate light sources were sought out. Two such compatible light sources enabling turnkey operation with a broad bandwidth are superluminescent diodes (SLDs) and supercontinuum light sources (SC). Unfortunately SLDs do not provide enough output power for high speed scanning (refer to Equation 2.12). Thus, in the next section the merits of employing a supercontinuum are laid out.

3.7.2 Supercontinuum

In this dissertation the SC source employed was a NKT Photonics SuperK EXW-4 low noise light source. In order to achieve ultrahigh axial resolution endoscopically, the severe limitations in spectral shape and high laser noise had to first be addressed.

3.7.2.1 Spectral Shaping

From the chapter 2 it is known that the autocorrelation of spectral shape of the light source is determines the shape of the axial point spread function (PSF). Thus, in order to achieve an ideal axial point-spread function and suppress high side-lobes, it would be desirable to have a more Gaussian spectral shape.

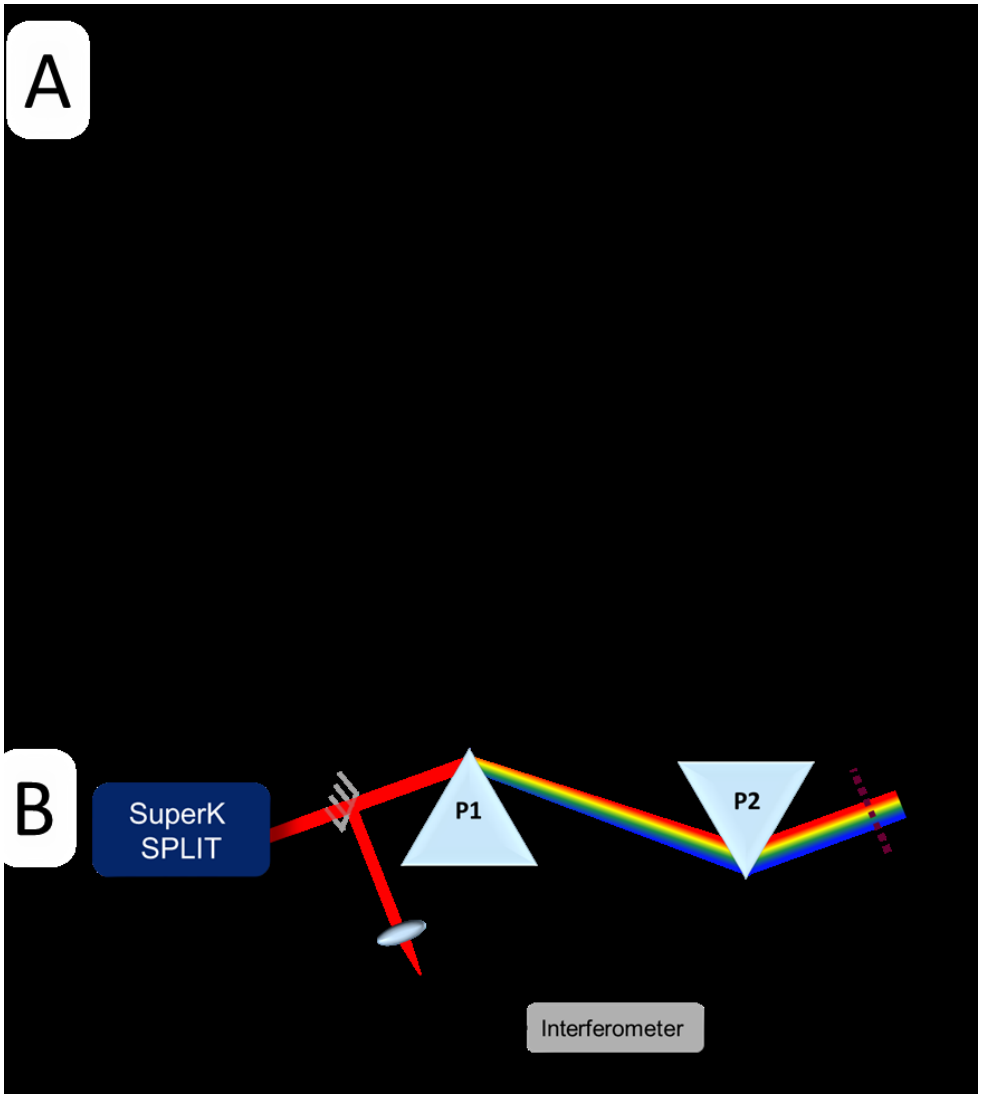

Figure 3.8 Original SC spectra and spectral shaping setup.

(A) Measured supercontinuum spectrum and (B) schematic of spectral shaping setup required to shape the supercontinuum spectrum. PM: pickup mirror, P1: prism 1, P2: prism 2, F: spatial filter, M: mirror.

The overall SC spectrum is extremely broad (400-2400 nm) and the source comes with a fiber coupled, collimated output with a beam diameter ~ 1 mm at 530 nm, ~2 mm at 1100 nm and ~ 3 mm at 2000 nm [153]. Due to the extremely broad spectral bandwidth of the laser a filter box**,** SuperK SPLIT [154], was employed to separate the spectral output into short (<1000 nm) and long (>1000 nm) wavelengths. The filter box did not perform any spectral shaping functions and strictly provided a collimated output from the filter box. The collimated output was fiber coupled through a superachromatic lens and measured with an OSA (model: ANDO AQ-6315E), the measured spectrum is shown in Figure 3.8 A. The collimated output of the SuperK SPLIT was sent into a home-built spectral shaping system in Figure 3.8 B. The output is sent through a set of dispersion compensation prisms from Thorlabs (AFS-FS).

The dispersion compensation prisms are generally used for compensating the dispersion, through adjustment of prism material, in laser cavities to ensure a narrow pulse width. When the laser beam traverses a prism, it is also spectrally dispersed and then made into a parallel beam. This phenomenon can be exploited to manipulate the spectral shape of the light source prior to use for imaging.

As shown in Figure 3.8 B, the collimated output beam is incident on prism 1 and emerges spectrally dispersed. The deviation angle of light through a prism is given by Equation 3.2:

$$\delta = \theta_0 + \sin^{-1}\left(n \sin\left[\alpha - \sin^{-1}\left(\frac{1}{n}\sin\theta_0\right)\right]\right) - \alpha. \quad 3.2$$

In Equation 3.2, δ is the deviation angle, θ_0 is the angle of incidence, n is the refractive index of the prism, and α is the apex angle of the prism. The distance between prisms 1 and 2 depend upon the amount of spectral dispersion desired, a larger separation will yield a finer spectral resolution when the dispersed components emerge from prism 2 as parallel beam[3].

At this point spectral shaping or filtering can be performed, and is schematically represented by the dashed purple line in Figure 3.8 B, labeled as F. A piece of optical fiber was placed before the mirror as a spatial filter. The optical fiber allowed a portion of the light to be attenuated, at the location of a spectral peak at 700 nm, through the clear optical fiber without sacrificing intensity of all wavelengths. The parallel beam was back-reflected through a slightly deviated path using a mirror after prism 2. The back-reflected path was then picked off by a pickup mirror and directed to an achromatic lens for fiber coupling into a Nufern 630 HP fiber and then coupled into the Michelson interferometer. The final spectral shape acquired at the CCD (after back-reflection from the reference arm) had an overall spectral bandwidth 165 nm centered about ~825 nm, as shown in Figure 3.9 A with the achievable axial resolution shown in Figure 3.9 B.

[3] The maximum amount of spectral resolution achievable is ultimately be governed by the physical size of the prism.

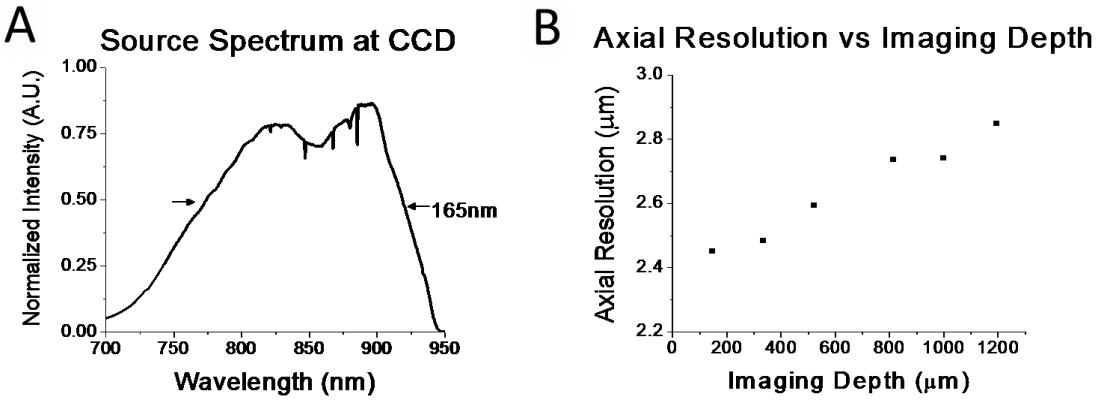

Figure 3.9 Shaped SC spectrum and axial resolution measurement.

(A) Spectrum of supercontinuum from SPLIT and (B) at spectrometer CCD. SD-OCT spectrometer performance graphs. (C) Axial resolution measured with respect to the imaging depth. Graph shows broadening of the axial PSF along the imaging depth, due to broad spectrum, suboptimal spectral shape and slight misalignment of imaging spectrometer.

3.8 *Source Comparison*

This section endeavors to compare the noise features of the Ti:Sapphire laser and the NKT Photonics supercontinuum source that affect image quality. Specifically, these features are the noise floor, laser excess noise, and shot noise measurements. Furthermore, it will be shown that under the correct circumstances the aforementioned supercontinuum can be employed for ultrahigh resolution SD-OCT imaging and provide good image quality.

3.8.1 Power Spectrum and Noise Floor[100]

In order to measure the power spectrum of the two light sources, a small portion of the laser output (~5.14 mW) was sent to a high speed silicon photodetector (Thorlabs DET10A) which was then coupled to an electronic spectrum analyzer (ESA) (Advantest

R3265A). An electronic spectrum analyzer can measure the power spectrum of the input signal through the full frequency range of the instrument. Figure 3.10 A and B are the results of the ESA measurements from 0-500 MHz.

Figure 3.10 A shows the power spectrum measurement of both the Ti:Sapphire and supercontinuum sources. Peaks are found at the repetition rate of the laser and corresponding harmonics. The repetition rates of the Ti:Sapphire laser and supercontinuum are ~80 MHz and ~315 MHz, respectively. One of the considerations when choosing a pulsed laser is to ensure that the laser repetition rate is sufficiently high compared to the A-scan rate in order to ensure that any pulse-to-pulse variation or noise can be averaged out to minimize variations between sequential A-lines. In this dissertation, the A-scan rate of the system is ~70 kHz, thus the repetition rates of both lasers are sufficiently high that several pulses will be averaged within the exposure time of the CCD in the spectrometer.

When the same power spectrum is plotted without the peaks as in Figure 3.10 B, we can focus on the noise floor. It can be seen that the supercontinuum has a noise floor ~25dB higher than the Ti:Sapphire and contributing to higher background noise in the OCT image.

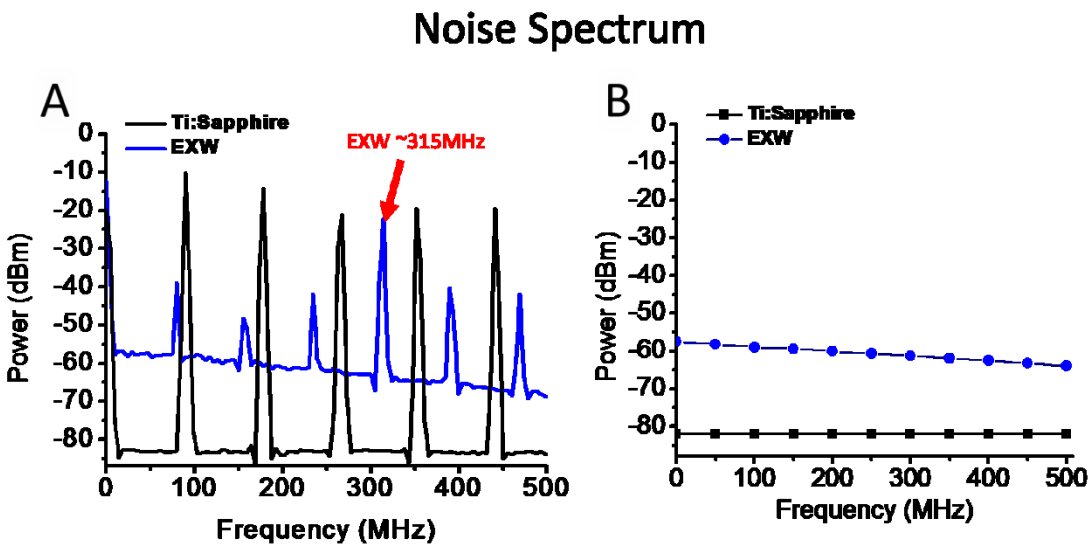

Figure 3.10 Noise characterization of Ti:Sapphire and SC.

Noise spectrum measurements of Ti:Sapphire compared against supercontinuum. (A) Noise frequency spectrum denoting the repetition rate of the laser, Ti:Sapphire ~80 MHz and supercontinuum EXW ~315 MHz. (B) Noise floor measurements, Ti:Sapphire has a flat noise floor of -80dBm over the frequency range, while the supercontinuum has a higher noise floor closer to DC ~-58dBm to -64dBm at 500 MHz.

3.8.2 Shot Noise and Laser Excess Noise (Relative Intensity Noise) [100]

Shot noise arises from the fundamental photon nature of light and describes the fluctuations in the detected number of photons arriving at a photodetector. In OCT it is imperative that the system operates within the shot noise limited regime. Operating in the shot noise limited range enables the phase of the interference signal to be preserved by minimizing the contributions of other sources of noise.

The shot noise for a SD-OCT system can be described by the following [152]:

$$\sigma_{shot}^2 = \frac{\eta\rho\tau}{h\upsilon_0}\frac{P_0}{N}(\gamma_s R_s + \gamma_r R_r). \quad 3.3$$

In Equation 3.3, η is the quantum efficiency of the detector, ρ is the spectrometer efficiency, τ is the exposure time of the CCD within the spectrometer, $h\upsilon_0$ is the energy of the photon corresponding to the central frequency of the light source (h is Plank's constant and υ_0 the central frequency), P_0 is the optical power incident on one detector pixel (calculated from the spectral resolution), N is the number of pixels illuminated, γ_s and γ_r are the portion of light leaving the interferometer from the sample and reference arms, and R_s and R_r the reflectivity of mirrors in the sample and reference arms (assumed to be 1).

Figure 3.11 A and B are log-log plots of the noise versus reference arm level in CCD counts for the Ti:Sapphire laser and the supercontinuum laser, respectively. The plot was generated by collecting 30-50 reference arm spectra for reference arm levels ranging from near saturation of the CCD until no light was able to be detected by the CCD. The standard deviation of a given pixel over 2048 A-lines was calculated and plotted with respect to the reference arm level in units of CCD counts.

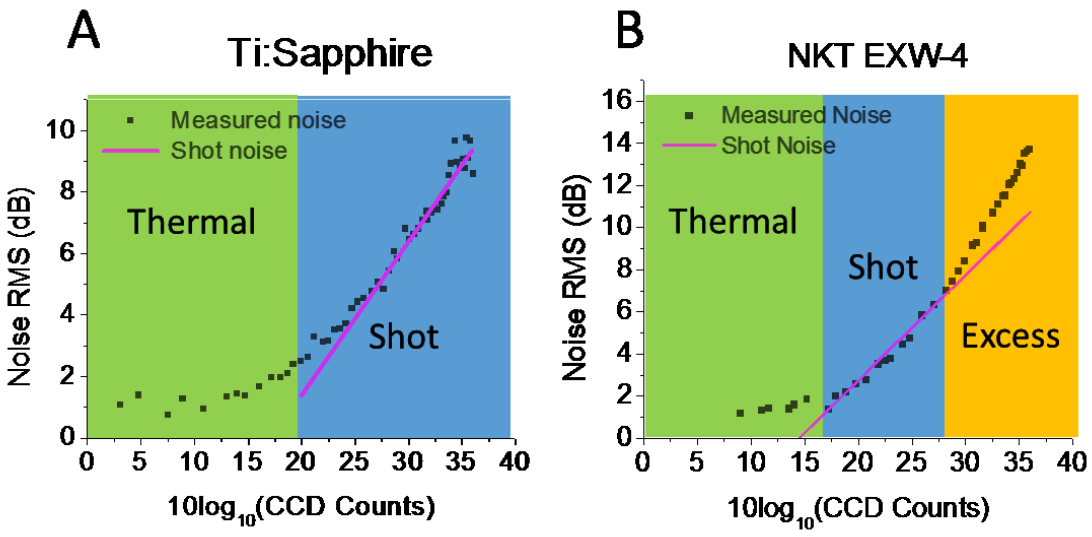

Figure 3.11 Measured shot noise limits for OCT sources.

(A) Ti:Sapphire and (B) NKT supercontinuum. **T**he light green region denotes the thermal or Johnson-nyquist noise, the light blue region is the optimal shot noise limited region and the nude colored region in (B) denotes laser excess noise.

There are three regions shown in Figure 3.11 B, a thermal noise region in light green, a shot noise limited region in light blue, and the excess noise region in beige. The thermal noise region arises from the heating effects of the CCD sensor, while the excess noise region arises from laser intensity fluctuations of the source. According to Figure 3.11, it is clear to see that the Ti:Sapphire has a much broader shot noise limited range compared with the supercontinuum which has two implications. Firstly, a broad shot noise limited range ensures the ability to increase gain in the reference arm allowing an increase in the signal-to-noise ratio. Secondly, as long as the supercontinuum is operated

within the shot noise limited range, the increased noise due to laser excess noise can be avoided [100].

3.9 *Results*

This section will present results from an endoscopic OCT system employing both the supercontinuum and Ti:Sapphire lasers in a sample of *ex vivo* rat colon.

3.9.1 Endoscopic Imaging System

The endoscopic imaging system used to collect the following images has been described above. The catheter[4] was similar to the catheter described in this chapter but was not the same one.

3.9.2 Experimental protocol

All imaging was performed under a protocol approved by the Animal Care and Use Committee at the Johns Hopkins University. For *ex vivo* rat colon imaging, the tissue was first dissected and flushed with saline to remove stool. The colon was then kept hydrated in a petri dish with saline during the imaging procedure.

---

[4] The catheter employed to test image quality between the two sources was based on the same general architecture as described in section 3.3, with two differences due to the lack of availability of the 900 μm diameter motor and miniature custom diffractive lens. This catheter employed a 1.5 mm diameter micromo motor from Faulhaber making the total outer diameter of the catheter 3.1 mm (with the protective plastic sheath) and the lens design simply omitted the diffractive element. The catheter had a working distance of 700 μm from the plastic sheath, a lateral resolution of 8.44 μm and was able to achieve an axial resolution of 2.8 μm (without the diffractive lens). Total round-trip loss in the catheter was ~2.96 dB.

The first set of images were acquired with the Ti:Sapphire laser and after the entire volumetric dataset had been acquired, the laser source was exchanged and reference arm level adjusted to ensure operation in the shot noise level.

To perform endoscopic imaging, the catheter was deployed into the colon from the distal part to the most proximal part. The colon was pinned to the petri dish to avoid movement during pull-back. The images shown in Figure 3.12 were acquired at 8.5 frames per second with each frame consisting of 8k A-lines without sacrificing image quality or causing non-uniform rotational distortion and pull-back was performed with a pitch of 20 μm over a length of 200 μm. The radial direction was oversampling in order to preserve the fine microstructural details of the colon, such as crypts.

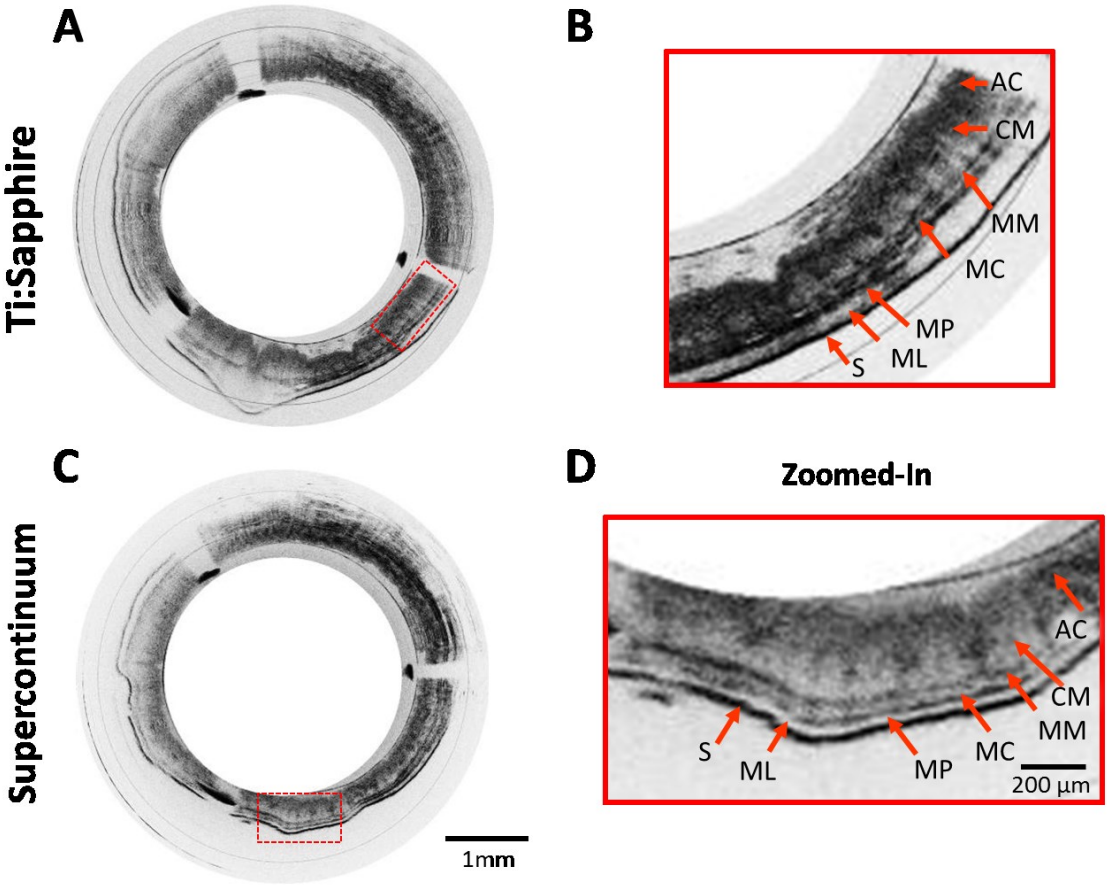

Figure 3.12 Image quality comparison with *ex vivo* rat colon.

(A) Cross-sectional image of *ex vivo* rat colon acquired with supercontinuum with (B) zoomed-in region corresponding to red dashed box in (A). (C) Cross-sectional image of same *ex vivo* rat colon acquired with Ti:Sapphire with (D) zoomed-in region corresponding to red dashed box in (C). AC: absorptive cells, CM: colonic mucosa, LP: lamina propria, MM: muscularis mucosae, SM: submucosa, MC: circular muscle, MP: myenteric plexus, LM: longitudinal muscle, S: serosa.

3.9.3 Image comparison

Figure 3.12 A and C are representative cross-sectional images acquired from the Ti:Sapphire and supercontinuum respectively. One of the ways in which the images can be assessed is compared is by the achievable resolution and detectable image structures. The catheter was able to achieve 2.8 μm with both light sources. Additionally, the zoomed-in regions shown in Figure 3.12 B and C demonstrate the capability to distinguish several layers within the colon such as the absorptive cell layer, colonic mucosa, lamina propria, muscularis mucosae, submucosa, circular muscle layer, myenteric plexus, longitudinal muscle layer and the serosa. By maintaining the

Another feature of both images is the comparable background noise and intensity distribution. By ensuring that the supercontinuum operated within the shot noise regime, the overall background noise and image quality is very similar to the Ti:Sapphire, showing that the supercontinuum can be used as a portable substitute for the bulky femtosecond laser.

3.10 *Future Directions: High Speed Endoscopic Imaging*

This chapter focused on implementation of a high speed, ultrahigh resolution endoscopic OCT system and it was shown that by using an 800 nm broadband light source with an SD-OCT configuration, an ultrahigh axial resolution ~2.8 μm could be achieved. The miniature micromotors employed for distal scanning endoscopes would significantly high frame rates from 200 frames-per-second for the Namiki motor employed in this dissertation to 3200 frames-per-second for the AC motor from Kinetron[50]. The major limiting factor this far is the maximum A-scan rate of the CCD (70kA-scans-per-second).

Many high speed endoscopic systems have been demonstrated using 1300 nm swept source OCT engines. These swept source OCT engines are able to achieve A-scan rates from several hundreds of kHz[43, 45, 46] to 20.8 million A-scans per second [44], leading one to believe that transitioning to swept source OCT at 800 nm may seem like the best option to achieve the highest A-scan rate and eventual frame rate.

800 nm swept source OCT systems have only recently been developed over the last decade and are still limited in their capabilities. There are three major drawbacks for swept source OCT engines around 800 nm, 1) limited sweep range usually less than 50 to 60 nm [39-41, 155-159] 2) low output powers, usually less than 10 mW, but sometimes 26 mW or greater has been demonstrated[36, 159] and 3) poor axial resolutions (> 6.6 μm). 800 nm swept source OCT is still limited due to the lack of broadband light sources and fiber optic components.

Thus in order to achieve ultrahigh axial resolutions (<3 μm) it is necessary to employ SD-OCT systems Currently the state of the art high speed SD-OCT systems employ CMOS cameras and are capable of acquiring data from up to 312,500 Ascans-per-second at 800 nm [30] with a single camera, or 500,000 Ascans-per-second with dual cameras [31], 120,000 Ascans-per-second at 1050 nm [160] or up to 184,000 Ascans-per-second at 1310 nm by employing Doppler induced phase shifts[161] .

The SD-OCT system employed in this dissertation has the capability to be upgraded so that the A-scan rate can be effectively doubled. This can be done by replacing the current linear CCD array in the spectrometer with a Basler spL-4096-

140km camera which can deliver up to 140,000 Alines at a full 4k pixel resolution and can acquire data up to 330,000 Ascans-per-second by reduction of the pixel resolution.

3.11 *Conclusions*

This chapter built upon the foundations laid by chapter 2, and focused on the practical choices associated with implementing an endoscopic SD-OCT system for high speed, ultrahigh resolution imaging. The high speed, ultrahigh resolution, endoscopic SD-OCT system introduced in this chapter will be employed throughout the rest of this dissertation. In context, in the following chapter, chapter 4, the focus will be on implementation of an algorithm to correct for non-uniform rotational distortion in distal scanning catheters. Following chapter 4, chapters 5 and 6 will be dedicated to biomedical applications on pulmonary imaging in a sheep model and colorectal cancer imaging in a murine model. The systems employed for image acquisition in the aforementioned models will be based on the system described in this chapter.

Chapter 4 Non-uniform Rotational Distortion Correction

4.1 *Introduction*

This chapter will focus on the image processing algorithms that can be applied to OCT images for non-uniform rotational distortion (NURD) correction in endoscopic imaging. The chapter will begin with a brief overview of types of NURD that have been discussed in the literature and the mechanism by which they occur and algorithms that have been developed to correct them. The focus of this chapter will be on stick-slip NURD which has not been well addressed in the literature, and an algorithm to correct for this distortion will be presented with some results from an *in vivo* mouse colon with colon cancer (from Chapter 5).

4.2 *Non-uniform Rotational Distortion (NURD)*

Chapter 3 focused on endoscopic OCT systems and described a distal scanning catheter for side-view imaging endoscopically. One of the major problems in endoscopic OCT imaging is non-uniform rotational distortion (NURD). In general NURD describes a phenomenon where a catheter is not able to acquire samples at equidistant spatial positions in the radial direction due to mechanical or electrical instability. NURD can result in an inaccurate representation of imaged tissue structure, so, it is important to suppress NURD to prevent potential clinical misdiagnoses while enabling high-speed endoscopic imaging.

Both proximal and distal scanning catheters can exhibit NURD however, the origin is starkly unique. In traditional, proximal scanning systems, the entire catheter is mechanically rotated at the proximal end. A proximal scanning catheter must incorporate a torque applying mechanism, such as a torque coil, to transfer rotation from the proximal end to the distal end of the probe. The torque coil is usually hollow and may consist of several layers of oppositely wound coils, in order to effectively deliver rotation. The completed catheter is then encased by a protective plastic sheath to avoid direct contact with the tissue. The protective plastic sheath is also responsible for containing the catheter within a finite space for rotation to occur concentrically within the sheath. In this case, NURD can manifest in the image due to any resistance in the path of the catheter between the catheter and sheath and can be a significant issue when imaging a sample through a tortuous pathway, i.e. small airways in the lungs. Additionally, any lateral displacement of the probe in a larger lumen will cause NURD as well.

Alternatively, distal scanning endoscopes can also exhibit NURD due to instabilities in the miniature micromotor. In order to reduce the overall size of micromotors, feedback mechanisms such as encoders are usually omitted, making it difficult to maintain the rotational velocity. Micromotors can exhibit NURD due to imbalanced load on the shaft of the micromotor, mechanical lifetime or changes in the electrical impedance along the length of the signal drive wires.

The types of NURD described above can be classified into three categories, 1) translation type NURD, 2) stretch-shrink NURD and 2) stick-slip NURD, each of which will be described in more detail in the following sections.

4.2.1 Translational NURD

Translation type NURD refers to non-uniform sampling due to undesired radial motion away from the center of the lumen. While this type of NURD is not strictly non-uniform sampling due to mechanical or electrical instabilities, a portion of the literature for OCT and intravascular ultrasound (IVUS) regarding NURD correction refers to this type of NURD. Translational NURD can occur due to significant motion of the catheter inside a lumen during an imaging procedure because of physiological motion artifacts such as respiration or heart rate. Another situation where translational NURD may arise is when imaging a lumen greater than the outer diameter of the catheter, such that the catheter is not in a fixed position. Either of the two aforementioned situations can cause the catheter to shift off-center preventing the catheter from uniformly sampling the lumen wall. Usually, this non-uniform sampling does not induce significant image artifacts and the main concern is compensating displacement between adjacent image frames to register sequential images for volumetric scans [162-166], correct motion artifacts for thermal strain imaging[167], or potential flow imaging[168].

This type of NURD has mainly been corrected through image registration techniques with cross-correlation of A-lines between adjacent frames [162, 163, 165, 166]. In certain cases, image features can be used as landmarks for registration such as stents in some intravascular OCT applications[164] or motor signal drive wires for distal scanning catheters[166]. Use of landmark features usually provide much better registration in the longitudinal direction compared to cross-correlation without landmarks, mainly due to

sparse sampling in the longitudinal direction, which can cause inaccuracies in the cross-correlation method making it difficult to use for pull-back data.

4.2.2 Stretch-Shrink NURD

Stretch-shrink NURD is named for its appearance in OCT images. Stretch-shrink NURD results from rotational velocity changes that are on the same time scale as the frame rate. As discussed earlier, proximal scanning catheters can experience significant resistance along the path of the catheter[169] due to a tortuous path. Resistance can cause the distal end to be stuck in a certain position before significant torque is built up and applied to the catheter after which the spring action causes the distal end to rotate to an unknown position and attempt to uniformly collect data again. Often times the catheter may not sample the remaining circumference uniformly and the result is a portion of the circumference that is densely sampled, appearing compressed, while another is sparsely sampled, which appears stretched, yielding a distorted image. Thus stretch-shrink NURD is frequently an issue in proximal scanning catheters and was originally discussed on the basis of intravascular ultrasound probes [169-171].

One of the few algorithms devised to help alleviate stretch-shrink NURD was only recently published [172]. The basis of the algorithm was to use fiducial markers at known angular positions to perform spline interpolation of the data in between the known locations. The catheter employed to demonstrate this algorithm was a distal scanning catheter and the edges of the distal enclosure, where signal void regions begin and end, were used as fiducial markers. The major drawback to this approach was in the

requirement for fiducial markers. Proximal scanning catheters that would not naturally have fiducial markers would need to be modified in order to implement this algorithm.

Ultimately, the algorithm performed well and was able to be used for vascular visualization of *in vivo* human esophagus data.

4.2.3 Stick-Slip NURD

Stick-slip NURD is caused by abrupt and rapid changes in rotational velocity that are on the order of the A-scan rate. Stick-slip NURD arises in mainly distal scanning endoscopes where an imbalanced load on the motor shaft, or motor instabilities, can cause the motor to momentarily halt and then rotate again, causing stick-slip NURD. The halted locations do not have any deterministic pattern but are usually preserved in the same spatial locations for a specific micromotor at a given rotational velocity, as can be seen in Figure 4.1.

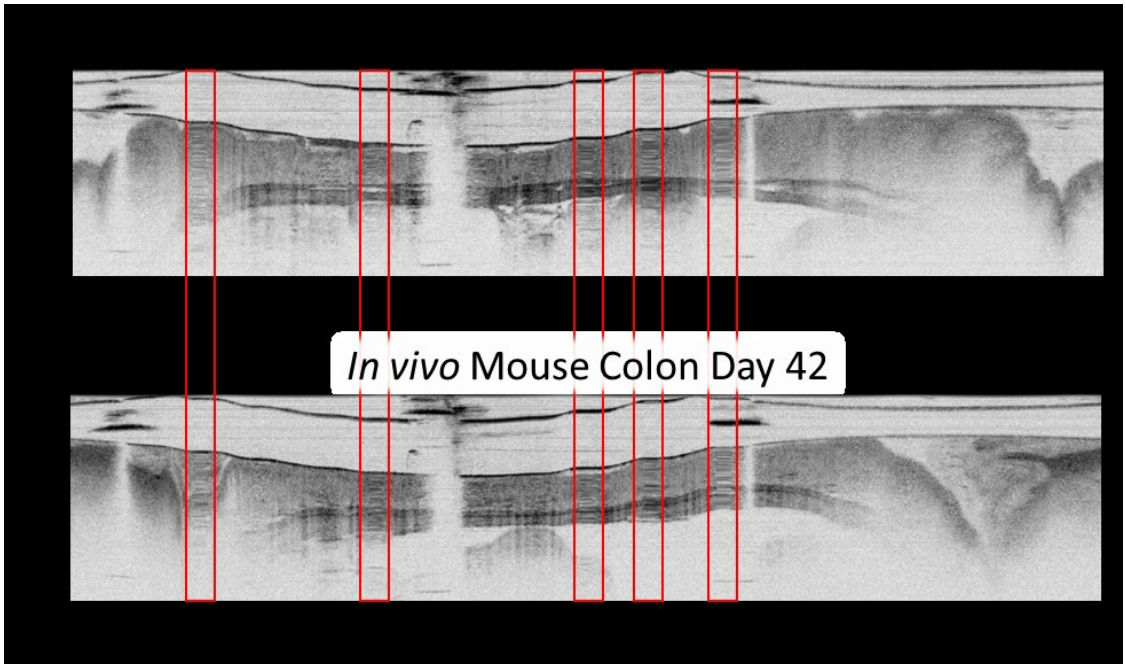

Figure 4.1: Spatial locations of NURD regions between datasets.

Rectangular, unwrapped, endoscopic OCT images acquired with the same imaging catheter, and same animal at two different time points within the course of the experiment[5]. The dataset from which (A) was selected was acquired one week prior to the dataset from (B). The regions highlighted by red line boxes demonstrate that the spatial locations of stick-slip NURD are preserved for a specific micromotor and catheter.

Stick-slip NURD regions are short segments with minimal transition zones between halted and uniformly sampled regions. Figure 4.2 A is a representative cross-sectional image of *ex vivo* rat colon that exhibits stick-slip NURD in several positions, one of which is enclosed in a box with a red dashed line. Next to the cross-sectional image, in Figure 4.2 B, is a zoomed-in view of the boxed region from Figure 4.2 A. There are two NURD sections marked as N_a and N_b and one section marked T.

[5] The time course experiments are described in further detail in chapter 6 on colon cancer imaging in a murine model.

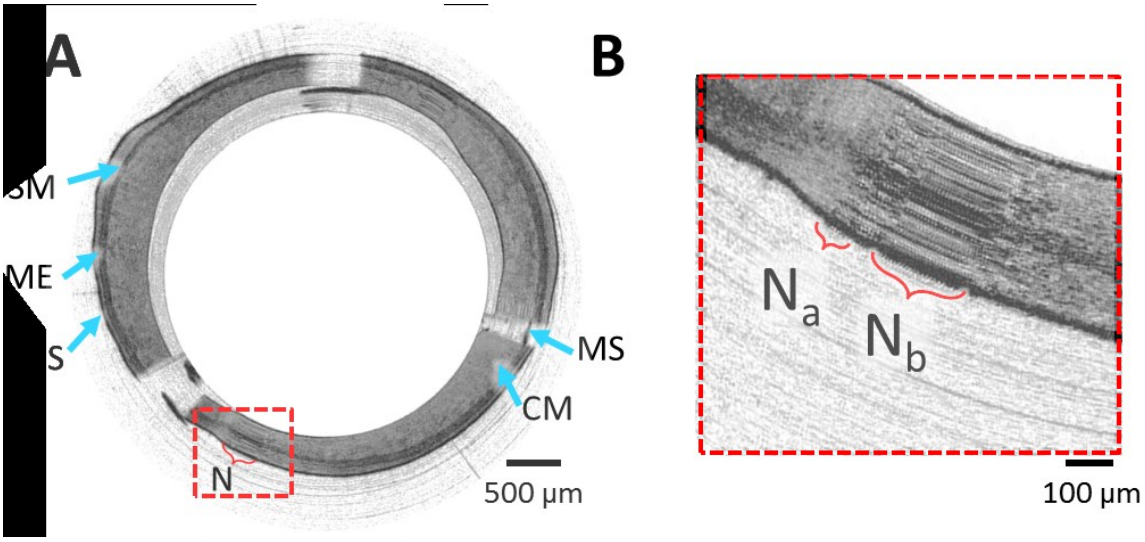

Figure 4.2: Example of stick-slip NURD from image of *ex vivo* rat colon.

(A) Representative cross-sectional image from ex vivo rat colon showing non-uniform rotational distortion labeled with N in the boxed region marked by red dashed line border. The labeled colon wall structures include, MS – metal strut of distal enclosure, CM – colonic mucosa, SM – submucosa, ME –muscularis externa, and S – serosa. (B) Shows a zoomed-in view of the boxed region in (A) explicitly shows non-uniformities that have been labeled with Na and Nb to exemplify two regions of repeated A-lines composing of NURD and a region labeled T as the transition zone between Nb and equidistant sampling.

The remarkable aspects of this zoomed-in image are three-fold. Firstly, it is important to note that between the uniformly sampled region and the halted NURD region N_a, there is no transition zone, whereas between N_b and the resumed uniform sampling is a short transition zone. This indicates the directionality of scanning as counterclockwise because

the motor requires little to no time to halt and some time to increase acceleration until the rotational velocity is reached. Secondly, one NURD segment may consist of a couple of clusters of repeated A-lines as seen and marked by N_a and N_b. Thirdly, the transition region is a short segment, similar to segment N_a. The short NURD and transition regions are the key to the algorithm (described below) employed to correct stick-slip NURD regions.

4.3 *Algorithm for NURD Correction*

This section will focus on the algorithm developed to correct OCT images with stick-slip NURD. In order to correct the images, the first step is to identify and exclude all unwanted A-lines that consist of NURD regions. In order to identify and isolate the NURD regions we need to find a feature which helps identify the region. In Figure 4.2 B, the zoomed-in region demonstrates that stick-slip NURD manifests as repeated A-lines where the signal intensity for a given wavenumber or depth pixel does not vary between adjacent A-lines. Figure 4.3 further examines this phenomenon.

Figure 4.3 is a plot of a single wavenumber, *k*, against A-line number for the entire image frame (shown in yellow), superimposed on the interferogram of the entire frame (in grayscale). The red arrows in Figure 4.3 point to prominent NURD regions where the signal intensity variation is low, as seen by the plateaus or slow variations in the plot and the nearly unchanging interference pattern in the interferogram.

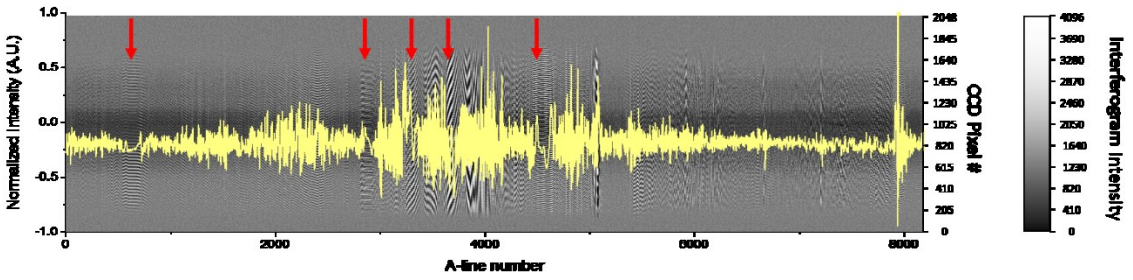

Figure 4.3: Low spatial frequency of NURD regions.

Yellow: plot of a single wavenumber, k, along all A-lines within a single image frame. Plot is superimposed on the corresponding interferogram of the image frame. Red arrows point out prominent NURD regions where the plot shows a plateau and the interferogram has repeated A-lines. The left Y axis shows the normalized intensity for the plot, while the Y axis on the right shows the CCD pixel number for the interferogram in the background with the colorbar corresponding to the intensity values in the interferogram.

The slow variations in NURD regions can help to isolate NURD regions from the surrounding equidistant sampled A-lines. These slowly varying regions will exist in the low spatial frequency range of the raw OCT interferogram and can be isolated by performing spatial frequency filtering on the interferogram prior to performing the Fourier transform.

One concern with filtering out low spatial frequency components from the raw interferogram is that some tissue structure may also contain low spatial frequency

components. Thus the algorithm needs to be able to identify and remove NURD regions without sacrificing valuable tissue relevant A-lines within the low spatial frequency range.

The algorithm employs a mask based method, wherein a mask is generated to highlight NURD regions and used on the entire dataset to remove A-lines corresponding to regions with NURD.

The image processing flow chart is shown in Figure 4.4 with five steps. The first step is to perform high pass filtering (HPF) on the raw SD-OCT data $I(k,x)$ prior to performing the FFT, i.e. $I_1(z,x) = FFT\{HPF[I(k,x)]\}$. High pass filtering was performed with a Butterworth filter to avoid ripples in the pass-band or stop-band. The HPF cutoff frequency was determined based on the spatial frequency corresponding to the length of the shortest NURD cluster. In general the highest spatial frequency,f_{max}, can be described as follows:

$$f_{max} = \frac{\#\ Alines/frame}{2(Circumference_{focal\ plane})}. \tag{4.1}$$

For the image frame shown in Figure 4.2 A, there are 8192 A-lines per frame and the circumference is 11.6 mm at the focal plane of the catheter yielding a maximum spatial frequency of 353 mm^{-1} according to Nyquist sampling theorem. Figure 4.2 B has two NURD clusters labeled N_a and N_b. N_a is the shortest NURD cluster in the image with approximately 13 repeated A-lines corresponding to a spatial frequency of 54.3mm^{-1}, i.e. ~15% of the spatial frequency range of the raw OCT image data. The high pass filter cutoff frequency will be 15% of f_{max} and the lowest 15% of the spatial frequency range will be filtered out. The cutoff frequency will determine how much of the low spatial

frequency components will be removed or how sharply NURD regions are filtered out. By identifying the shortest contiguous region of NURD visible within the image, the cutoff frequency is set to a value that will filter out NURD regions and retain relevant image data.

In order to better characterize the behavior of the cutoff frequency, the spatial frequency corresponding to NURD regions was measured with varying frame rates and compared to 15% of the maximum spatial frequency captured from the OCT image. The comparison is shown in figure 4.4. The red data points are calculated as 15% of f_{max} from equation 4.1 and the black data points correspond to the spatial frequencies calculated from the shortest NURD regions measured in an OCT B-frame for a given rotational velocity. Each black data point is the average of the (NURD) spatial frequency measured over 20 OCT B-frames.

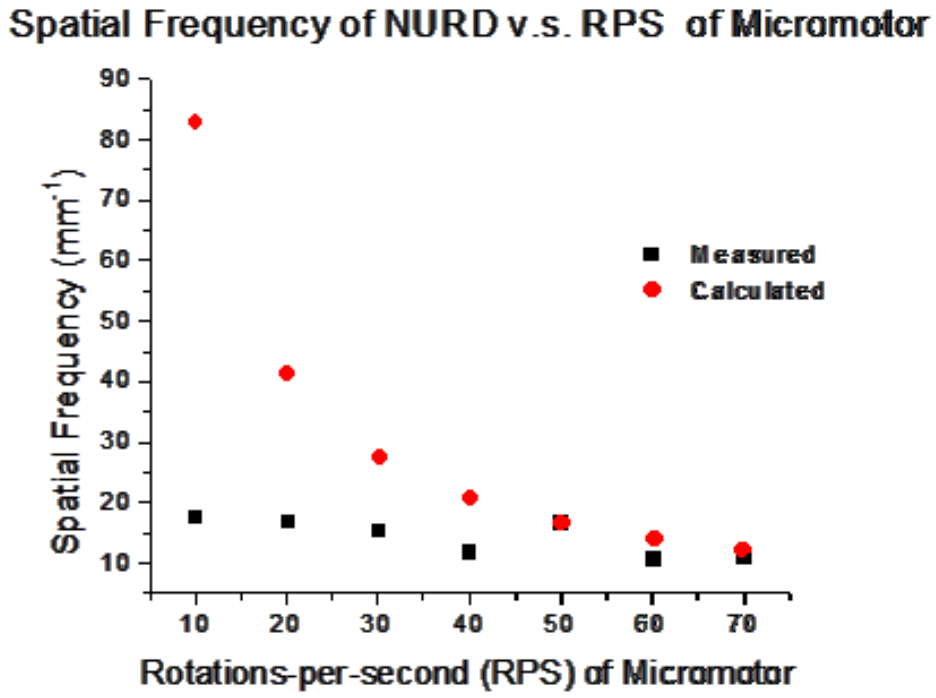

Figure 4.4 Upper spatial frequency limit of NURD regions versus rotational velocity of the micromotor.

The red dots denote the spatial frequency corresponding to 15% of the maximum spatial frequency spectrum present in the OCT B-scan image. The black dots denote the measured spatial frequency upper limit corresponding to the shortest NURD region for a given rotational velocity. Each data point in the measured curve corresponds to the spatial frequency averaged over the NURD regions identified in 20 OCT B-scans for a given rotational velocity.

From these data points, it can be seen that the shortest stick-slip NURD region exists in the lowest 15% of the maximum spatial frequency captured in the OCT image. This relationship was also found to be representative between endoscopes of the same basic design and architecture i.e. endoscopes with a micromotor and similar load due to micro-mirror.

In order to illustrate the method by which a mask is formed, all images in Figure 4.5 are the unwrapped, rectangular images (and plots) corresponding to each of the five steps in the algorithm. Figure 4.5 A shows the raw OCT image data $I(k,x)$ obtained from the endoscopic SD-OCT system and Figure 4.5 B shows the corresponding high pass filtered image $I_1(z,x)$. The white signal void regions in Figure 4.5 B are the NURD regions that have been filtered out.

The second step aims to take into consideration any low spatial frequency components relevant to tissue structure that could have been filtered out in the first step. In order to minimize this loss, low pass filtering (LPF) is performed on the raw OCT data prior to performing the FFT, i.e. $I_2(z,x) = FFT\{LPF[I(k,x)]\}$. The cutoff frequency for the LPF

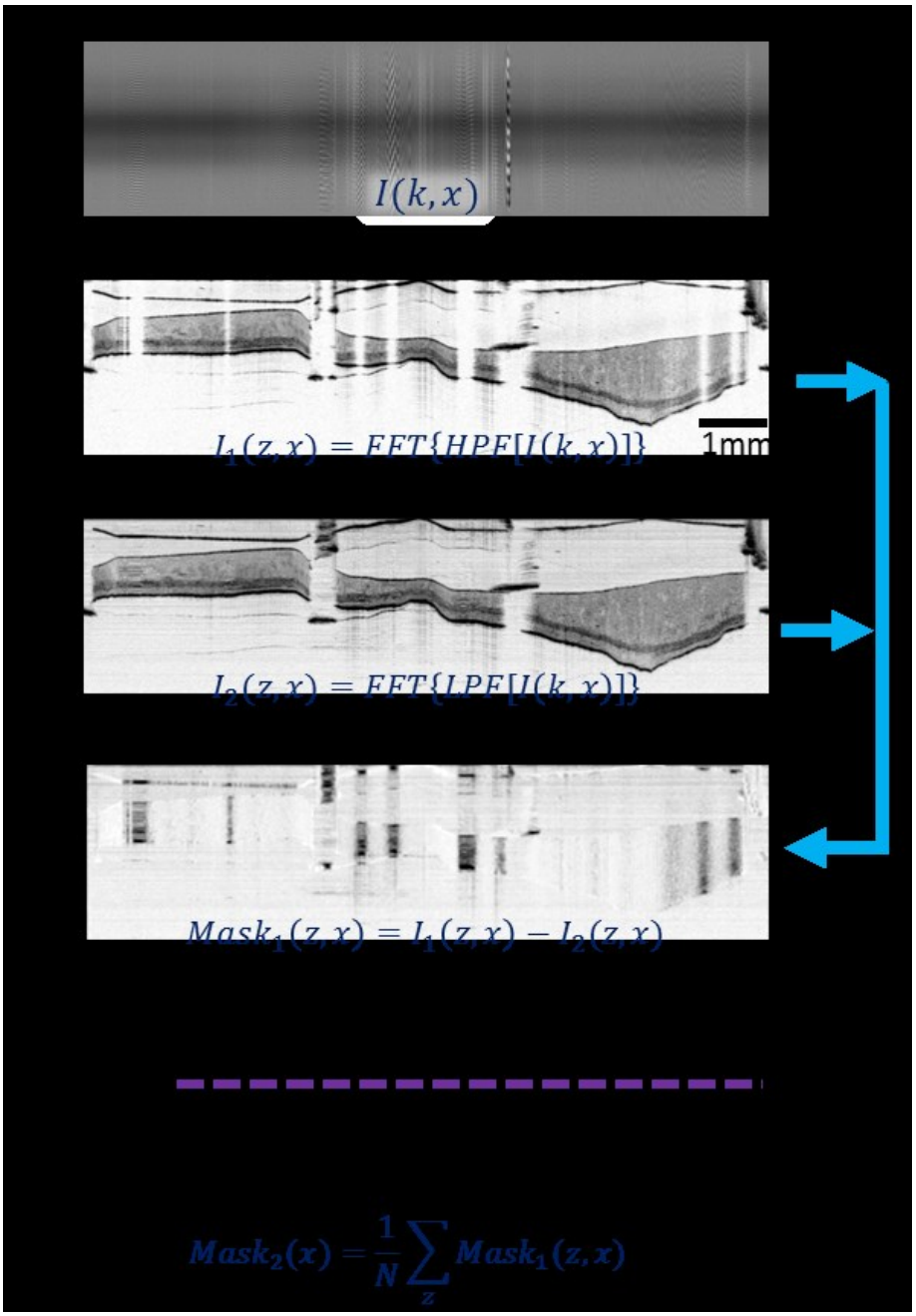

Figure 4.5: Flowchart representation of NURD correction algorithm.

(A) The raw spectral interference fringes in one frame acquired by the SD-OCT system. (B) and (C) Images I_1 (z, x) and I_2 (z, x) resulting from high-pass and low-pass frequency filtering of the raw OCT image data, respectively, prior to performing Fourier transform. (D) $Mask_1$ obtained

after performing image subtraction of the high-pass and low-pass frequency filtered images (i.e. $Mask_1 = I_1 - I_2$). (E) $Mask_2$ obtained from averaging every A-line along the imaging depth from *Mask1*. The purple dashed line is an example of an appropriate threshold level for this dataset. (For the purposes of illustrating this algorithm, the cross-sectional images are shown in Cartesian view instead of polar view.)

should smooth the transition region between equidistant sampling and NURD regions to ensure that the regions are sharply removed during subtraction. The LPF cutoff frequency was empirically determined to be 85% of f_{max}, the result can be seen in Figure 4.5 C.

I_1 and I_2 are images obtained from the FFT of HPF and LPF OCT interferograms. Each image excludes some part of the frequency content in the image, by taking the difference of these two images, i.e. $Mask_1 = I_1(z,x) - I_2(z,x)$, an image that accurately identifies the NURD regions has been formed. Essentially, all relevant tissue structure from the LPF image is removed from the HPF image. Since the HPF image contains only relevant tissue structure with signal void areas corresponding to NURD regions, the result is NURD regions from the LPF image as can be seen in Figure 4.5 D.

The most important information gained from $Mask_1$ is the location or A-line number in the image frame of NURD related A-lines. In order to extract this information and employ it, $Mask_1$ is collapsed into a single array of values by averaging along the imaging depth. Meaning that $Mask_2 = \sum_z Mask_1(z,x)/N$, where N is the total number of pixels in an A-line, as shown in Figure 4.5 E.

The values of $Mask_2$ will be lower for NURD regions than tissue regions due to the fact that creating $Mask_1$ removed most tissue-relevant structures except with NURD (of low spatial frequency) remaining. As shown in Figure 4.5 E, $Mask_2$ has a small negative value (between 0 and -0.1) for tissue relevant, or equidistantly sampled A-lines where NURD does not occur. The small negative value is due to the decrease in background noise from the high-pass filter when computing $I_1(z, x)$. When the value of $Mask_2$ drops rapidly to below -0.25, the A-lines correspond to NURD regions. A threshold is set for $Mask_2$, at -0.2, marked by the purple dashed line in Figure 4.5 E. $Mask_2$ is a map of the spatial locations of NURD regions for the original unfiltered OCT image as well as any images within the same dataset.

Finally, a corrected image is formed by rejecting A-lines at spatial location x as identified in $Mask_2$ where the value dips below the threshold. This method can be applied to all images a volumetric pull-back scan with the same mask.

4.4 *Experimental Methods*

4.4.1 Endoscopic Imaging System

The endoscopic spectral domain OCT (SD-OCT) system is as shown in Figure 3.5 A. The light source employed was the home built Ti:Sapphire laser with a central wavelength of 830 nm and a spectral bandwidth of ~ 150 nm. The OCT catheter is pictured in Figure 3.3 D and was able to achieve an axial resolution of 2.8 μm (in air) and a lateral resolution of 7.6 μm with a working distance of ~200 μm.

4.4.2 Experimental Protocol

Animal model imaging was performed under a protocol approved by the Animal Care and Use Committee at the Johns Hopkins University. The animals were first anesthetized with a mouse mix (100mg/kg Ketamine and 10 mg/kg Xylazine) injected intraperitoneally, ensuring that the mouse remained dormant for ~45 minute. After the animal was anesthetized, the catheter was inserted in to colon a maximum insertion depth of 4 cm.

Endoscopic imaging was performed at 20 frames-per-second with 3k A-lines per frame and pull back was performed with a pitch of 20 μm between each frame from the point of insertion until the catheter was completely outside the animal. The overall pull-back length varied based on amount of insertion into the colon (2 to 4 cm). The algorithm was applied to determine a suitable mask which was then applied to the entire volumetric pull-back scan.

4.4.3 Discussion

Figure 4.6 shows an example of original and corrected *in vivo* images of mouse colon, respectively. The images are displayed as the flattened, rectangular, averaged projection view of the volumetric pull-back.

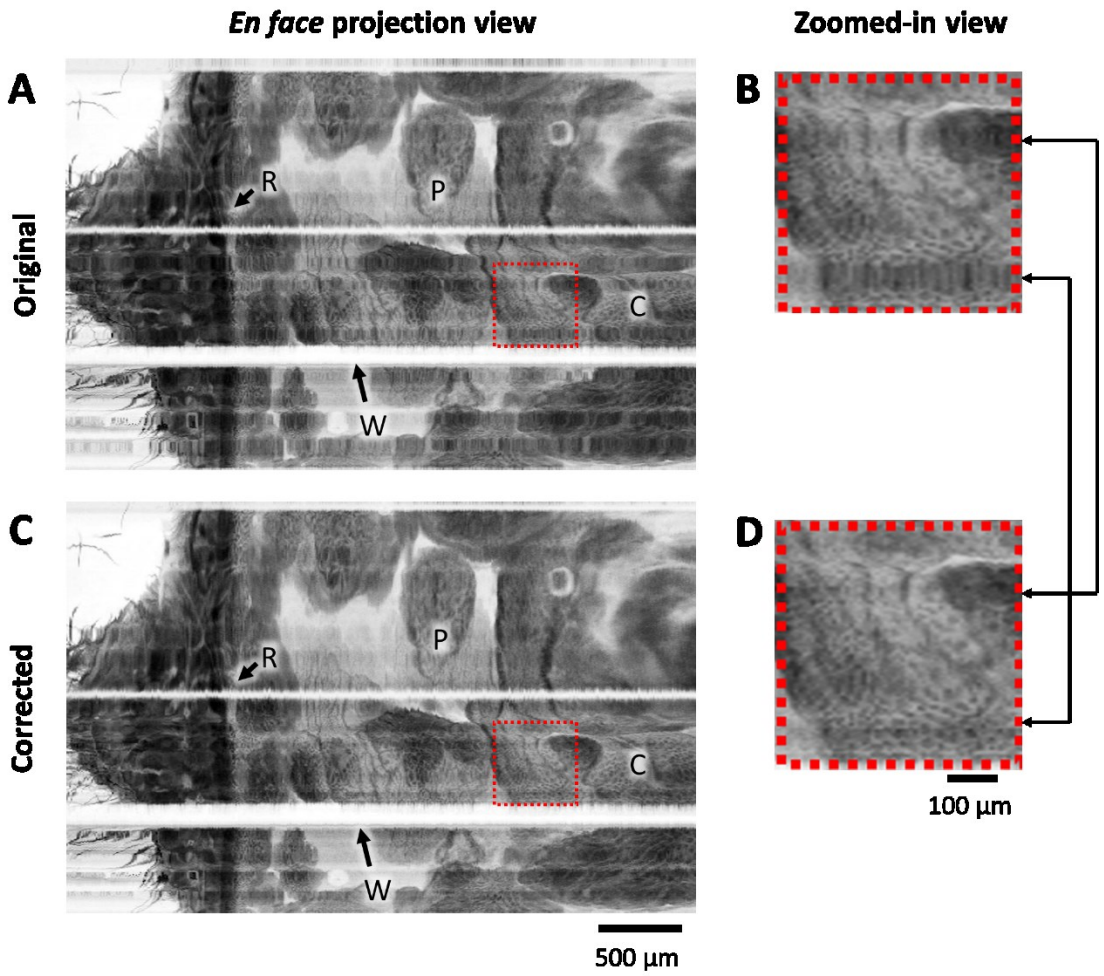

Figure 4.6: NURD corrected *en face* projection images of *in vivo* mouse colon.

(A) Original pull-back scan with (B) zoomed-in region. (C) The NURD corrected pull-back scan and (D) corresponding zoomed-in region. The red arrows between the zoomed-in images in (B) and (D) indicate two NURD regions, one large stick-slip segment and another more difficult to detect segment have been corrected with this algorithm. R: rectum, W: Wire or enclosure strut, P: polyp, and C:crypts.

Figure 4.6 B and D are zoomed-in regions of the original and corrected areas enclosed in red. On the right of Figures 4.6 B and D are two black arrows pointing to stick-slip NURD segments and the corresponding corrected regions. Additionally, several structures or features are labeled in the image, colonic crypts, signal void region due to strut or wire, beginning of rectum, and potential polyps.

This algorithm is able to eliminate many A-lines with redundant information and reform the cross-sectional image with the remaining unique A-lines. One of the benefits of this algorithm is that all cross-sectional images within a dataset can be corrected with the same mask. Additionally, as it was illustrated in Figure 4.1, the spatial locations of stick-slip NURD are preserved between volumetric pull-back scans for the same catheter (with same micromotor) at a given speed.

Another advantage of this algorithm is the flexibility that it entails. This algorithm can be applied on an as-needed basis. In the event that stick-slip NURD only presents in several frames or a short segment of the volumetric scan, the algorithm can be applied on distorted frames only.

Finally, the high pass filter cutoff frequency should be adjusted once based upon the shortest NURD segment present in the dataset. This is a one-time cost for the use of this algorithm, after which the mask can be applied to the entire dataset and future datasets from the same catheter at a given speed.

Thus far, we discussed the several advantages of this algorithm however, under certain conditions such as when stretch-shrink NURD (also known as motion blur) coexists with stick-slip NURD, the performance of this algorithm suffers greatly.

Temporally, stick-slip NURD consists of rapid changes in rotational velocity on the order of the A-line acquisition time. Spatially, it then manifests in localized regions of the imaging frame. Stretch-shrink NURD occurs when changes in the rotational velocity are on the same time-scale rotational velocity or the time period of a frame acquisition. Stretch-shrink NURD can affect a portion or the entire imaging frame.

Stretch-shrink NURD contaminates the low spatial frequency ranges due to two reasons, 1) the sparsely sampled stretched region which will appear blurred and 2) the transition zones between the stretched and compressed regions will appear more continuous and possibly longer than the short transition zones in stick-slip NURD. Contamination of low spatial frequency ranges will prevent the algorithm from being able to isolate stick-slip NURD regions rendering it ineffective, however if stretch-shrink NURD is corrected through resampling or interpolation, any residual stick-slip NURD may be able to be corrected with this algorithm.

4.5 *Conclusions*

This chapter presented NURD as a common distortion that appears in endoscopic OCT images and described NURD by identifying three types of NURD in literature; 1) translational NURD, 2) stretch-shrink NURD and 3) stick-slip NURD. By understanding the type of NURD and the physical reasons for its occurrence, this distortion can be corrected. Translational NURD was able to be corrected through image registration with landmarks[164, 166] and cross-correlation algorithms[162, 163, 165, 166], while stretch-shrink NURD is a more difficult problem, requiring the data to be resampled uniformly. Although adequate resampling was demonstrated, it was only demonstrated with a distal

scanning catheter where the algorithm was aided with a priori information using fiducial markers based on the distal end enclosure [172]. Finally, stick-slip NURD was not yet addressed in the literature, thus an algorithm to correct this type of NURD was presented in this chapter.

Results were demonstrated on a dataset acquired from *in vivo* mouse colon in a cancer model (further discussed in chapter 6), showing that for a one time cost, many datasets from the same catheter can be corrected. This algorithm will be used (on an as needed basis) in conjunction with the OCT catheter described in chapter 3 in the following two chapters, where results from *in vivo* imaging of small airways in sheep (chapter 5) and *in vivo* imaging of a rapid colon cancer model in mice (chapter 6) will be presented.

Chapter 5 Pulmonary Imaging of Small Airways

5.1 *Introduction*

This chapter will focus on endoscopic imaging results obtained with the high speed, ultrahigh resolution endoscopic OCT system described in chapter 3. The first part of this chapter will focus on the significance of small airway imaging with respect to airway diseases such as obstructive lung disease (OLD) and the role of OCT in the context of pulmonary imaging studies. The rest of the chapter will focus on the imaging studies performed with our high speed, ultrahigh resolution endoscopic OCT system, specifically *in vivo* imaging of small airways in eight sheep. The goals were to be able to perform direct visualization of airway smooth muscle and correlate *in vivo* airway imaging with *ex vivo* histology.

5.2 *Obstructive Lung Disease*

Obstructive lung disease (OLD) is characterized as a respiratory disease in which airways are obstructed making it difficult to empty air from the lungs as opposed to filling lungs (as in restrictive lung disease where lungs cannot be adequately expanded)[173]. Some of the diseases that fall under the classification of OLD are bronchitis, bronchiectasis, chronic obstructive pulmonary disease (COPD) and asthma. Our interests lie in understanding and possibly quantifying tissue component changes in the airway wall in COPD and asthma, which will be discussed further in the following sections. It is thought that both COPD and asthma may have preclinical changes in small airways (<2 mm diameter [174]) that could help diagnose disease early [174-176].

5.2.1 Chronic Obstructive Pulmonary Disease (COPD)

COPD is a disease in which the limited airflow is not reversible with treatment. COPD is diagnosed through spirometry, with the severity dependent on the volume of air that can be forcibly expired (FEV_1) within one second [173, 175, 177]. It is best characterized by a combination of small airway diseases such as obstructive emphysema, chronic bronchitis [178, 179], and chronic bronchiolitis or (peripheral or small airway disease) [180].

In obstructive emphysema there is a permanent enlargement of alveoli with destruction of alveolar walls and chronic inflammation leading to fibrosis. Fibrosis leads to reduced elasticity and difficulty during expiration. Another facet of obstructive emphysema is that the bronchioles remain open during inspiration but collapse during expiration, due to loss of attachments between airways and surrounding parenchyma[181, 182], leading to large amounts of air being trapped in the lungs [178].

Chronic bronchitis, on the other hand, occurs mainly due to inhalation of irritants which cause excessive mucous production and inflammation which also leads to fibrosis of the mucosa. One notable difference in chronic bronchitis is that there is an impaired gas exchange due to mucous production compared [178] to obstructive emphysema where gas exchange may be impaired due to reduced surface area from destroyed alveolar walls [183].

5.2.1.1 Causes

COPD is primarily attributed to inhaled toxins such as cigarette smoke [179, 183] and possibly environmental toxins such as air pollution[184]. There are numerous toxins in

cigarette smoke which irritate the airway causing a chronic inflammatory response [176, 185], which can lead to a buildup of inflammatory cells and that lead to alteration and damage to lung structure causing COPD.

Although COPD is primarily attributed to inhaled toxins, some research suggests that 10% to 20% of non-smokers[183]. This leads to the understanding that there are other factors at play such as second hand smoke, or some genetic susceptibility to airflow obstruction in COPD [186-189]. Finally, there is also some research to suggest that respiratory conditions during childhood [190-192] or poor development *in utero* [193] lead to COPD in adult life due to persistent obstruction of airways or constrained growth of lungs, respectively.

5.2.1.2 Prevalence, Diagnosis, Treatment and Limitations of Current Therapies

According to the American Lung Association estimates nearly 11 million people are affected by COPD and possibly 24 million are yet undiagnosed in the United States alone [194]. Additionally, COPD is projected to be the 5th ranking disease in terms of burden and 3rd in terms of mortality by year 2020 [179] making it an overreaching affliction to a broad population.

The suggested diagnosis and assessment of COPD is through spirometry and patient history. The diagnostic parameter in spirometry is the FEV_1/FVC ratio, which measures the volume of forcibly expired air within 1 second (FEV_1) to the vital capacity (FVC) of the person (volume of air exhaled upon deepest inhalation). When the measured FEV_1/FVC ratio is less than 0.7, the patient is considered to have COPD. As mentioned earlier there are changes in small airways early on in COPD and asthma, however

detecting these changes in through spirometric methods has been difficult because resistance in small airways is a small part of the total airflow resistance [174, 195]. Thus patients diagnosed through spirometry may already have a progressed state of COPD.

Furthermore treatment of COPD presents a challenge because existing treatments such as anti-inflammatory drugs and bronchodilators are much less effective in COPD where the airways may not be as sensitive or responsive to drugs [175, 196].

5.2.1.3 Airway Wall Remodeling in COPD

One of the most active areas of research in COPD is understanding airway wall remodeling in COPD. Specifically, our interest is in understanding the structural composition of the airway wall in small airways in order to better understand morphological changes in COPD.

Persistent inflammation in COPD can lead to remodeling of the airway wall in both large and small airways [197, 198], leading to permanent alterations of structure [174, 199]. In large cartilaginous airways the inner wall is thickened with respect to the severity of inflammation and disease not to the area of smooth muscle [200].

Changes in the small airways include a thicker airway wall, loss of alveolar-bronchiolar attachments, increase in number of goblet cells, possible increase in blood vessel density, fibrosis, metaplasia of epithelium, and striking increase in airway smooth muscle mass [174, 175, 177, 197]. An increase in the overall wall thickness from increased edema, vasculature, collagen or reticular basement membrane thickness can oppose the ability of the airway to shorten, leading it to most likely constrict instead[176].

Thusly, changes that occur in the small airways are notable and significant for study of early disease progression in COPD.

5.2.2 Asthma

Asthma is different from COPD in that episodes are triggered in between symptom-free periods however there are also similarities in the sense that both diseases have some degree of inflammatory response, though unique. Additionally, there is some degree of airway wall remodeling in both diseases.

Unlike COPD, asthma is essentially an inflammatory disease in which there is an immune response to an allergen causing inflammation of the airway. Once asthma is triggered, there are three main processes that occur, 1) inflammation, 2) bronchospasms and 3) mucus secretion [173, 201]. Once the airway is inflamed, there is a hyperresponsiveness and the effect of bronchospasms is more severe causing significantly reduced airflow [178]. This hyperresponsiveness is unique to asthma because it means that the limited airflow is reversible with treatment.

5.2.2.1 Causes

Understanding the underlying causes of asthma is still complex and the major causes of asthma are still disputed [202]. Thus far, the cause of asthma has been attributed almost equally[203] to either allergens or environmental toxins[204], or genetics [205, 206].

5.2.2.2 Prevalence, Diagnosis, Treatment and Limitations of Current Therapies

As of 2010, approximately 25.7 million people, in the United States, have been diagnosed with asthma, with approximately 7 million of those being children aged 17 and under

[207]. Currently, physicians diagnose asthma using the medical history of the patient, a chest examination, and to check for reversible airflow obstruction using spirometry with a short acting bronchodilator[208]. The downside to the aforementioned methods is the inability to detect inflammation in the airway, which is one of the key features of asthma. Bronchoscopy is a more invasive method to diagnose asthma, where physicians may perform bronchial biopsies to visualize airway wall structures and/or perform bronchoalveolar lavage (BAL) to obtain respiratory cells and secretions which may provide complimentary information[209] in terms of better studying inflammation.

There are numerous drugs available on the market to treat asthma and are classified into long term control medications or quick acting relief medications[208]. These treatments have come about from more fundamental understanding of disease, from bronchodilators for quick relief to anti-inflammatory drugs for long term management of disease [178, 204]. Nevertheless, unlike COPD, most often asthma can be managed with the appropriate drug treatments.

5.2.2.3 Airway Wall Remodeling in Asthma

Major changes in the airway wall in asthma include fragility of the epithelium, a thickened reticular basement membrane, increased vasculature, increased smooth muscle content in large airways (hypertrophy), and increase in glands[197].

Hypertrophy of smooth muscle in large airways, represents a major difference in airway wall remodeling in asthma in comparison to COPD. Another increase in airway smooth muscle that occurs in fatal asthma is hyperplasia in large and small airways[210]

and the percent of bronchial wall composing of smooth muscle is almost doubled to approximately 12% compared to 5% in a normal airway [211].

5.3 *OCT and Pulmonary Imaging*

Equipped with knowledge and understanding of obstructive lung diseases such as COPD and asthma, we can now explore the role that OCT plays in pulmonary imaging. Clearly, accessing small airways less than 2 mm *in vivo* has been a difficult task. Additionally, use of spirometry as a diagnostic tool is not helpful until disease progresses into larger airways in COPD and is not a good indicator of inflammatory responses in asthma. Nevertheless, there are many morphological changes that occur in the small airways which may be of diagnostic value. OCT is able to perform depth resolved imaging and obtain cross-sectional information which may be similar to what is presented in histological findings. Thus endoscopic OCT can be helpful to aid in diagnosis and early detection. Currently pulmonary imaging in OCT has focused imaging bronchial lesions, anatomical measurements of the airways, visualization of airway smooth muscle directly or through birefringence and visualization of alveoli.

5.3.1 Visualizing Bronchial Lesions

OCT is frequently used for cancer imaging due to the ability to visualize tissue microstructure below the surface, making it an excellent complementary imaging modality to standard endoscopic imaging. Endoscopic OCT at 1300 nm has been used to show that normal airway wall structures have a layered appearance in contrast to tumors which appear as unevenly distributed increase in backscattered light [212-214]. OCT was further studied to show that imaging can differentiate dysplasia and carcinoma *in situ*

from lower grade lesions [215], while another study described the ability to visualize differences between squamous cell carcinoma, adenocarcinoma, salivary gland and mucinous adenocarcinomas[214].

5.3.2 Anatomical OCT

An active area of interest in OCT is to perform anatomical OCT where the dimensions of the airways may be measured endoscopically and *in vivo* for airway profiling to study obstructive sleep apnea [216, 217], visualization of changes during respiration[218-220], surgical intervention and potential subsequent stent or valve placement[221], or visualization of airway wall narrowing due to electrical [222] or chemical stimulation[223].

5.3.3 Visualizing Alveoli

Since alveolar walls can be destroyed in obstructive emphysema, visualizing normal and abnormal alveoli could be of clinical relevance. Since alveoli are past the terminal bronchioles, endoscopic probes have to be very small to reach these spaces, making it difficult to visualize with standard bronchoscopy. Early on, studies were performed with *ex vivo* lung specimens using benchtop systems[224, 225] however this was slowly transitioned to endoscopic probes.

In one study, two types of needle probes were developed for static and dynamic imaging of alveoli and lung structures in *ex vivo* lungs of large and small animals. Imaging was performed with an 800 nm SD-OCT system and the probes were inserted by puncturing the inflated lung from the pleura, images showed the ability to visualize alveoli, bronchioles and blood vessels [226].

5.3.4 Visualizing Airway Wall and Wall Structure

Earlier it was discussed that in both COPD and asthma, the airway wall undergoes remodeling. One of the areas of interest has been attempting to visualize the role of airway smooth muscle in these diseases, however, due to the small percentage (and small size and thickness) of smooth muscle in small airways it has been difficult to achieve with standard 1300 nm systems.

Nevertheless, preliminary work in visualizing airway wall structures with comparison to histopathology occurred with 1300 nm benchtop OCT systems[227, 228], paving the way for further research to be performed. With the advent of endoscopic OCT systems, it was highlighted as an important tool for measurement of airway wall dimensions when it was compared against widely used computed tomography (CT) measurements and found to be more sensitive the changes in the small airways of patients with obstructed airflow[229].

In another study, endoscopic OCT was performed on *ex vivo* porcine airways which were then fixed for histology and compared against the cross-sectional OCT images. In this study, the airway wall components and areas were measured and compared between OCT and histology to show that OCT images are able to accurately depict airway wall substructure relative to the airway wall area [230]. Measurement of the airway wall area is an important feature when studying COPD or asthma, where there may be airway wall thickening compared to a normal healthy lung. Although this study was rigorous, OCT imaging was performed in *ex vivo* tissue specimens, not accounting

for the true physiological environment *in vivo* because the small tissue sample of airway was not imaged in an inflated state.

The area of interest in this dissertation, is not only visualizing the small airway wall, and specifically airway smooth muscle since it is hypothesized to have a key role in airway wall remodeling and narrowing in COPD and asthma. Since airway smooth muscle is a small percentage of normal healthy airway wall (≤15 % in adults[231]) it has been difficult to visualize it using 1300 nm OCT systems where the resolution is not sufficient to visualize the small thickness of airway smooth muscle. Recently, two approaches to visualize airway smooth muscle have been demonstrated. One method was to employ polarization sensitive OCT and take advantage of the birefringent properties of airway smooth muscle (ASM) to identify it[232] while the other method employed high resolution endoscopic OCT with 800 nm SD-OCT to directly visualize the airway smooth muscle[233].

5.4 *Methods*

	Endoscope	**O.D.**	**δx**	**W.D.**	**B.R.**	**Loss**
	E^1	2.1 mm	5.8 μm	200 μm	-81 dB	< -3.8 dB
	E^2	1.78 mm	6.7 μm	215 μm	-81 dB	< -2.8 dB
	E^3	1.78 mm	6.5 μm	260 μm	-81 dB	< -2.5 dB

	E^4	1.78 mm	5.9 µm	235 µm	-78 dB	< -3.09 dB
	E^5	1.78 mm	5.8 µm	265 µm	-81 dB	< -2.6 dB

Table 5-1: List of endoscopes used.

O.D.: outer diameter including protective plastic sheath, δx: lateral resolution, W.D.: working distance measured from the plastic sheath of the probe to the focal plane, B.R.: backreflection of the catheter, loss is the double-pass signal attenuation, and FOV blockage: is the field of view blockage due to struts and wires of the distal end enclosure measured as a percentage of the circumference. E^1: Design had a 4 strut enclosure, employed an aluminum coated prism reflector, and standard motor. E^2, E^3 and E^4: Design had a 3 strut enclosure, employed a gold coated rod reflector and customized motor. E^5: Design had a 4 strut enclosure with wire gap (described in chapter 3), employed a gold coated rod reflector and customized motor.

5.4.1 Endoscopic Imaging System

The endoscopic spectral domain OCT (SD-OCT) system is as shown in Figure 3.5 A. The light source employed was the home built Ti:Sapphire laser with a central wavelength of 830 nm and a spectral bandwidth of ~ 150 nm, achieving an axial resolution of 2.6 µm (in air) endoscopically.

The OCT catheters employed over the course of this project are similar to the one pictured in Figure 3.3 D and is catheter E^5 in Table 5-1. The catheters E^1, E^2, E^3, and E^4 are previous versions of the distal scanning OCT catheter. All versions of the OCT

catheter employ the same optical design elements, with a diffractive lens, glass rod and GRIN lens. The intended optical design maintained a short working distance of less than 300 μm, with the intent to determine the most optimal working distance for small airway imaging. The working distance is defined as the distance from the plastic sheath to the focal plane of the catheter.

The main difference between the catheters in Table 5-1 is the mechanical design. $E^1$was designed prior to the customized Namiki motor[6] and customized rod reflectors, thus the enclosure was fabricated with 4 struts and an off-the-shelf aluminum coated prism reflector. The catheter E^2, $E^3$and E^4 were designed for the customized motor described in chapter 3, and a new enclosure which only had 3 struts and employed customized gold coated rod reflectors, which enabled the loss to be reduced from the original design. Finally, E^5 was designed as described in chapter 3 and represents the final distal scanning endoscope design.

5.4.2 Experimental Protocol

OCT imaging was performed on sheep small airway *in vivo* under a protocol approved by the Animal Use and Care Committee (ACUC) at Johns Hopkins University. The animal was anesthetized and ventilated throughout the duration of imaging. After intubation a bronchoscope was inserted and the OCT catheter was passed through the accessory port

[6] The standard Namiki motor had 4 backward facing wires that were heat-shrinked together in a bundle that was approximately 500μm in diameter. Each wire was individually insulated with an outer diameter of 120 μm. The motor also did not have a customized pedestal for mounting a reflector.

and lodged into a small airway approximately 70 cm into the lungs (4 cm beyond the end of the bronchoscope).

5.4.3 Imaging Protocol

Upon insertion of the catheter, radial scanning with the micromotor and pull-back scanning with a motorized translation stage was performed. Table 5-2 lists the

Sheep #	Date	Catheter Used	Frame Rate	Pitch
1	11/11/2015	E^2	20 fps	20 µm
2	01/12/2016	N.A.	--	--
3	02/01/2016	E^3	20 fps	20 µm
4	03/21/2016	E^4	20 fps	20 µm
5	05/02/2016	E^4	20 fps	20 µm
6	06/01/2016	E^5	20 fps	20 µm
7	07/06/2016	E^5	20/50 fps	20 µm
8	08/01/2016	E^5	50 fps	20 µm
9	09/07/2016	E^5	50 fps	10 µm

Table 5-2: List of sheep experiments.

experiments that have been performed and the catheter variation that was used for each experiment, along with the imaging frame rate and pitch between subsequent frames.

Figure 5.1 A shows a representative cross-sectional image of a small airway acquired using catheter E^3 where some structures of the airway wall such as epithelium, lamina propria, and cartilage are depicted. There are three shadows on the images caused by the ultrafine metal struts of the self-aligning enclosure and the micromotor drive wires. Figure 5.1 B shows an example 3D volumetric rendering of the entire pull-back scan.

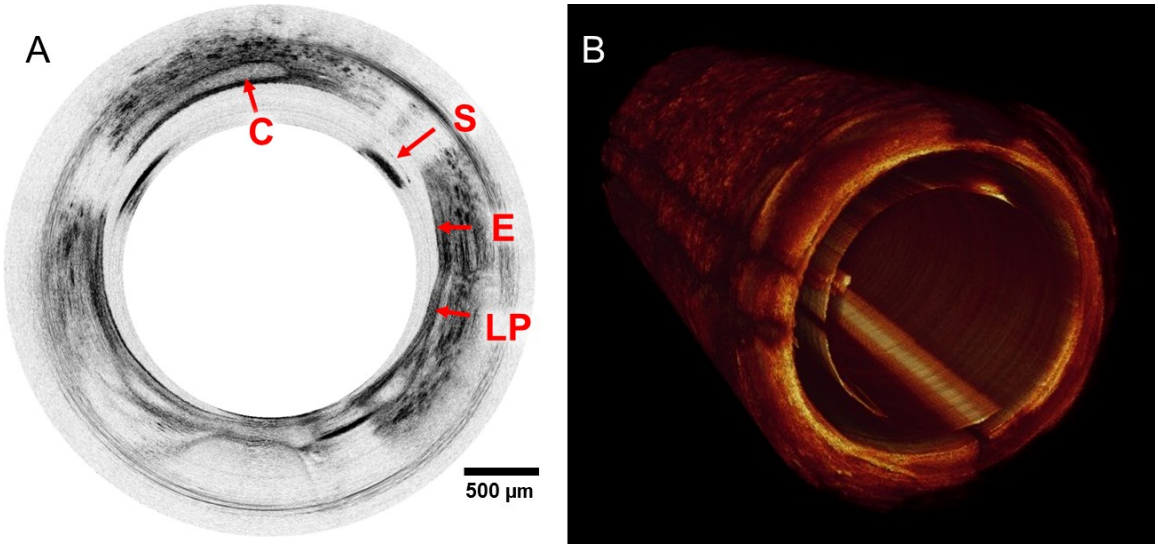

Figure 5.1: Cross-sectional and volumetric images of *in vivo* sheep airway from sheep #3.

(A) Representative cross-sectional frame and (B) snapshots of 3D visualizations of volumetric pull back scan acquired from the sheep airways *in vivo.* C: cartilage, S: ultrafine strut of distal enclosure, E: epithelium, and LP: lamina propria.

5.4.4 Determination of Optimal Working Distance Catheter

Table 5-1 shows the iterations of catheters that have been fabricated throughout the course of imaging experiments. One of the changes between catheters has been the working distance or distance from the protective plastic sheath to the focal plane of the probe. In doing so, we were able to pinpoint the best range of working distances optimal for imaging the small airways.

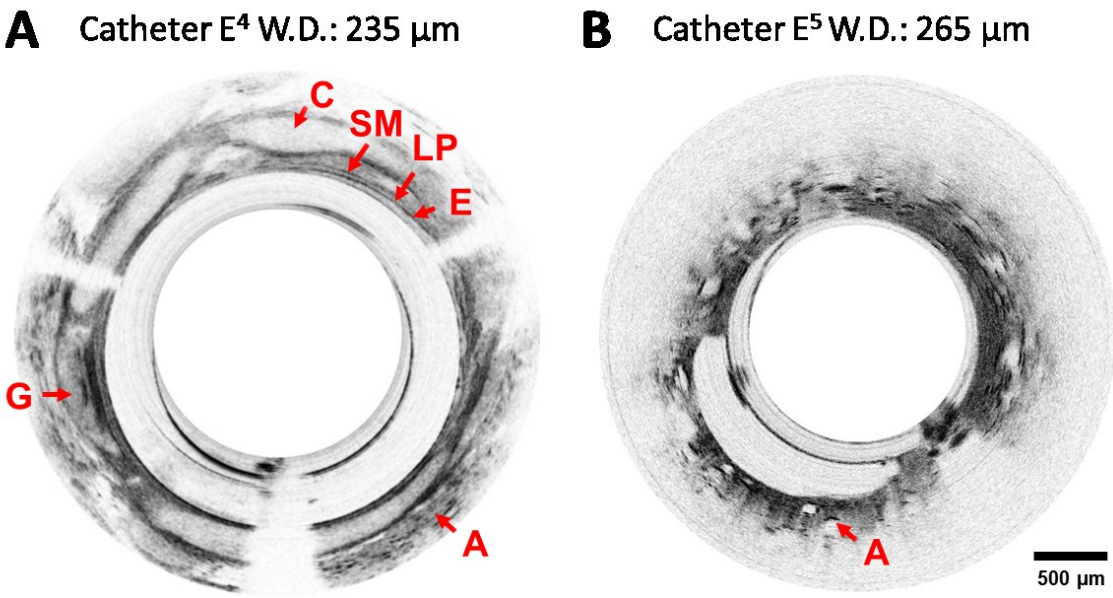

Figure 5.2: Representative cross-sectional frames from catheters with varied working distances.

(A) Representative cross-sectional image acquired from sheep #4 with catheter E^4. (B) Representative image acquired from sheep #7 using catheter E^5. E: epithelium, LP: lamina propria, C: cartilage, SM: smooth muscle, A: alveoli, and G: glands.

Below in Figure 5.2 A and B show cross-sectional images acquired from catheters E^4 and E^5. Through these two catheters we have been able to determine that airway wall

structures very close to the airway wall surface are best visualized with working distances of 235 μm or shorter such that the light is not significantly dispersed by the time it reaches the structure. Several wall structures are able to be seen clearly by catheter E^4 in Figure 5.2 A. Alternatively, to visualize airways which are larger in diameter than the catheter a longer working distance is preferable. Thus, catheter E^5 in Figure 5.2 B shows structures farther away sharper than structures near to the catheter sheath.

Both catheter working distances can be of use in airway imaging depending on the structures of interest. For example, although the airway wall may not be clearly visualized by catheter E^5, the faraway alveoli structures are clearly seen. This catheter can possibly be of use to study breakdown of alveolar walls in obstructive emphysema. In this dissertation, we are primarily interested in airway wall components, thus working distances shorter than 235 μm are optimal.

5.4.5 Direct Visualization of Airway Smooth Muscle

One of the goals of ultrahigh resolution endoscopic imaging was to be able to directly visualize airway smooth muscle due to the fact that it has not been able to be visualized clearly with previous OCT systems, as mentioned earlier.

In order to demonstrate the capability of ultrahigh resolution endoscopic OCT to directly visualize the airway smooth muscle it was necessary to compare with respect to corresponding histology acquired immediately after *in vivo* imaging. Figure 5.3 A is the same cross-sectional image shown in Figure 5.2 A and the corresponding histology slide from the same airway acquired after sacrificing the animal is shown in Figure 5.2 C. Several structures are labeled in both images, such as the epithelium, lamina propria,

cartilage, airway smooth muscle, alveoli and glands. In order to further appreciate this, Figures 5.3 B and D show the zoomed-in images of regions in the red dashed line boxes in Figures 5.3 A and C. Through these images it is clear that smooth muscle is on the order of 10's of μm and can be visualized with high resolution endoscopic OCT.

In the image shown in Figure 5.3 A the measured thickness of the smooth muscle at the location of the arrow is ~8.6 μm measured as ~20 pixels. The imaging depth was calibrated to 1.23 mm and corrected by assuming a refractive index of 1.4. A similar measurement in of the smooth muscle at the location of the arrow on the histology slide was ~5.8 μm. It has been noted that lung fixation techniques lead to shrinkage of the tissue and by using a correction factor for sheep of 1.59[234] from the histologic section to the unfixed air filled lung the measurement of the smooth muscle may be ~9.2 μm. Assuming the histologic measurement to be correct the percentage error in the measurement is approximately 6.5%.

The structures measured are on the same order of the axial resolution of standard 1300 nm endoscopic OCT systems. The manual measurement of airway smooth muscle in shown in Figure 5.3 aids to illustrate the significant advantage that ultrahigh resolution endoscopic OCT systems demonstrate for imaging of the small airways.

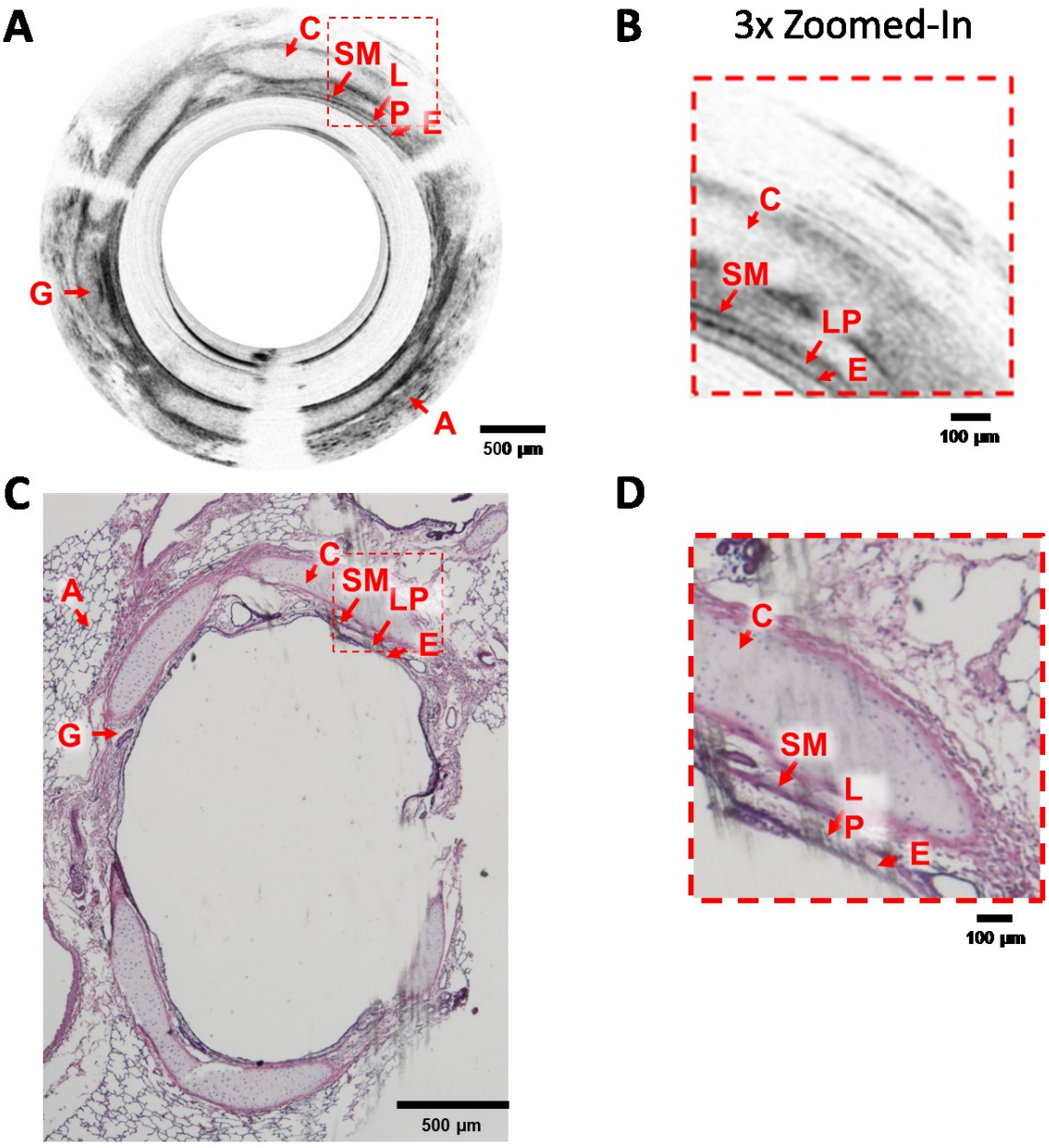

Figure 5.3: Cross-sectional image of sheep airways *in vivo* with corresponding histology.

(A) Representative cross-sectional image from sheep #4 and corresponding histology (C). (B) and (D) are the 3x zoomed-in regions shown in red dashed-line boxes in (A) and (C). E: epithelium, LP: lamina propria, C: cartilage, SM:

smooth muscle, A: alveoli, and G: glands.

5.4.6 Towards Volume Correlation of OCT and Histology

In addition to correlation of OCT cross-sectional frames with histology slides, another important aspect to further correlate OCT and histology is through volume correlation of several OCT images with histology slides from the same airway. This type of volume correlation would enable true confirmation of OCT image correlation with corresponding histological slides.

5.4.6.1 Volume Registration of OCT Scans Before and After Marking with India ink

In order to perform volume registration of airway segments, an airway segment was imaged before and after marking with India ink, to confirm the location of the ink mark . The airway segment was marked using an endoscopic side-marking needle that was expanded to match the inner diameter of the airway of interest. After imaging OCT imaging was completed, the lungs were fixed and the airway segment was dissected through manual airway mapping. The airway segment was cut into several blocks from which several histology slides were cut.

Figure 5.4 A and B show the *en face* projection view of the pull-back scan before and after marking with India ink, respectively. A few airway segment features demonstrate the similarities between the images before and after marking with ink. There are two branch points visible in both images as well as 3 signal void regions from the metal struts.

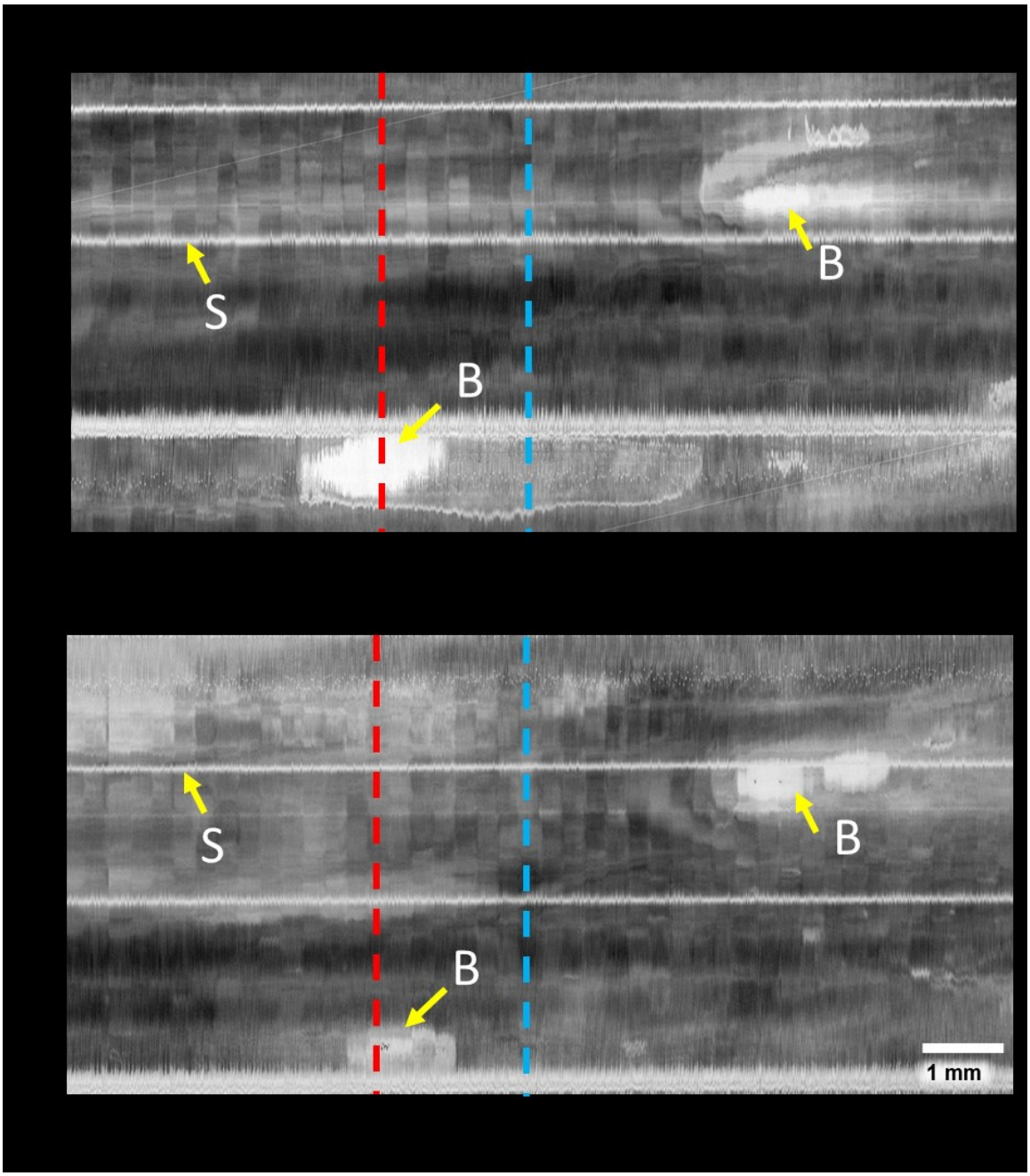

Figure 5.4 *En face* projection view before and after India ink.

En face projection views of pull-back scan before (A) and after (B) injection of India ink. S: metal strut of catheter enclosure, B: airway branch points.

In order to further demonstrate that these two data sets are correlated, Figure 5.5 has cross-sectional images from the locations of red and blue dashed lines in Figure 5.4 A and B.

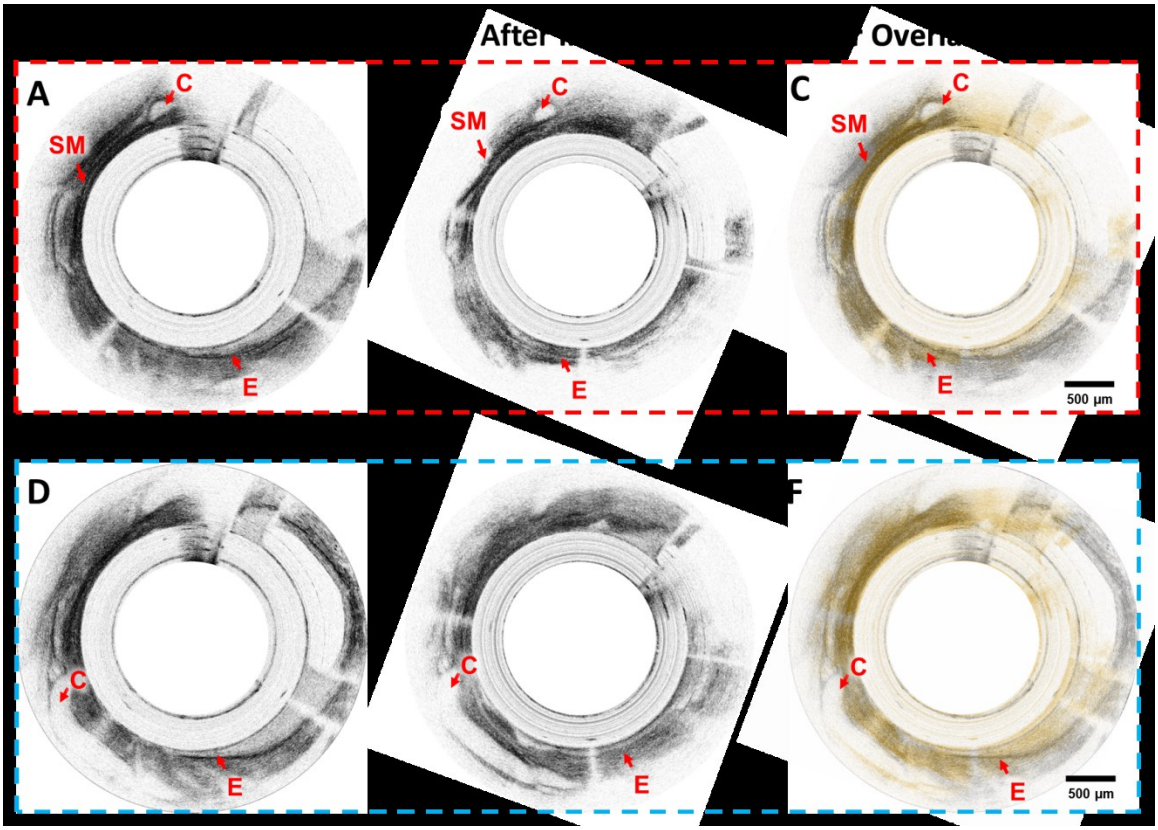

Figure 5.5: Representative cross-sectional images before and after marking with India ink.

(A) and (B) cross-sectional frames from the distal part of the airway where the segment has been inked. (D) and (E) are representative cross-sectional frames from regions prior to the ink spot. (C) and (F) show the cross-sectional images after inking overlaid in gold on the cross-sectional images prior to inking.

E: epithelium C: cartilage and SM: smooth muscle.

Figures 5.5 A and B are the cross-sectional images from the red dashed lines in Figure 5.4 A and B, respectively. These images are from the more distal portion of the airway segment and signal attenuation is higher in Figure 5.5 B due to the India ink marking. Similarly Figures 5.5 D and E are from the location of the blue dashed line in Figure 5.4 A and B, respectively. These images are located proximally and are prior to the area that was marked with India ink, thus Figure 5.5 E does not show significant signal attenuation. Both sets of cross-sectional images bear similarity in the location and size of airway wall components such as cartilage and smooth muscle.

In order to appreciate the correlation further, in Figure 5.5 C the cross-sectional image after inking (Figure 5.5 B) is overlaid on the image in gold color prior to inking (Figure 5.5 A) which is still in grayscale. The most prominent feature, the cartilage matches in both images, after which the gold overlaid image shows significant and quick signal decay in comparison to the pre-inked image in grayscale. Figure 5.5 F shows the same overlay in gold of the image in Figure 5.5 E on the pre-inked image in grayscale in Figure 5.5 D. In this cross-sectional image, the two regions of cartilage and region of smooth muscle are seen to be overlapped.

There are some differences in the cross-sectional images caused by some physiological and experimental phenomena. Firstly, the pitch between two frames is 10 μm, so the image match between the two datasets can potentially be from a position with a difference of 5 μm. The lateral resolution of E^5 is ~5.8 μm meaning that the lateral position is not sampled per the Nyquist sampling requirement. Reduction of lateral sampling occurs under the assumption that physiological wall structures will not change

significantly within the period of 10 μm, enabling us to match adequately. Secondly, due to physiological motion, the exact oblique cross-sectional angle may not be identical after removal of the catheter and reinsertion. Thirdly, due to insertion and retraction of the catheter and marking needle, excessive irritation causes production of mucus within the airways. This can be seen when looking at Figure 5.5 E where there is a naturally 'fuzzy' look to the image due to distortion caused by excessive mucus in the airways, preventing the airway wall from being clearly visualized. Additionally, this is the reason why the branch points appear smaller in Figure 5.4 B in comparison to the pre-inked scan in Figure 5.4 A.

5.4.7 Future Correlation Goals

The section above showed the ability to insert the catheter to the same airway and image it before and after marking the segment with India ink. One of the goals of this experiment is also to provide correlation of the airway segment with histology slides. *In vivo* correlation of OCT images with histology is one of the most challenging aspects of this project. In addition to the difficulties of imaging the same airway segment after retraction and re-insertion of the catheter, dissecting the airway after the lungs have been fixed poses an equally challenging problem. Although airway mapping is accurate enough to reinsert the catheter, searching for the same airway, after fixation, can be difficult. Even with India ink marks, it can be unclear as to which airway segment is of interest due to the fact that the need could puncture deeper into the wall spreading ink into a neighboring airway segment. For these reasons, correlating the airway segment images to a histology stack of the segment can be challenging.

This is one of the goals currently being investigated. The solution may be to try other marking methods or to find new ways of reaching the same airway segment after fixation of the entire lung. Another marking technique such as laser marking has been previously tested to mark the epithelial lining of the esophagus after imaging in order to guide acquisition of biopsy samples under standard endoscopy[235]. Some advantages to this approach are that the adjacent airway would not be marked, and the effect of marking would be minimal on the OCT image in comparison to India ink. When India ink spreads, there is significant attenuation throughout a region of the airway segment making it difficult to match before and after images. Unfortunately, one of the downsides to this approach is that it may be difficult to visualize by eye without slicing the airway segment open, not aiding in the efforts to dissect the correct airway segment.

Yet another more manual approach would be to leave a guide-wire, colored tubing in the airway segment after imaging. This approach may be used in conjunction with a marking mechanism. Ideally, after reinsertion of the image catheter, and confirmation of the marked area, the catheter could be retracted whilst leaving the plastic tubing in the airway segment. Aside from longitudinal displacement due to physiological motion, the plastic tubing may be able to remain in the same position through the fixation process, aiding manual dissection of the correct segment.

5.5 *Conclusions*

In this chapter, it has been shown that ultrahigh resolution endoscopic OCT can be performed in *in vivo* sheep airways at a speed of up to 50 frames-per-second (limited based on the A-scan rate of the SD-OCT engine). The ability to visualize smooth muscle

and correlate it with corresponding histology has been shown. Finally, the ability to image the same airway segment before and after ink marking shows the ability to perform volumetric airway segment registration.

In the following chapters, the ability of this endoscopic OCT system to perform longitudinal imaging in a disease model will be explored. The final two chapters will explore other projects that have been completed during the course of studies.

Chapter 6 Colorectal Cancer Imaging in Mice

6.1 *Introduction*

This chapter will focus on endoscopic imaging results in a longitudinal colorectal cancer model in mice. The first part of this chapter will focus on the significance of colorectal cancer imaging in small animals such as mice and the role of OCT in the context of small animal imaging studies. The rest of the chapter will focus on the imaging studies performed with our high speed, ultrahigh resolution endoscopic OCT system, specifically *in vivo* imaging of colon polyp formations in four mice over an eight week period. The goals were to be able to perform longitudinal experiments in a mouse model to detect morphological changes during the course of disease.

6.2 *Background*

Colorectal Cancer is one of the leading causes of cancer related deaths. The usual progression of disease involves an adenomatous polyp in the colon or rectum that will essentially increase in size and become malignant. The key to testing is to be able to identify polyps at a benign stage and monitor it prior to becoming malignant. Imaging based tests can help to visualize any abnormalities in the colon and rectum that would need to be monitored over time.

6.2.1 Colorectal Cancer

Colorectal cancer (CRC) is cancer affecting the colon and rectum. There are numerous risk factors for CRC including diet, environmental, and genetic factors. In comparison to

genetic factors it has been relatively difficult to define diet and environmental factors as risk factors for CRC, nevertheless some new models and hypotheses are gaining momentum to explain other ways that CRC can be induced.

In the genetic model for cancer, certain genetic defects are accumulated causing tumor/adenoma growth and subsequent spread of cancer[236]. Genetic defects can usually be categorized defects leading to new oncogenes or increasing the function of existing oncogenes or decreasing the function of tumor suppressor genes. Several gene defects leading to inherited and sporadic CRC have been identified, perhaps the most well-known defect being in the adenomatous polyposis coli (APC) gene which is a tumor suppressing gene. Mutations in this gene are linked to familial adenomatous polyposis (FAP) which is a hereditary form of CRC, Gardner syndrome, Turcot's syndrome, attenuated adenomatous polyposis and in a majority of sporadic CRCs (approximately 70-80%) [237].

Another model for CRC is a bacterial driver-passenger model which suggests that CRC can be initiated due to (driver) bacteria within the gut which are replaced with (passenger) bacteria that can encourage or hinder tumor growth[238]. The concept of driver bacteria is related to the 'alpha-bug' hypothesis which suggests that certain bacteria such as enterotoxigenic *Bacteriodes fragilis* (ETBF) are oncogene promoting and can make changes in the mucosal immune system that promote CRC. The crux of the alpha-bug hypothesis is that there is a triangular relationship between the colon microbiome (at the top) driving changes in the immune system response and subsequently the colonic epithelial cells and changes or genetic mutations in the colonic

epithelial cells are where CRCs originate[239]. Regardless of the method by which CRC originates, it is a disease with a high rate of incidence that is not easy to detect early in the disease process.

6.2.2 Prevalence and Screening of Colorectal Cancer

Colorectal Cancer has one of the highest incident rates, ranking among the top 5 cancers from 2007-2011 [240] in the United States. Early detection is known to increase the 5 year survival rate from 65% to 90%, however only 40% of cases are diagnosed early enough [241]. Screening tests can be divided into two categories fecal sample testing and image based testing. Image based testing includes double-contrast barium enema, colonoscopy, flexible sigmoidoscopy and computed tomography colonoscopy. Imaging based tests are typically done at 5 or 10 year intervals compared to fecal sample based tests which are should be done annually [242]. There is no definitive best practice for colorectal screening, guidelines suggest that high risk adults be screened for colorectal cancer with optical colonoscopy, while average risk adults can be screened with either fecal testing, flexible sigmoidoscopy or optical colonoscopy[243].

Traditional colonoscopy performed for screening is only able to visualize and detect adenomatous polyps that are slightly elevated from the surface. Colonoscopy is particularly ineffective in early stages such as field carcinogenesis where there is no detectable polyp or histopathological signature, however some molecular or structural changes have begun [244].

In addition to structural imaging techniques fluorescence based techniques such as laser induced fluorescence spectroscopy [245, 246] and auto-fluorescence endoscopy

[247, 248] have already been applied to the study of colorectal cancer in human tissues to differentiate dysplasia from malignant polyps.

OCT is a high resolution, real-time, non-invasive imaging modality that has been well established for colon imaging. Initially, feasibility of employing OCT as an imaging modality for colon imaging was tested using benchtop OCT systems which investigated *ex vivo* human colon tissue. Studies have shown that OCT was able to visualize colonic mucosa as well as detect changes in the mucosa and submucosa in early stage cancer [249, 250]. With technological advancement, endoscopes were integrated into 1300 nm based OCT systems enabling *in vivo* endoscopic imaging of human colon tissues [68, 70].

6.2.3 OCT Imaging of Colorectal Cancer in Mice

There has been a push for the development of murine colorectal cancer models to exhibit the same behaviors as human colorectal cancer model for study of biomarkers, therapeutics and imaging agents that can be used for more effective screening and diagnosis [251-253]. Simulating colonoscopy screening processes in murine models remain challenging due to the small scale of the colon in mice. There have only been a limited number of studies showing that colonoscopy can be performed in live mice [253, 254], however many other technologies such as fluorescence imaging [255-257] and OCT imaging technologies [76, 77] integrated with fluorescence [258, 259] have been implemented with more success.

Even with recent advances in technology it remains challenging to perform these procedures in murine colorectal cancer models as a way to study the efficacy of therapeutic and diagnostic imaging agents as well as studying screening protocols. Thus

there is a need to develop image based technologies capable of detecting abnormalities in colonic mucosa in murine models.

The challenges in implementing OCT for imaging in murine models are in miniaturizing endoscope probe design while simultaneously increasing axial resolution to be able to visualize aberrant crypts in colonic mucosa. Such high resolution OCT has only been able to be achieved by moving OCT to central wavelengths around 800 nm. OCT at this wavelength has been demonstrated[76, 77], however only recently, with technological innovations, enabled 3D volumetric endoscopic imaging for investigation of the entire luminal organ [78].

In this chapter we will focus on using the ultrahigh resolution, high speed endoscopic OCT system described in earlier chapters to monitoring morphological changes longitudinally. The next section will describe the animal model used to simulate colorectal cancer in mice.

6.2.4 ETBF Induced Colon Cancer Model in APC^{Min} mice

As discussed earlier, CRC is generally explained through accumulated genetic mutations and more recently a bacterial driver-passenger model and the alpha-bug hypothesis. In the hypothesis, bacteria could result in immune system changes which were responsible for changes in the colonic epithelial cells where genetic mutations would lead to CRC.

Bacteriodes fragilis (B. fragilis) is a bacterium found in the normal flora of the human colon and is generally commensal unless it is moved into the bloodstream or surrounding tissue where it can cause infections. Enterotoxigenic *Bacteriodes fragilis*

(ETBF) is a subset of B. fragilis is known to secrete a proinflammatory toxin (B. fragilis toxin) and it has been linked to diarrheal diseases, colitis, and IBD and CRC [260, 261].

As discussed above, mutations in the APC gene has been linked downregulation of tumor suppression and has been linked to a majority of hereditary and sporadic CRCs. Mice share many similarities with humans on physiological scale and this extends to tumor expression of mice due to APC gene mutations. In the subset of APC models, the multiple intestinal neoplasia (Min) mouse has a point mutation in the APC gene and is frequently the model used to study the tumor suppressing capabilities of the APC gene[262].

ETBF induced colon cancer in APC^{Min} mice provides a model for human commensal induced CRC that can be used to study morphological changes occurring in the colon leading up to cancer. APC^{Min} mice will develop intestinal tumors over the course of 2-3 months that will gradually develop into CRC however when treated with ETBF, the mice experience colitis that results in a rapid growth of distal colonic tumors [263].

In this chapter, we use this model to study accompanying morphological changes within a total of 8 weeks after inoculation with ETBF. This would be the first time that OCT has been used to study the longitudinal changes in a bacterial model for CRC.

6.3 *Materials*

6.3.1 Endoscopic Imaging System

The endoscopic spectral domain OCT (SD-OCT) system is as shown in Figure 3.5 A. The light source employed was the home built Ti:Sapphire laser with a central wavelength of 830 nm and a spectral bandwidth of ~ 150 nm, achieving an axial resolution of 2.6 μm (in air) endoscopically. The OCT catheters employed over the course of this project are similar to the one pictured in Figure 3.3 D (chapter 3) and is catheter E^5 in Table 5-1.

Specifically, for these experiments, the protective plastic sheath was marked every centimeter from the reflector portion of the catheter for a distance 4 centimeters away. This was done in order to ensure that the catheter did not puncture the mouse colon during imaging.

6.3.2 Animal Protocol

All imaging was performed under a protocol approved by the animal use and care committee at Johns Hopkins University. For these experiments, APC^{Min} mice were infected with enterotoxigenic bacteriodes fragilis (ETBF).

The baseline image represents imaging performed on the animals before being infected with ETBF. After the bacteria have colonized the colon, the animals will experience severe colitis and shedding of the intestinal epithelial lining for approximately 2 weeks, during which time imaging is not performed. Once the animals recover from colitis, physiological processes leading up to tumor growth can occur. Thus the first imaging time point after baseline is set to approximately 2 or more weeks until the animals have recovered.

6.3.3 Imaging Protocol

During each imaging session, the animals were anesthetized with mouse mix (100mg/kg Ketamine and 10 mg/kg Xylazine) which allowed for a ~45 minute imaging period. After the mice were anesthetized, the catheter was directly inserted into the colon from the rectum. The catheter was inserted a total length of 4 centimeters (as marked by the plastic sheath) or until physical resistance was felt. This was done to ensure that the colon was not puncture during the course of experiments due to polyp growth or stool impeding the path of the catheter.

OCT imaging was performed at 50 frames-per-second with each frame composed of 1397 A-lines and pull-back was performed with a 20 μm pitch between subsequent image frames. This limited the overall imaging time to less than 2 minutes per animal. We found that these parameters were ideal for imaging the mouse colon in a quick fashion and minimized trauma experienced by the mouse enabling imaging weekly without sacrificing the mouse.

Date	Image Set	Mouse
2015-12-01	Baseline	F70
2015-12-29	Day 8	F70
2016-01-06	Day 16	F70
2016-01-14	Day 24	F70

Table 6-1: Log of longitudinal preliminary mouse experiments.

6.3.4 Preliminary Experiments: Visualizing Morphological Changes

This section reports the results obtained from preliminary testing in the aforementioned mouse model. The goal was to be able to consistently obtain images from the same animal with minimal trauma and visualize morphological changes during the course of the disease. For these first set of experiments, imaging was performed using catheter E^2 and imaging was performed at 20 frames-per-second with 3470 A-line-per-frame. The results of these preliminary experiments are summarized by Figures 6.1 and 6.2.

Figure 6.1 A and 6.2 A are the *en face* projection view of the mouse colon from Mouse F70 at baseline and 24 days after inoculation of ETBF in the colon. A few major features are noted from the *en face* projection view images, 1) There are three signal void regions corresponding to the endoscope enclosure and wires and 2) in Figure 6.2A B there is a clear change in the averaged projection view showing a more distinctly heterogeneous structure in the colon due to polyp formation.

In order to look more closely at these changes we can look at the corresponding cross-sectional images from locations throughout the pull-back scan as shown from each volume in 6.1 B-C and 6.2 B-C.

The cross-sectional images in Figure 6.1 B-C are from the baseline volume and perhaps the most notable feature is that in all cross-sectional images the submucosa and muscularis mucosa are able to be seen past the colonic mucosa. This is especially notable in comparison to the cross-sectional images in Figure 6.2 B and C where the colonic mucosa is thicker with significant signal attenuation making it difficult to visualize the submucosa and muscularis mucosa.

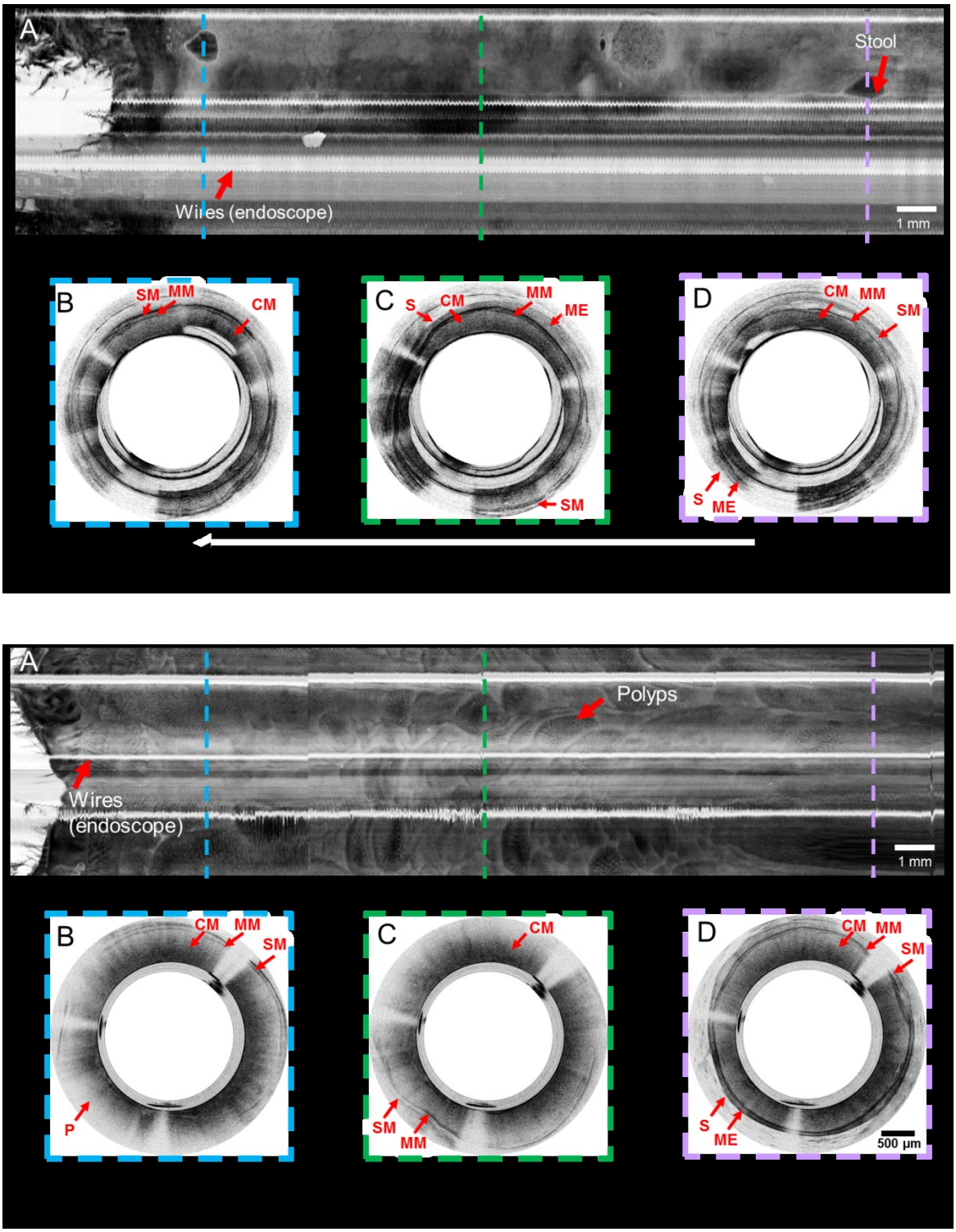

Figure 6.1: *En face* projection view and corresponding cross-sectional images from baseline and day 24 scan of mouse F70.

(A) *En face* depth averaged projection view of volumetric pull-back scan showing signal void regions from wires and some hyperintense signal region due to stool. (B) Cross-sectional image acquired from the location of the light blue dashed line, (C) green dashed line and (D) purple dashed line. (A) *En face* depth averaged projection view of volumetric pull-back scan showing signal void regions from wires and some rounded structures that are polyps. (B) Cross-sectional image acquired from the location of the light blue dashed line, (C) green dashed line and (D) purple dashed line. Labeled structures include: CM: colonic mucosa, MM: muscularis mucosa, SM: submucosa, ME: muscularis externa, S: serosa and P: polyp.

6.3.5 Additional In Vivo Studies: Over 8 week period

After performing preliminary imaging experiments to confirm that morphological changes could be monitored *in vivo* during as tumor growth progresses, another set of experiments were organized as shown in the log in Table 6-2. The experiments used 3 female and 3 male animals housed separately, however during the course of experiments 2 female mice, F1 and F2, died and histology was unable to be performed in a timely manner. F2 died during bacterial colonization so no subsequent imaging was able to be performed. F1 died in between days 37 and 44. It is suspected that the mouse may have died due to perforation of the colon; however no autopsy was done to investigate the cause of death of the animal.

Date	Image Set	Mouse
2016-07-15	Baseline	F1, F2, F3, M1, M2, M3
2016-08-05	Day 19	F1, F3, M1, M2, M3
2016-08-11	Day 25	F1, F3, M1, M2, M3
2016-08-23	Day 37	F1, F3, M1, M2, M3
2016-08-30	Day 44	F3, M1, M2, M3
2016-09-09	Day 54	F3, M1, M2, M3
2016-09-13	Day 58	F3, M1, M2, M3

Table 6-2: Log of longitudinal mouse experiments.

Animals F1 and F2 did not survive the course of experiments until day 58.

Figure 6.2 shows the *en face* depth averaged projection view of a volumetric scan from each time point during imaging of mouse M2. Data from M2 is representative of the physiological changes seen across all animals, i.e. from normal mucosa at baseline, inflammation after bacterial colonization, and finally subsiding inflammation and tumor growth.

One of the observed differences among mice was the overall progression of tumor growth characterized by the number and density of tumors. Volumetric scans from M1 showed numerous smaller tumors clustered together throughout tumor progression.

Whereas tumor growth in F3, M2, and M3, consistently showed fewer, larger tumors more spread out over the distal portion of the colon.

Since the overall morphological changes (i.e., tumor growth) progressed the same way across all animals, the rest of this chapter uses data from M2 to further discuss the morphological changes that were visualized from baseline until day 58. Figure 6.2 A shows the baseline image and figure 6.2 G shows the last time point before the animal was sacrificed and the colon was removed for histology.

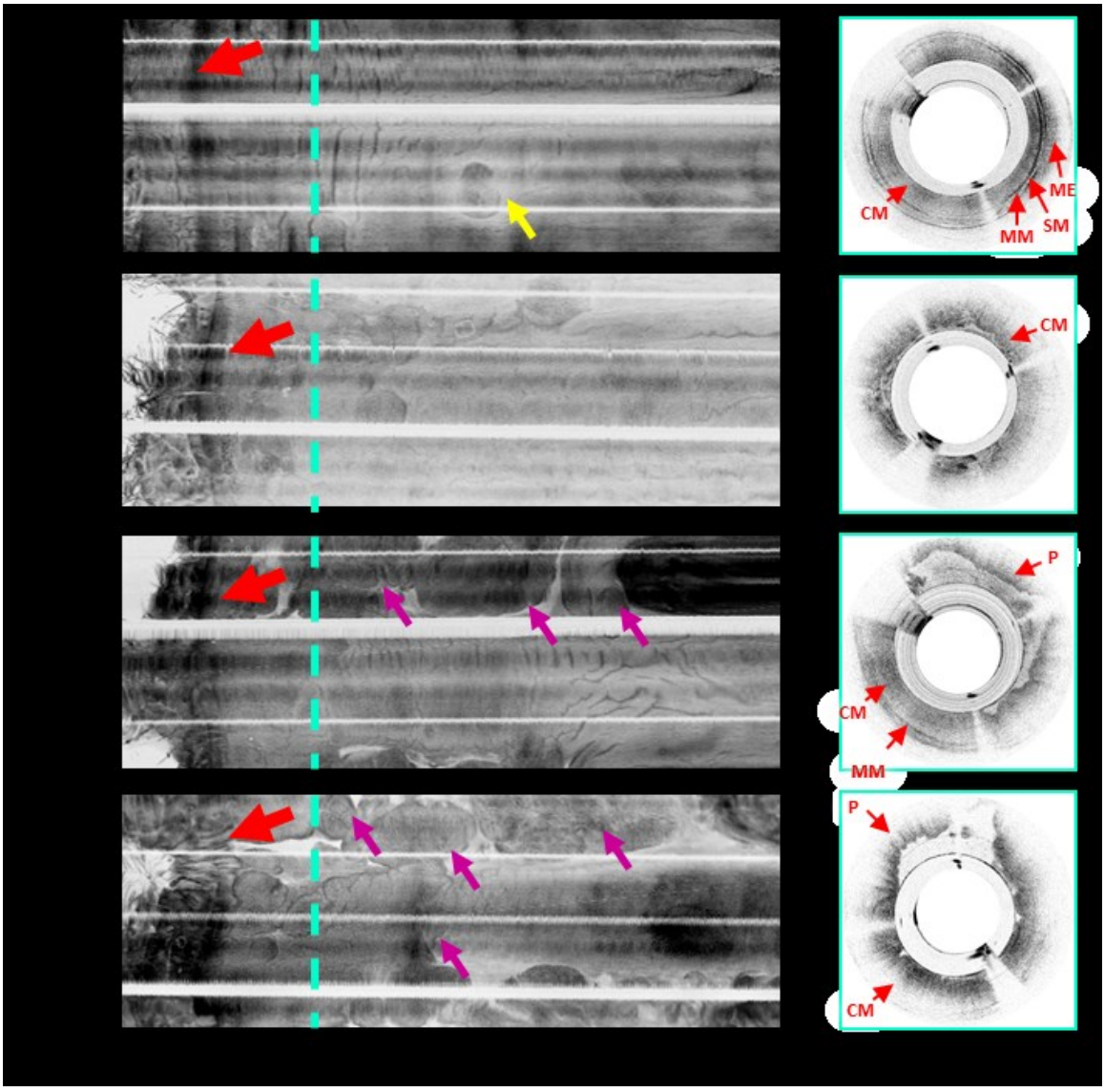

Figure 6.2: *En face* projection view and cross-sectional views of colon in M2.

The progression from mainly uniform and homogenous structural features in the baseline image (A) to many abnormal looking polyp structures can be seen (C), (E), (G) as the disease progresses to day 58. The red arrows point to a change from colon to rectum marked by the sudden hyperintense signal region. Cross-sectional images (B), (D), (F) and (H) are from the spatial

location of the cyan dashed line in (A), (C), (E), and (G). Several structures are labeled in the cross-sectional image, CM: colonic mucosa, MM: muscularis mucosa, SM: submucosa, ME: muscularis externa, S: serosa and P: polyp.

In addition to the *en face* projection views, a cross-sectional OCT image from the spatial location marked by the cyan dashed line (in each image) is shown to the right in Figure 6.2 B, D, F and H. The cross-sectional images give a clearer picture of the changing morphology of the colon over the eight weeks. The baseline image, Figure 6.2 B shows most of the normal colon structures such as the colonic mucosa, muscularis mucosa, submucosa, muscularis externa and serosa. By day 19, Figure 6.2 D, only the colonic mucosa can be seen with high signal attenuation due to continued inflammation in the colon. Figure 6.2 F shows an image from day 44 and by this time, the inflammation seems to have subsided yielding normal looking structures on the bottom right and a uniformly high signal attenuating region on the top and right areas of the frame. These areas are most likely due to the presence of a polyp. By the final time point day 54, the image in Figure 6.2 H shows relatively high signal attenuation across-the whole image frame and only the mucosa and what appears to be a polyp can be visualized.

These observations match with those from the *en face* projection view as well. For example, the baseline image (Figure 6.2 A) is relatively homogenous overall with the exception of one regions which may have developed spontaneous polyps early (marked by the yellow arrow). Then in the following time point, day 19 the image has an overall lower signal intensity due to the inflammation throughout the colon, and as time

progresses the signal intensity returns along with abnormal structural features corresponding to polyp growths (marked by purple arrows).

6.3.6 OCT- Histology Correlation

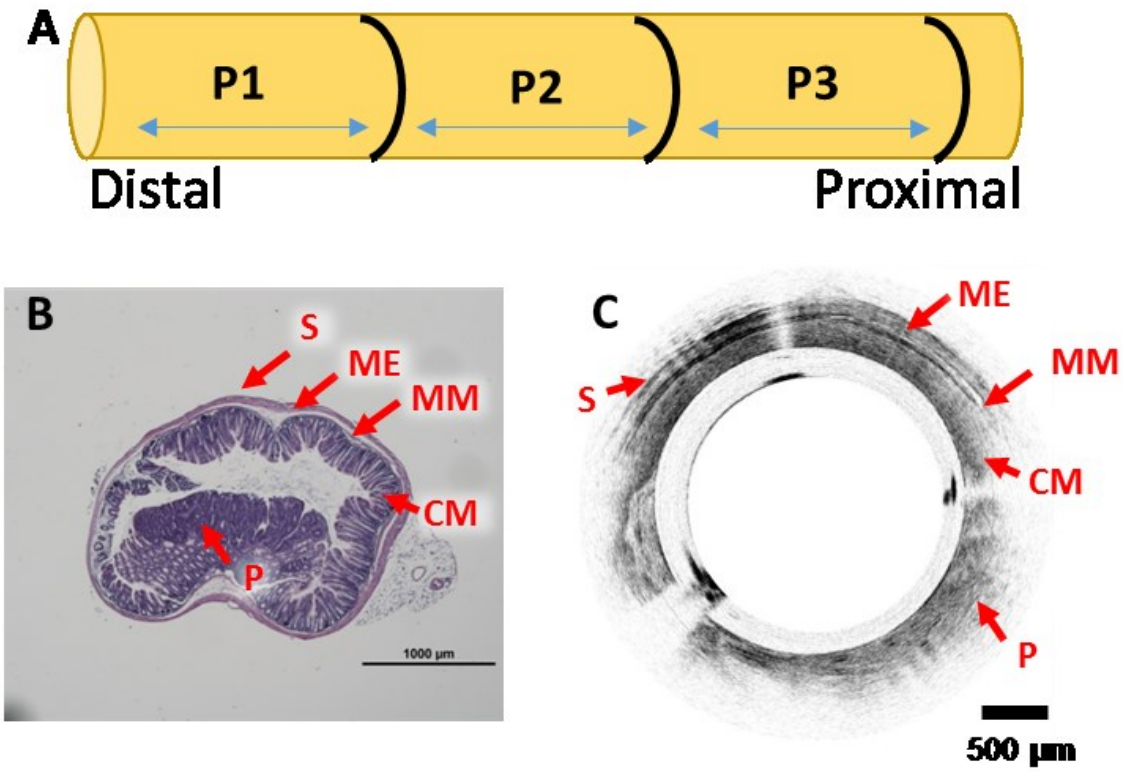

Figure 6.3: OCT-histology correlation from M2.

(A) Schematic representation of how colon was cut for histology. P1, P2 and P3 are 15 mm long segments of the colon cut and processed into blocks. (B) Histology slide from block P1 with corresponding cross-sectional OCT image (C). The OCT image shows a lack of defined structure on the bottom from the polyp structure. Several structures are labeled in the cross-sectional and histology images, CM: colonic

mucosa, MM: muscularis mucosa, SM: submucosa, ME: muscularis externa, S: serosa and P: polyp.

One way to confirm the presence of polyps in the colon to confirm the ability of OCT to visualize morphological changes and visualize polyp growth is through correlation with histology slides. Figure 6.3 A shows a schematic of how the colon from each mouse was cut for processing. Once dissected from the animal, each colon segment was cut from the rectum to a length greater than 6 cm into the large intestine. The OCT catheter was only inserted a maximum of 4 cm into the colon and less if impeded by stool or a large polyp. Thus, 3 cuts were made with each segment measuring ~15 mm. Each segment was processed into a block and histology slides were cut 1 mm from the edge into slides 100 μm apart.

The OCT cross-sectional images were sampled 20 μm apart over the total pull-back length. The oversampled OCT images and sparsely sampled histology ensured that an adequate frame correlation could be performed. The only caveat is that the animals did not undergo an enema to remove stool from the colon and it is possible that part of the field of view of the probe may be blocked by stool.

The histology slide shown in Figure 6.3 B is from segment P1 and was matched globally through the *en face* projection view, then locally by searching for matching features within the cross-sectional frames. The histology slide showed a relatively normal looking colonic mucosa with a very thin muscularis externa and muscularis mucosa and very little submucosa and a polyp growth in one location. In the global search, the *en face* projection view was searched for a singular polyp, as indicated by the rightmost located

purple arrow in Figure 6.2 G. After roughly locating the region where it resided, the OCT image frames 14 mm proximal to the rectum were identified and matched to the histology slide. The OCT image frame shown in figure 6.3 C was identified as the best match image.

Matching images in this respect with ultrahigh resolution endoscopic OCT can be difficult due to the limited depth penetration compared to 1300 nm endoscopic OCT. A greater penetration depth may have enhanced the ability to correlate the OCT-histology slide by matching the entire cross-sectional segment from colonic mucosa to the serosa. This may also have provided a more quantitative approach in being able to measure the polyp size and compare with histology. The drawback to using a longer wavelength source would be the inability to clearly visualize the thin layered structures such as the muscularis mucosa and fine microstructures such as crypts.

Understanding the limitations involved in correlation with histology, another method of performing quantitative analysis is by studying the attenuation coefficient in different regions of the colon.

6.3.7 Quantifying Attenuation in the Colon

One metric that can be calculated in OCT is the attenuation coefficient. Early in this dissertation, in chapter 2, there was a brief discussion of light tissue interactions where it was discussed that absorption and scattering phenomena govern the amount of light that can be backscattered towards the detector (for OCT). Since the amount of backscattered photons decrease with increasing sample thickness or imaging depth, the relationship can be described as an exponential decay where the decay constant is the total attenuation

coefficient. The attenuation constant varies for tissue samples under different conditions (e.g. tumor versus heathy tissue), making it particularly useful to find meaningful differences when there is a lack of sufficient microstructure to visually inspect the tissue sample.

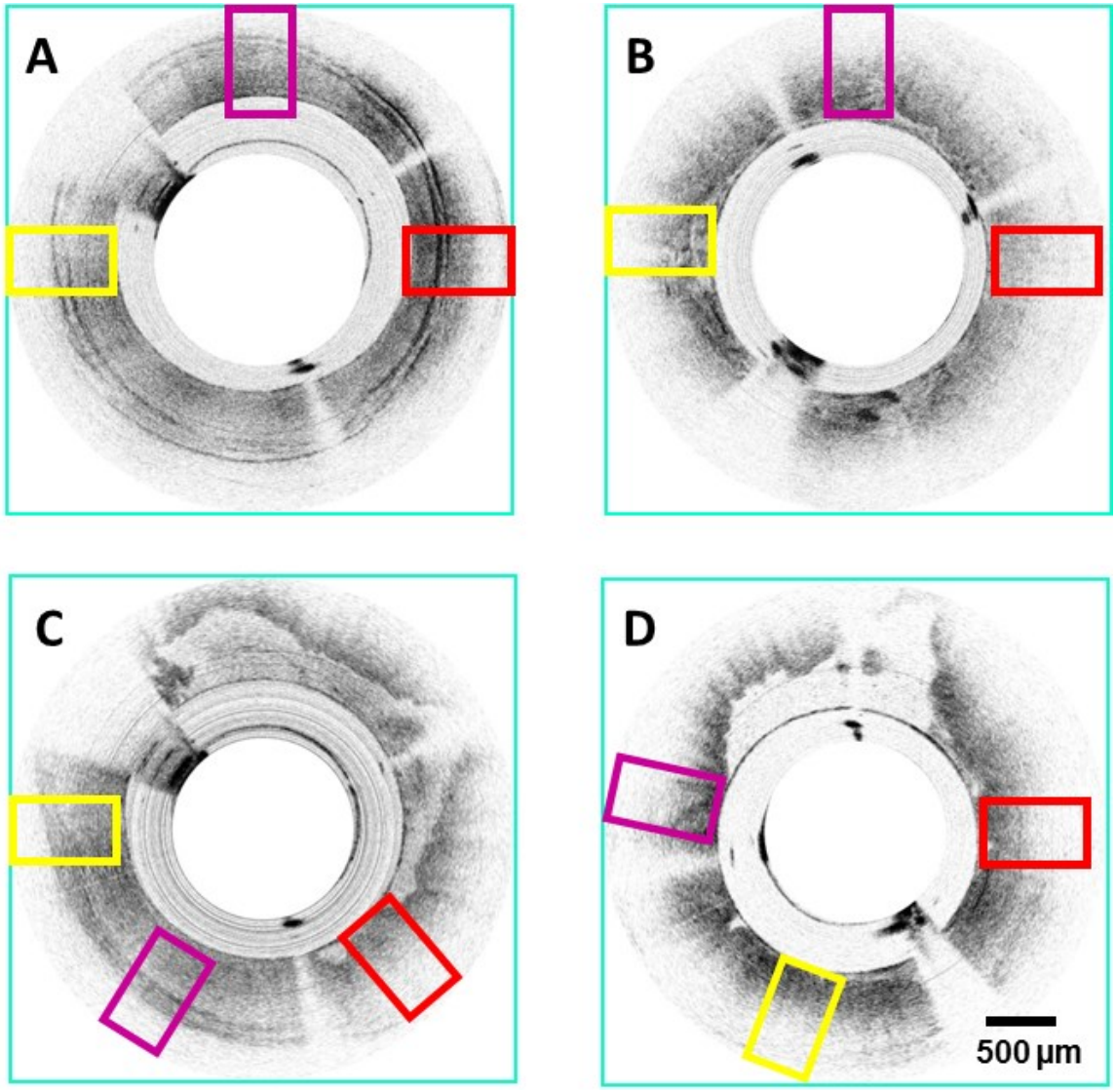

Figure 6.4: Segments used for calculation of attenuation coefficient.

(A-D) are the cross-sectional images shown in Figure 6.2 (B),(D),(F), and (G) marked with three regions over which attenuation coefficients will be calculated. Each region is enclosed by a red, yellow and purple rectangle. Regions with the most flat surface closest to the plastic sheath of the catheter were selected.

In this chapter, the attenuation coefficient is calculated for three areas in the cross-sectional images shown in Figure 6.2. Each region was selected through two criteria, 1) the region must be sufficiently flat and 2) the region must be in contact with the catheter plastic sheath.

The attenuation coefficient was calculated from the linear fitting the average of 50 A-lines over regions indicated by the red, yellow, and purple boxes shown in Figure 6.4. Before averaging each region of 50 A-lines, median filtering was performed to remove contribution of speckle noise and smooth the image for fitting. The results of linear fitting are shown in Table 6-3 with the hypothesized feature noted in parenthesis.

Frame	**Red** μ_t (Feature)	**Yellow** μ_t (Feature)	**Purple** μ_t (Feature)
A	2.48 mm^{-1} (normal)	2.66 mm^{-1}	2.52 mm^{-1}

		(normal)	(normal)
B	2.19 mm^{-1} (inflammation)	3.63 mm^{-1} (inflammation)	3.04 mm^{-1} (inflammation)
C	3.12 mm^{-1} (polyp)	2.68 mm^{-1} (normal)	2.76 mm^{-1} (normal)
D	3.44 mm^{-1} (polyp)	3.90 mm^{-1} (polyp)	3.96 mm^{-1} (polyp)

Table 6-3 Attenuation coefficients for features in cross-sectional OCT images from Baseline, day 19, day 44 and day 58.

The regions over which attenuation coefficients were calculated are shown schematically in Figure 6.4 through the red, yellow and purple rectangles. In parenthesis are the structural features that were observed or suspected (in case of polyp or inflammation) from the OCT image.

From Table 6-3, it is not clear if there is a relationship between the attenuation coefficient and normal or polyp regions in the OCT images. In order to elucidate this relationship, Figure 6.5 shows the histogram distribution of the attenuation coefficients in Table 6-3. Through the histogram it becomes clearer that there may indeed be a relationship between the attenuation coefficient and healthy and diseased regions of the colon.

This relationship is made clear in Figure 6.5 it can be seen that there may be a bimodal distribution where lower attenuation coefficients centered between 2.4 mm^{-1} -2.6 mm^{-1} correlate to healthy tissue while higher attenuation coefficients greater than 3.2 mm^{-1} correlate to polyp regions.

The histogram distribution also brings to light that the suspected features in Table 6-3, based on visual observation, may not be correct when it comes to differentiating inflammation from polyp regions. According to the distribution, the value highlighted in Table 6-3, which is thought to be inflammation may indeed be a polyp. For

This approach can provide valuable insights into the rate of polyp growth in this model, allowing the morphological changes to be visualized and quantified over the course of 8 weeks. The measurement of attenuation coefficient can also serve as an indicator of early morphological changes leading to polyp formation.

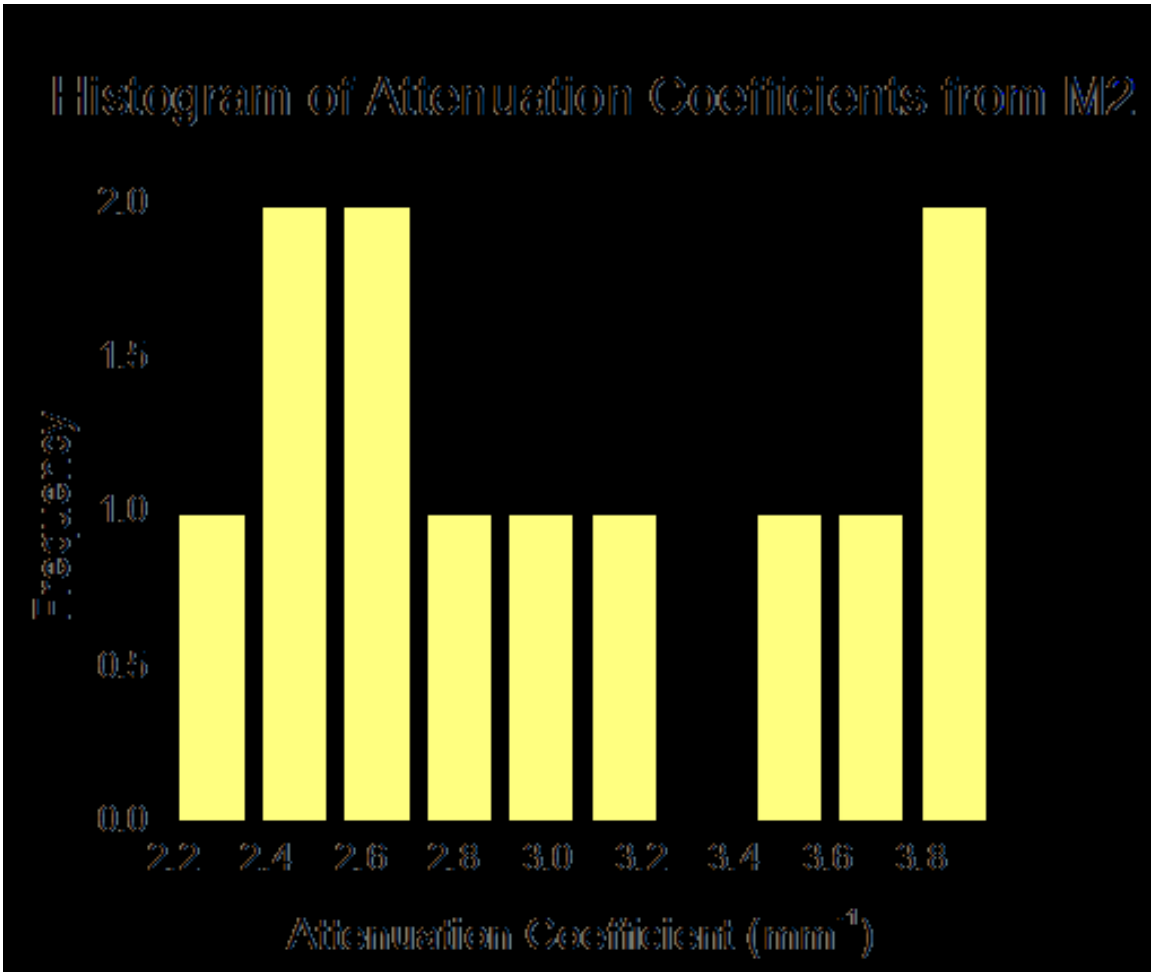

Figure 6.5: Histogram distribution of calculated attenuation coefficients from OCT images acquired in M2.

6.4 *Future Work*

In this chapter, it was shown that high speed, ultrahigh resolution endoscopic OCT imaging can be performed longitudinally in an ETBF induced CRC model in APC^{Min} mice. Specifically, this probe enables the ability to probe mice several times during the course of disease while minimizing trauma to the animal. Imaging time per mouse is minimized to less than 2 minutes (maximum given a frame rate of 50 frames-per-second).

A natural extension of this work is 1) performing better *in vivo* correlation with attenuation coefficient measurements and 2) employing attenuation coefficients to determine early morphological changes involved in polyp growth or establish growth trends in this model.

In order to perform better *in vivo* correlation, after OCT imaging has been performed the animal should be sacrificed and tissue processed into histology slides to be read by a trained physician to identify the state of the tissue (i.e. healthy versus polyp or inflammation, etc.). This should also be performed at different time points over 8 weeks to incorporate the variety of morphological changes occurring during the course of polyp formation. In this chapter, the need to perform histology for correlation at each time point made it impossible to study the morphological changes occurring over time in this model. Ideally, the measurement of attenuation coefficients would lead to a strong distribution with known thresholds for normal and polyp tissue.

This naturally leads to the second type of experiment that could be designed. Once there are known ranges of attenuation coefficients, these could be applied to *in vivo* imaging of CRC in this model to determine the trend of attenuation coefficients over the course of time. The trend of attenuation coefficients may shine light on the rate of polyp growth and possibly even allow for explanation for inter-animal variability. Another way to utilize the attenuation coefficient would be to analyze the trend leading up to full polyp growth. This may allow prediction of early changes leading to polyps that become malignant. In summation, the experiments described in this section would enable this

work to be extended to better understand the physiological changes in an ETBF induced CRC model in APC^{Min} mice and in turn the changes that occur in the human analog.

6.5 *Conclusion*

In this chapter, high speed, ultrahigh resolution endoscopic OCT has been used to visualize morphological changes in a mouse colorectal cancer model. These experiments showcased the ability of ultrahigh resolution endoscopic imaging to be performed numerous times within the same animal with little trauma to the animal, proving utility in longitudinal monitoring of disease progression. Furthermore, OCT was able to visualize changes in morphological structure over the course of 58 days after inoculation of ETBF. It was shown that among the morphological changes such as polyp formation could be observed. This chapter concludes description of research projects performed with ultrahigh resolution endoscopic OCT during the course of graduate studies.

The next two chapters will touch upon additional projects that have been completed during the course of studies and the final chapter will serve to summarize the work completed throughout my graduate studies by briefly summarizing the dissertation.

Chapter 7 Blood Flow Visualization

7.1 *Introduction*

This chapter will focus on the algorithms that have been employed to extract blood flow information from interference patterns acquired for structural imaging with OCT. The first half of this chapter will focus the significance of blood flow imaging and the types of algorithms that have been published in the literature while the second half will focus on results obtained in two animal models. The first animal model was middle cerebral artery occlusion while the second is a tumor angiogenesis model.

7.2 *Clinical Significance of Blood Flow Imaging*

Visualizing vascular networks is important in biomedical imaging for numerous reasons. The ability to visualize and detect blood vessels is important during real-time surgical procedures where a major artery may lie in the surgical path. In addition to real time imaging, understanding vascular changes in a disease states can help understand physiological responses as in stroke models. Yet another example of an important application for visualization of vasculature is in tumor angiogenesis, where visualizing growth patterns and the effects of therapeutic agents on growth patterns could help formulate new drugs for cancer therapy.

7.2.1 Middle Cerebral Artery Occlusion (MCAO) Stroke Model

Stroke affects an estimated 700,000 patients every year [264], and it is a debilitating disease causing many people to temporarily or permanently loose motor function. The

normal brain relies on a regulated supply of cerebral blood flow in order to function and a lack of adequate blood supply can lead to stroke due to ischemia. Although the brain possesses a unique ability to recover from traumatic events, one area of interest lies in the role of smaller vessels and capillaries in the severity and contrastingly recovery from traumatic events such as stroke, or brain injury. Temporal studies of ischemia, leading to stroke and subsequent infarction, note that there is a temporal window during which ischemia can be treated or reversed prior to irreversible infarction [265, 266].

Recently, there has been an increasing interest in imaging microvasculature within the Dura mater, meninges, and cortex using OCT as a noninvasive imaging modality for qualitative and quantitative blood flow visualization [267-269]. This was made feasible by Doppler OCT and related algorithms which detect the movement of blood flow based on the phase differences between adjacent axial lines [270-273].

7.2.2 Tumor Angiogenesis

Tumor angiogenesis describes the process of growth of new capillary blood vessels to support tumor growth and metastasis[274]. This phenomena has been noted for a long time, however only recently, in 1971, was it suggested that preventing tumor angiogenesis could help limit and possibly stop tumor growth [275]. This theory has led to the development of numerous cancer drugs in trial to inhibit vascular growth factors[276].

OCT presents an interesting opportunity to visualize tumor angiogenesis due to the fact that it can perform structural imaging to visualize growth of tumor while complementary obtaining flow information through the same data sets. This allows for

study of structural changes as well as vascular changes in cancer models. Specifically, this technology enables real-time, noninvasive, non-contact visualization of changes in vasculature during tumor growth and upon application of therapeutic agents. There have been a few studies have been employed OCT to study the tumor microenvironment to visualize morphological and vasculature change [277, 278].

7.3 *Vascular Visualization*

As mentioned above, vascular visualization has become increasingly important for biomedical applications and further understanding of many disease mechanisms. This section will focus on three types of image processing algorithms employed for flow visualization. Broadly the image processing algorithms can be categorized into intensity based, phase based, and frequency based algorithms. Intensity based algorithms take advantage of decorrelation of speckle patterns to filter out static signals and highlight rapidly changing patterns that are correlated to flow. Phase based algorithms take advantage of phase shifts induced by the Doppler frequencies to capture flow velocity or variances related to the Doppler frequency spectrum. Finally, frequency based algorithms try to take advantage of a range of frequencies within the spatial frequency spectrum to visualize and quantify flow velocity and directionality.

7.3.1 Intensity Based Algorithms

Intensity based algorithms for flow imaging is useful in situations where the system is unable to be phase stable. This is particularly important for *in vivo* imaging where physiological motions such as heart rate and respiration may transfer to the system or simply contaminate the data. Another important source of phase instability can come

from the OCT laser engine as in the case of swept sources <enter references> or from the laser scanning mechanism such as galvanometer scanners which may cause jitter between A-line acquisition, inducing unwanted phase noise.

There are three main intensity based methods to extract the flow information based on intensity changes in the OCT structural images. The first is speckle variance OCT (SV-OCT), the second is intensity based Doppler variance (IBDV) and the third is phase insensitive angiography.

7.3.1.1 Speckle variance OCT (SV-OCT)[278-280]

SV-OCT is based on the principle that speckle patterns de-correlate faster for fluids moving through a cross-sectional image frame compared to static tissue structures. SV-OCT can be calculated from cross-sectional OCT images through the following equation:

$$SV_{ijk} = \frac{1}{N}\sum_{i=1}^{N}\left(I_{ijk} - \frac{1}{N}\sum_{1}^{N} I_{ijk}\right)^2. \qquad 7.1$$

SV_{ijk} is the variance of pixel I_{ijk}over N image frames. This calculation is quick and simple to implement for real-time image processing and is fairly robust in the event of minimal tissue motion.

The overall signal-to-noise ratio of the vascular images can be increased by increasing the number of image frames, N, that are employed for averaging, when there is minimal tissue motion. Furthermore in the event of excessive tissue motion, image registration techniques can be employed prior to speckle variance calculation to improve the signal-to-noise ratio.

The major advantage of SV-OCT over the IBDV is the ability to be used for real-time calculation due to its simplicity and that it is independent of frame rate. The speckle decorrelation

phenomena can be taken advantage of without consideration towards inter-Aline or inter-frame time difference, allowing the frame-rate to be as high as possible for a given system as long as sufficient sampling occurs between B-frames. These advantages also come with a drawback that due to the lack of dependency on time, this algorithm cannot be used to obtain quantitative flow velocity or directional information. Nevertheless SV-OCT has been successfully implemented and employed easily in phase unstable systems for quick, real-time visualization of vascular networks[280].

7.3.1.2 Intensity Based Doppler variance (IBDV) [281-283]

IBDV is based on modifications of Doppler variance algorithm. Doppler variance algorithms (further discussed below) calculate the variance of the average Doppler flow velocity, using both phase and intensity information. IBDV methods are based on the same concept as phase resolved Doppler variance however all phase relationships are canceled out, by using the magnitude instead of complex value of each pixel. The resulting equation to calculate the variance is shown below:

$$\sigma^2 = \frac{1}{T^2}\left[1 - \frac{\sum_{j=1}^{J}\sum_{z=1}^{N}(|A_{j,z}||A_{j+1,z}|)}{\sum_{j=1}^{J}\sum_{z=1}^{N}\frac{1}{2}\left(|A_{j,z}|^2+|A_{j+1,z}|^2\right)}\right]. \quad 7.2$$

The variance, σ^2, is dependent on the magnitude of signal at the same depth pixel z between two adjacent A-lines, $A_{j,z}$ and $A_{j+1,z}$. When there is a larger magnitude difference between two adjacent A-lines due to moving particles and decorrelation of speckle patterns, the variance is greater indicating a broader Doppler frequency spectrum and greater variations in flow velocities. The dual summations in the numerator and denominator over *J* A-lines and *N* depth pixels are for lateral and depth averaging which increase the image SNR at the cost of computational time.

One of the major advantages of IBDV is its ability to be used in phase unstable systems such as swept source OCT and is completely independent of phase. In comparison with phase resolved color Doppler, this algorithm was able to visualize vessels without bulk motion correction and was easy to implement [281]. The only drawbacks are the lack of quantitative information and of course cost of computational time as further averaging is performed.

7.3.1.3 Phase Insensitive Angiography [284]

Phase insensitive angiography was a method, derived from phase sensitive angiography to quickly generate an angiogram for real-time visualization. This algorithm is perhaps the simplest of the three phase insensitive algorithms described in this section. The cross-sectional angiogram is calculated by taking the magnitude of the magnitude differences between alternating (even and odd) B-frames.

$$\left|\Delta A_{phase-insensitive}\right| = \left|\left|A_{2n}\right| - \left|A_{2n-1}\right|\right| \tag{7.3}$$

One of the caveats in this algorithm is that the scanning protocol requires each frame to be repeated twice before movement to the next spatial location. Thus each cross-sectional angiogram is calculated from the same spatial location, allowing for enough decorrelation between flow related pixels to be highlighted and enough correlation from static structures to be canceled out.

In comparison to its phase sensitive counterpart, this angiogram generation is noisier since there are no phase shift or motion corrections employed. Regardless, this algorithm results in a decent generation of an angiogram with little overhead or processing requirements and provides good results if there is minimal motion artifact during sample imaging.

7.3.2 Phase Based Algorithms

Phase based algorithms use phase differences between adjacent A-lines within a frame or between frames to calculate the average Doppler frequency or the phase variance of the Doppler velocity, in order to visualize the vascular networks. These algorithms are dependent on the time difference between measurement points allowing them to be used for quantitative measurements. The two methods that will be described below are phase resolved color Doppler which measures the Doppler frequency and phase resolved Doppler variance which is a measure of the width of the Doppler frequency spectrum.

7.3.2.1 Phase Resolved Color Doppler (PRCD) [282, 285]

PRCD is the most basic algorithm that takes advantage of the phase shifts incurred due to the Doppler frequency from moving particles. PRCD obtains the average Doppler velocity from the ratio of the phase shift between two adjacent A-lines over the time interval between the two A-lines. This method is purely based on the phase and has very high velocity sensitivity when the flow direction is collinear with the probing beam. Equation 7.3 shows the relationship between the averaged Doppler frequency, $\bar{f}$ and the phase difference between two adjacent A-lines for a given depth pixel.

$$\bar{f}(z) = \frac{d\theta(z)}{dt} = \frac{\theta_{j+1,z} - \theta_{j,z}}{T} \qquad 7.4$$

The associated velocity is then calculated by[286] $v(z) = \frac{\lambda}{2}\bar{f}(z)$.

This method has two main drawbacks. Firstly, as mentioned above, this method is highly dependent on the direction of flow with respect to the incident beam, thus as the direction of the flow becomes closer to perpendicular this method becomes less sensitive.

Secondly, this method depends upon the time interval between two A-lines. For slow flow speeds, there may not be a detectable phase change between two adjacent A-lines and the algorithm may need to be applied between frames or may need to significantly down sample or slow acquisition rates in order to detect slow flow velocities. Alternatively high flow velocities could be miscalculated due to aliasing and phase wrapping if the tissue is under-sampled in the time domain. Thus this algorithm is very sensitive to sampling errors and best operates under known flow velocity conditions.

7.3.2.2 Phase resolved Doppler variance (PRDV) [272, 285]

Phase resolved Doppler variance is used to calculate the variance of the Doppler frequency spectrum. The variance is related to the width of the Doppler frequency spectrum where greater variations in flow velocity relate to a higher phase variance [285].

The variance can be calculated, using autocorrelation relationships, with the following equation[282]:

$$\sigma^2 = \frac{1}{T^2}\left[1 - \frac{\sum_{j=1}^{J}\sum_{z=1}^{N}\left|\left(A_{j,z}A_{j+1,z}^{*}\right)\right|}{\sum_{j=1}^{J}\sum_{z=1}^{N}\frac{1}{2}\left(A_{j,z}A_{j,z}^{*}+A_{j+1,z}A_{j+1,z}^{*}\right)}\right]. \quad 7.5$$

In Equation 7.4, there are two sets of summations for averaging in the lateral and depth directions to improve the signal-to-noise ratio. As in IBDV, $A_{j,z}$ is the complex value of the z^{th} pixel, in the j^{th} A-line, and $A_{j+1,z}$, is the complex value of the z^{th} pixel in the adjacent A-line.

Due to the fact that the variance is not directly related to the frequency but the width of the frequency spectrum, the algorithm has several advantages such as insensitivity to Doppler angle, pulsatile nature of blood flow, and is robust against bulk motion [287]. One of the downsides of this algorithm in contrast with PRCD is that it

cannot provide a direct quantitative measurement of flow velocity however it can be calibrated to provide an estimate [288].

7.3.3 Frequency Based Algorithms

It was briefly mentioned above that frequency based algorithms seek to take advantage of the spatial frequency spectrum in cross-sectional images by analyzing the high spatial frequencies that are related to flow imaging within the frame. The most popular algorithm employed to accomplish this is coined optical angiography (OAG) or optical micro-angiography (OMAG).

7.3.3.1 Optical Angiography (OAG)

In optical angiography the goal is to be able to extract Doppler frequencies that arise due to moving particles that backscatter light within the sample. A modulation frequency is introduced to modulate the spatial frequencies within the image frame.

Physically, within the OCT system, frequency modulation may be performed using a piezoelectric actuator in the reference arm to induce a Doppler frequency[289-291], inducing a frequency shift by scanning the sample arm galvanometer mirror off-axis[292-294], or with a phase modulator[295-297] as was originally demonstrated for full-range OCT imaging.

The modulation frequency helps map spatial frequencies due to moving particles onto one image or one side of the Fourier transform and the spatial frequencies of the static scattering particles onto a separate image or the opposite side of the Fourier transform. The determination of whether the moving particles are in the positive or

negative frequency space depends upon the direction of the modulated Doppler frequency (i.e. moving into or out of the image frame). If the frequency of the moving particles are moving at a speed greater than the Doppler frequency the particles will be mapped to the positive space, however if the particles are moving in the opposite direction, they will be mapped into the negative frequency space. Since the moving particles can only be detected if they induce a Doppler frequency, there is a minimum velocity that can be detected based on the modulation frequency [289]:

$$\pm v_{min} = \mp f_M \frac{\bar{\lambda}}{2\cos(\beta)}. \tag{7.6}$$

In this equation, f_M is the modulation frequency, and $\lambda$is the central wavelength of the light source with β the angle between the probe and the direction of flow particles. Finally in order to extract the flow signals, the Hilbert transform of the interferogram (of the whole OCT image frame) is filtered along the spatial frequency axis. The induced Doppler frequencies will reside around the modulation frequency, while the static signals will be centered about zero frequency.

As seen from equation 7.6, this algorithm enables flow velocities to be measured with directionality making it a powerful algorithm for biomedical imaging applications where vascular patterns need to be studied quantitatively. While it is a powerful algorithm, it is difficult to implement due to the numerous image processing steps required to obtain low noise signals. The algorithm will be affected by bulk motion, physiological motion, and requires significant consideration of sampling intervals and the induced Doppler frequency. Additionally, since there is a hardware aspect to this

algorithm to implement a modulation frequency, there can be addition noises from hardware such as jitter, making it difficult to effectively filter out static signals from moving particle signals in the frequency domain. This is only made more difficult from very heterogeneous tissue samples that may span a broad spatial frequency range.

7.4 *Methods*

7.4.1 Imaging System

Figure 7.1 depicts the schematic of the ultrahigh-resolution SD-OCT system. The SD-OCT engine is essentially the same as what was described in Chapter 3 however it was employed in free-space with a 50/50 beam splitter cube.

The broadband Ti:Sapphire laser had a 3dB bandwidth of ~150 nm around a central wavelength of 830 nm. Finally, the imaging spectrometer is the same as that described earlier in chapter 3. Briefly, the spectrometer is capable of accommodating a ~240 nm spectral bandwidth over the width of the 2k pixel linear CCD array. The spectrometer design achieved a spectral resolution of 0.121 nm and a calibrated imaging depth of 1.23 mm and was able to acquire 70k A-lines-per-second.

The reference arm as shown in Figure 7.1 contained an achromatic collimating lens, a BK-7 prism pair for dispersion compensation, and a variable neutral density filter to ensure operation in the shot noise range (the filter is not shown in the schematic). The sample arm optics consisted of a pair of galvanometer mirrors for X and Y scanning and telecentric scanning lens (Thorlabs LSM02-BB). In order to perform telecentric imaging along the frame, the Y galvo was maintained at the appropriate scanning distance of 16

mm away from the aperture of the imaging lens. The imaging lens allowed for a working distance of 7.5 mm from the lens surface and enabled us to achieve a lateral resolution of 16 µm and maintained an axial resolution of 2.8 µm with the broadband Ti:Sapphire laser.

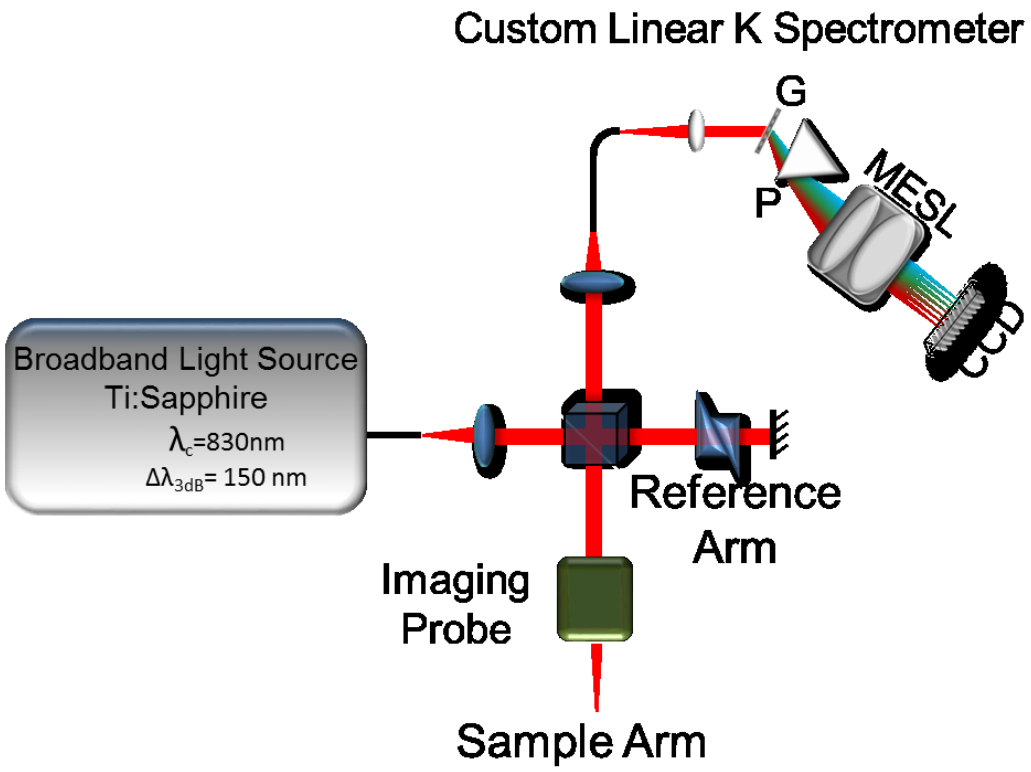

Figure 7.1: Free space SD-OCT system.

G: grating, P: prism, MESL: multi-element scanning lens, and CCD: linear CCD array.

7.5 *Results*

Vascular networks were visualized in two distinct models in order to test the feasibility of the system with respect to known physiological phenomena. The first model that will be discussed is a middle cerebral artery occlusion MCAO model. Occlusion models are

frequently used to study the effects of stroke by restricting blood flow to a major supply artery in the brain.

The second model that will be discussed is a mouse tumor model. A tumor has been grown on the ear of a nude mouse in order to visualize vascular network changes during tumor angiogenesis.

7.5.1 Middle Cerebral Artery Occlusion (MCAO)

Phase resolved Doppler variance and phase insensitive angiography algorithms were used in prior experiments and showed higher background noise in comparison to the SV-OCT based angiograms presented in Figures 7.2 and 7.3. The background noise is possibly due to physiological bulk motion such as brain shift within the skull, respiration, heart rate and pulsatile nature of blood flow. We found that the ability to increase signal-to-noise ratio through averaging in SV-OCT was helpful and allowed vasculature to be visualized with low background noise.

7.5.1.1 Animal Protocol

All imaging was performed under protocols approved by the animal use and care committee at Johns Hopkins University. The mouse was first anesthetized via an intraperitoneal injection of mouse mix (100mg/kg Ketamine and 10 mg/kg Xylazine), after which a cranial window of 4mm by 4mm was implemented over the right hemisphere and sealed with a glass-slide. Once the cranial window was implemented, a surgery was performed to suture-shut the middle cerebral artery. This procedure could be reversed by releasing the suture, however for the set of experiments that was performed, the suture was shut and the animal was sacrificed after the experiment.

An imaging clip was glued to the front part of the skull to ensure mount to a pole for imaging. Head mounting ensures that position is not shifted during imaging so the same field of view can be acquired over the 2 hour period during which imaging was performed.

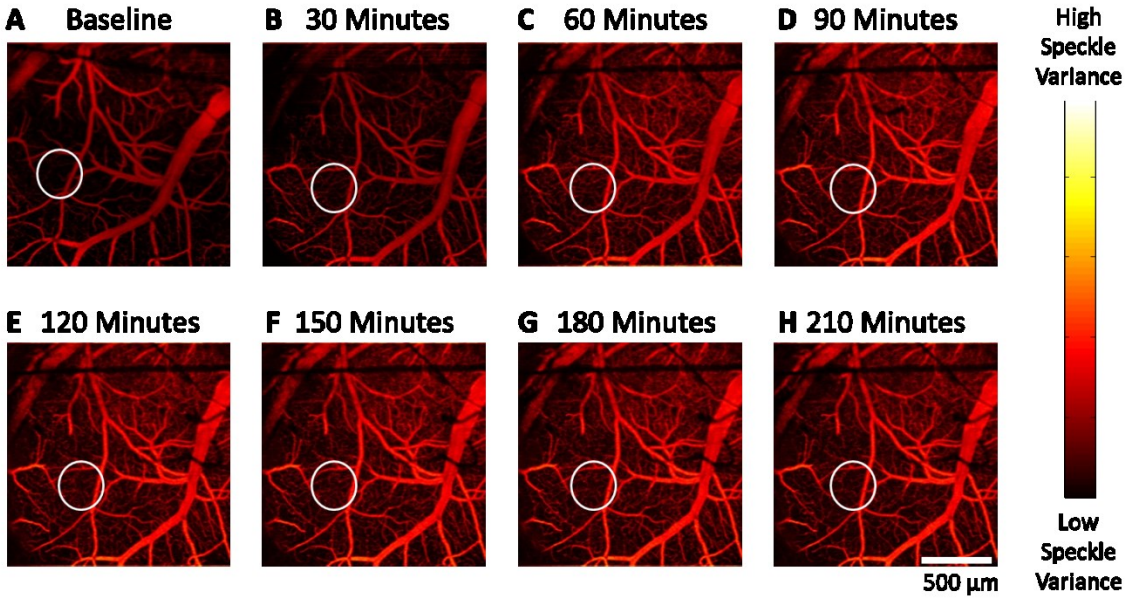

Figure 7.2: *En face* projection view Doppler variance imaging of MCAO through a cranial window in a mouse model.

(A) Baseline image of the mouse brain before surgery. (B-H) Post-surgical angiograms acquired immediately after surgery and every 20 minutes thereafter. The circled regions mark areas where vascular patterns have changed due to diversion of blood flow.

7.5.1.2 Imaging Protocol: Speckle Variance OCT

Immediately after surgery 3D OCT volumes (2 mm by 2 mm) were acquired every 20 minutes through the cranial window. The OCT volume consisted of 1024 A-lines per frame over 2 mm with 1024 frames distributed over 2 mm. This provided enough sampling to employ the phase resolved Doppler variance method between adjacent A-lines as described in section 7.3.2.2 [272].

7.5.1.3 Angiography of MCAO

Figure 7.2 shows *en face* projection views of the depth averaged speckle variance OCT images before surgery (Figure 7.2 A), immediately post-surgery (Figure 7.2 B) through 20 minute increments up to 210 minutes post-surgery (Figures 7.2 C-H). The angiograms are shown in a red hot colormap, with white corresponding to high variance and black low variance. As mentioned earlier variance represents greater variation of Doppler frequencies, thus larger vessels show a greater variance than smaller vessels.

The white circle in the bottom left hand side of the projection views has been highlighted to show that different blood vessels are visualized over time due to diversion and reassignment of blood flow. This can be seen more clearly in Figure 7.3 where these regions have been magnified. Two specific changes have been highlighted with yellow and white arrows in Figure 7.3.

The yellow arrows indicate a vessel that could barely be seen in the baseline image that showed a forked path on the top right at 30 and 60 minutes, which was slowly diverted and seemingly cut off after 90 minutes. Contrastingly, the white arrow shows new vascular paths that have been reinforced with greater blood flow until Figure 7.3 H

at 210 minutes where it seems that there is an overall reduction in blood flow in this region. These two opposing phenomena show that the vascular changes in this model are complex and restricted blood flow can be diverted to different regions of the brain.

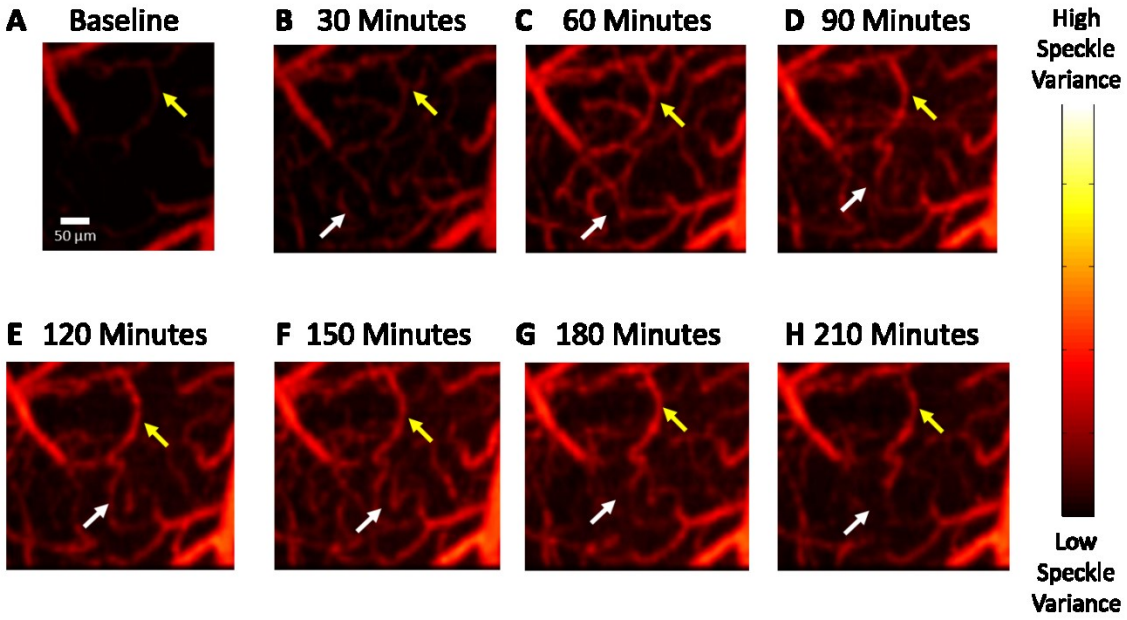

Figure 7.3 4x magnified vascular changes in MCAO model.

All images are 4x zoomed-in regions marked by white circles in the angiograms from Figure 7.2. (A) Baseline image of the mouse brain before surgery. (B-H) Post- surgical angiograms acquired immediately after surgery and every 20 minutes thereafter. White arrows indicate diversions of blood flow as a result of occlusion of the middle cerebral artery.

7.5.2 In Vivo Tumor Angiogenesis

The tumor angiogenesis model was imaged with a phase insensitive angiography method. This method is even simpler than the SV-OCT method and was able to be used due to the minimal bulk motion artifacts for ear imaging. Excessive averaging was unnecessary to obtain quick, reliable angiograms with low noise.

7.5.2.1 Animal Protocol

All imaging was performed under protocols approved by the animal use and care committee at Johns Hopkins University. The mouse was first anesthetized via an intraperitoneal injection of mouse mix (100mg/kg Ketamine and 10 mg/kg Xylazine), after a subcutaneous injection of A431 cells for tumor growth. Tumor growth was monitored up to 34 days after which the animal was sacrificed.

During imaging, the animal was anesthetized with mouse mix and placed in a custom designed mount to ensure that there was no bulk motion present during imaging.

7.5.2.2 Imaging Protocol: Phase Insensitive Angiography

Imaging was performed over 3 areas, 1) normal ear region at edge of ear, 2) directly on tumor region on days 25, 31, and 34 and3) adjacent to the tumor region on days 25, 31, and 34. During each imaging session, the acquired OCT volume consisted of 1024 A-lines per frame over 2 mm with 1024 frames distributed over 2 mm. Each B-frame was repeated once making the total number of frames in the volume 2048. Angiograms were generated using the phase insensitive angiography method described in section 7.3.1.3 [284].

7.5.2.3 Angiography of Normal Nude Mouse Ear

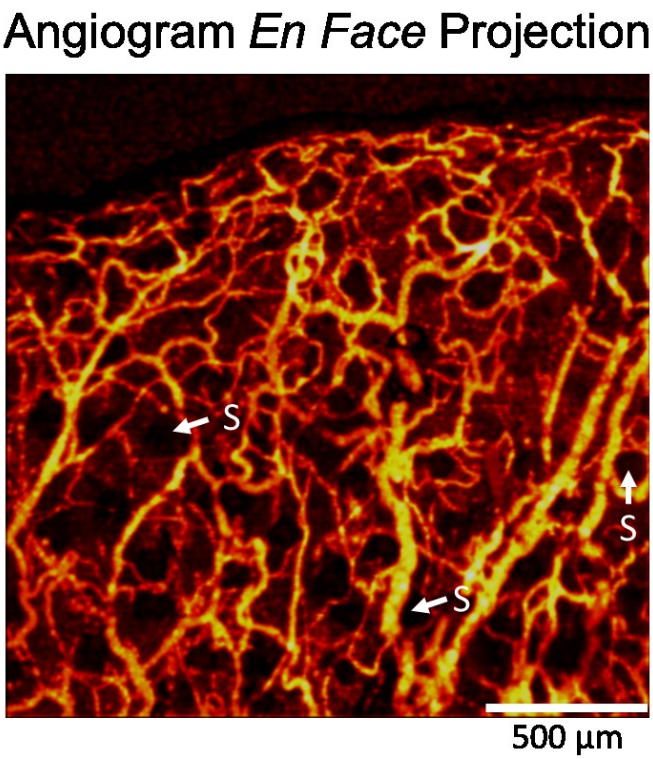

Figure 7.4 E*n face* angiogram of normal nude mouse ear.

A few sebaceous glands are pointed out to indicate the strong signal attenuation experienced by OCT when imaging sweat glands in the ear. S: sebaceous glands.

Figure 7.4 shows the *en face* angiogram generated through phase insensitive angiography of normal, healthy nude mouse ear. The edge of the ear can be seen on the top edge of the image, where vasculature stops. A few arrows in the image point to sebaceous glands. Although, there are many glands throughout the ear, a few have been pointed out to note that sebaceous glands are highly scattering structures that significantly attenuate penetration beyond the gland. Thus, there are several places in the angiogram where it

appears as a circular signal void region, due to the fact that no vessels under the glands could be visualized due to limited backscattered light.

7.5.2.4 Angiography of Tumor Angiogenesis in Nude Mouse Ear

Figure 7.5 shows some results from imaging the tumor and tumor periphery areas. In Figure 7.5 A-C, the images are labeled with P to indicate the relative location of the peripheral image shown in Figures 7.5 D-F, and similarly the peripheral images are labeled with T to show the relative location of the tumor.

Upon first inspection it can be seen that on day 25 there seems to be a higher density of vessels on the tumor region in comparison to day 31 and 34. It is believed that as the tumor continued to grow, it became necrotic and the blood flow was diverted away from the main tumor site. Contrastingly, the tumor periphery shows interesting changes. On day 25, vessels are seen leading to the main tumor region. The vessel paths have already become convoluted and tortuous in comparison to the normal mouse ear shown in Figure 7.4. As the tumor grows, the vascular network becomes more intertwined and dense, until day 34 when it seems as there are is a dense network of vessels that can be seen until the edge of the tumor region.

It is difficult to visualize the vasculature going to the tumor region on day 34, as it is shown on day 31 due to the physical size of the tumor. The large height difference of the tumor with respect to the boundary region did not allow for the transition zone to be within the same field of view for imaging. Hence the network connections heading to the tumor region were not able to be identified as clearly as in the day 25 and 31 time points.

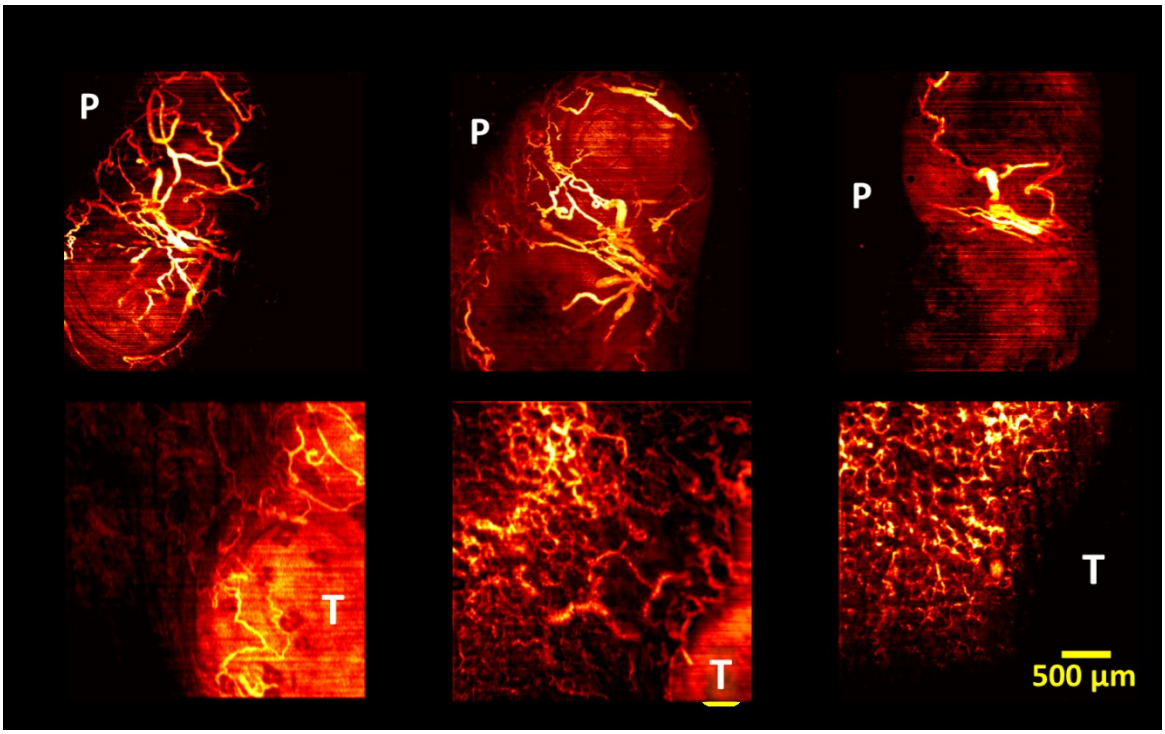

Figure 7.5 Tumor angiogensis in nude mouse ear.

Three representative *en face* projection view of angiograms from a tumors (A-C) and the corresponding tumor boundary (D-F) are shown for days 25, 31 and 34 during tumor growth. P: periphery and T: tumor.

7.6 *Future Work: Endoscopic Angiography*

Angiography has shown great potential in numerous applications, specifically with respect to cerebrovascular imaging [267, 269]and tumor angiogenesis[277, 278]. The ability to perform angiography is still limited by the necessity to be performed on benchtop systems. The requirement for highly stable environments that are extremely sensitive to phase or frequency represent a major issue when considering angiography for clinical use in humans *in vivo*. Thus, intensity based algorithms may provide a good solution for endoscopic OCT imaging *in vivo* in clinical settings.

Recently there has been some work to show that it would be possible to perform angiography endoscopically [130, 298]. This paper primarily focused on a 1300 nm VCSEL light source and a distal scanning catheter; however, angiography was demonstrated from data acquired in *in vivo* human esophagus. This is quite possibly the first demonstration of angiography performed from endoscopic OCT data. The angiogram was affected by rotational distortion as well as distortion upon catheter pull-back, however these could be easily resolved through post-processing [172]. Hence, future work should also attempt to visualize vasculature endoscopically and further understand the best algorithms for this application.

7.7 *Conclusions*

This chapter is one of two chapters focusing on other projects that were completed during the course of my graduate research studies. This chapter is dedicated to imaging vasculature through image processing algorithms applied on OCT interference signals. The chapter began with a brief overview of the biological need for vascular imaging with respect to stroke and tumor angiogenesis. Three categories of image processing algorithms, intensity based, phase based and frequency based, were briefly described with some implementations.

Finally, we presented results obtained with the high resolution SD-OCT system acquired using speckle variance and phase insensitive angiography methods in a middle cerebral artery occlusion and tumor angiogenesis model. These results demonstrated the ability to visualize vascular network changes due to physiological phenomena.

The next chapter will focus on another project completed during graduate studies, a multimodal OCT and fluorescence imaging platform for endoscopic imaging. Finally, the dissertation will be summed up and concluded in the final chapter.

Chapter 8 Multimodal Endoscopic OCT and Fluorescence Imaging

8.1 *Introduction*

This chapter will present a project that was completed during the course of graduate studies and is related to endoscopic OCT imaging. This chapter will discuss the engineering and implementation of an entirely fiber optic endoscopic multimodal OCT and fluorescence imaging platform for simultaneous imaging. The methods and results described in this chapter have been published [299, 300].

8.2 *Background*

Throughout this dissertation it has become clear that OCT is able to provide high resolution morphological information with high speed, however, one caveat is that OCT lacks of molecular sensitivity, which can be crucial in order to draw conclusions for medical diagnosis.

Alternatively a complementary imaging modality to provide molecular information is fluorescence imaging. Additionally, fluorescence imaging has been performed endoscopically in the gastrointestinal tract for cancer screening/diagnosis[301], where generally only surface images with low resolution are generated without depth-resolved high-resolution tissue microstructure information. Another example of endoscopic fluorescence imaging is the fluorescence confocal endomicroscopy technology [302]. Fluorescence confocal endomicroscopy takes

advantage of exogenous fluorophores such as intravenously administered fluorescein to visualize tissue microstructures with a superb resolution comparable to histology. The drawback to this approach is that image depth and field of view are both limited.

The complementary nature of OCT and fluorescence imaging can provide a great advantage for image guided biopsy and disease diagnosis. Thus, there is a critical need to for multi-modal imaging to visualize tissue microstructure with high resolution and gain molecular information simultaneously.

8.2.1 Benchtop Multimodal Systems

The nature of multimodal imaging has been an attractive concept before the ability to engineer multimodal endoscopes and was originally demonstrated in benchtop systems [303-305]. Benchtop multimodal systems often employ a complex combination of fiber optic and free-space components in order to combine and separate fluorescence and OCT light. One of the major design challenges is being able to ensuring efficient operation over both fluorescence and OCT wavelength ranges.

Numerous benchtop systems have been devised for a combination of OCT and fluorescence imaging, one example is OCT and laser induced fluorescence (LIF) system, a fiber optic OCT module was combined in free-space with the LIF system [303, 306]. The source lights were combined and separated through a free-space beam splitter and an uncoated calcium-fluoride lens which was able to operate over the necessary broad spectral bandwidth from 300-1500 nm. Scanning the laser beam with this configuration would have resulted in numerous optical aberrations degrading the image quality, so the sample was placed on a motorized translation stage for scanning. Through further consideration of the beam path it is possible to perform beam scanning with a

galvanometer mirror [305]. Nevertheless, these systems are complex with numerous optical components to combine and separate light paths and the success of these systems in cell and tissue imaging has brought about further interest in endoscopic multimodal systems.

8.2.2 Endoscopic Multimodal Systems

In order for multimodal imaging to be effective towards guidance and diagnosis it needs to be implemented in an endoscopic platform such that internal organs can be imaged in a clinical setting. Prior to the publication of this all fiber-optic multimodal platform a few designs had been implemented in an attempt to perform multimodal imaging endoscopically.

One of the early designs had a multimodal endoscope designed with multiple optical fibers with one for sending/receiving OCT source and backscattered light, and another for delivery of fluorescence excitation and a third for fluorescence emission collection[307, 308]. With the use of a total internal reflection through a reflective ball lens, the light was able to be deflected 90° to a focal plane 30 μm from the outside of the probe. The multiple-fiber based design led to a complicated imaging system setup and made it difficult to introduce a radial scanning mechanism. Thus this design only allowed for B-frame imaging through a pull-back mechanism. The capability of this endoscope was demonstrated in *in vivo* mouse colon where the OCT provided images of healthy colon tissue as well as adenomas within the same image frame and laser induced fluorescence spectroscopy provided unique spectra for healthy and adenomatous regions.

A major improvement on the multiple fiber based design came when a double-clad fiber coupler was presented and allowed for fluorescence and OCT light to be

combined and separated fiber-optically[309-313]. These systems demonstrated the ability to perform OCT imaging and obtain fluorescence spectra using a double clad fiber coupler, but did not provide convincing results in an *in vivo* animal model due to the lack of multimodal endoscope. Most results were demonstrated with a lensed fiber[309] or with an galvanometer scanner[311].

Nevertheless, this design represented a major change in the way multimodal endoscopic imaging could be performed. Soon after numerous double clad fiber based designs were published. One such design employed double clad fiber (DCF) in conjunction with a fiber-optic rotary joint to construct an endoscope probe [314]. The dual model catheter consisted of an angle polished ball lens fabricated from a double clad fiber, such that the size was small enough for intravascular applications. Imaging was performed in an *ex vivo* cadaveric human coronary artery with stent that contained Cy7 labeled fibrin for near infrared fluorescence imaging (NIRF). Although radial scanning was performed with this design, only the endoscope contained double clad fiber, thus the home-built rotary joint combined and separated fluorescence and OCT light using filters and dichroic mirrors.

Another multimodal endoscopic platform design similar to the system described this chapter was published using pump and signal combiner as a double clad fiber coupler[315]. The multimodal catheter employed a distal scanning mechanism with a miniature micromotor and results were demonstrated in *ex vivo* rabbit arteries with atherosclerotic plaques. The tissue was stained for 24 hours prior to imaging using Annexin V-conjugated Cy5.5 in order to target the atherosclerotic plaques. The combined fluorescence-OCT image was able to show fluorescence signal at the surface of the

plaque. Unfortunately, the imaging speed and efficiency of the pump signal combiner, high speed capability of miniature micromotor, and axial and lateral resolutions of the system were not addressed, leaving unanswered questions as to the true performance of the system.

Since these publications, the double clad fiber coupler employed in this chapter has become commercially available through Thorlabs, enabling a number of multimodal systems to be implemented by other groups. Recently multimodal needle probes for combined OCT and fluorescence imaging have been published using the commercially available double clad fiber couplers [316, 317].

8.3 *Multimodal System Design*

In this chapter, the multimodal platform described is an entirely fiber optic system with a distal end scanning, DCF-based endoscope for seamlessly integrated simultaneous OCT and fluorescence imaging.

In order to design a multimodal system that is entirely fiber optic, there are several considerations. Firstly, the imaging system needs to be able to perform multimodal imaging simultaneously without compromising image quality or interference between the two imaging modalities. In order to perform multimodal imaging simultaneously, one approach is to design a single endoscope that can be shared by both imaging modalities.

Secondly, from the system level, there must be a way to fiber optically combine and separate OCT excitation and backscattered light from fluorescence excitation and emission light. In addition to fiber optic combination and separation OCT light must be

able to maintain single-mode operation. Finally, the system design needs to be able to optimize and ensure that the signal-to-noise ratio is not compromised for OCT or fluorescence imaging. In the following sections the details of the endoscope and system design will be described.

8.3.1 System Architecture

The system schematic of the dual-modality imaging platform is shown in Figure 8.1. The system is composed of two modules, an OCT module and a fluorescence imaging module. Both modules are combined in the OCT sample arm through amultimodal endoscope and customized fiber-optic components to allow for efficient delivery and collection of OCT and fluorescence light.

The OCT engine consists of a home-built 40 kHz Fourier-domain mode-locking (FDML) fiber laser swept-source, operating at a center wavelength of 1310 with a 3dB spectral bandwidth of ~140 nm. The OCT engine includes a Mach-Zehnder interferometer (MZI) to generate a calibration signal.

The fluorescence imaging module is composed of an argon ion laser at 488 nm for excitation and a photomultiplier tube (PMT) for detection. Band-pass filters are placed in front of the PMT to filter out any residual fluorescence excitation light that may be coupled back into the detection path.

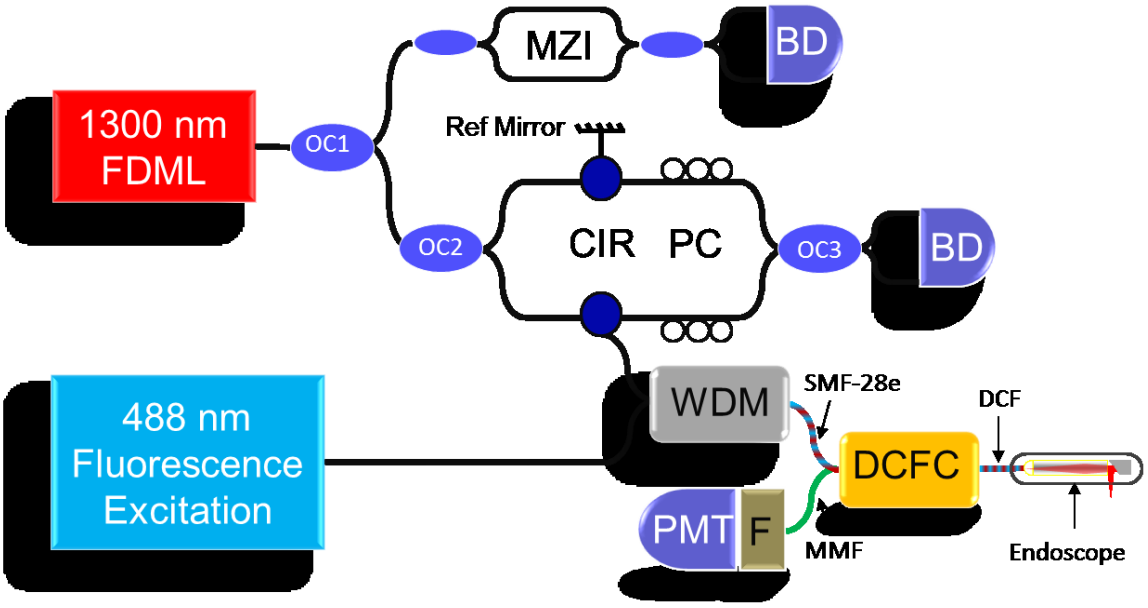

Figure 8.1: Schematic of the dual-modality system.

FDML: Fourier-domain mode-locking fiber laser; OC: Optical coupler (OC1 95/5, OC2 70/30, OC3 50/50); MZI: Mach-Zehnder interferometer; CIR: Circulator; PC: Polarization controller; BD: Balanced detector; WDM: Wavelength division multiplexer; DCFC: double-clad fiber coupler; PMT: Photomultiplier tube; F: Bandpass filter; Green: Multimode fiber (MMF); Blue/Red: Double-clad fiber (DCF); Black: Single-mode fiber (SMF-28e).

8.3.2 Endoscope Design

The first key component of this system that will be discussed is the multimodal OCT and fluorescence endoscope. There are several design challenges associated with designing a multimodal endoscope such as 1) efficient delivery of the OCT source light and fluorescence excitation light, 2) effective collection of OCT backscattered light in single

mode, 3) effective collection of fluorescence emission, and 4) implementation of a scanning mechanism with a compact footprint.

The first three challenges in regards to efficient delivery and collection of light along with maintaining a small footprint can be solved by employing a single double clad fiber based design. A customized double-clad fiber (DCF) with a 9 μm diameter core, 180 μm diameter inner cladding and 200 μm diameter outer cladding was used. The core ensures single-mode transmission for the 1300 nm OCT light while guiding fluorescence excitation in multimode. The backscattered OCT light and fluorescence emission and excitation light travel through the core and inner cladding of the DCF upon recollection. The large inner cladding allows for a high collection efficiency of fluorescence emission from the sample. Additionally, employing a single fiber design enables the overall probe diameter to be small.

The final consideration was implementation of a scanning mechanism for radial scanning. Earlier in chapter 3, the advantages and disadvantages of radial scanning proximally, with fiber optic rotary joints and distally with miniature micromotors was discussed. Several of the advantages of distal scanning included high speed and minimal non-uniform rotational distortion due to resistance in the catheter path. Among these, there are a few key advantages for distal scanning in a multimodal catheter.

Specifically, for proximal scanning a customized double clad fiber based rotary joint would be needed. Such a rotary joint would require extremely precise alignment over a full 360° rotation in order to prevent the backscattered OCT light traveling in the inner cladding of the endoscope from being coupled into the single-mode fiber in the interferometer. Any backscattered light that has traveled into the inner cladding of the

endoscope and is coupled back into the OCT interferometer would significantly comprise the OCT image quality due to having traveled multiple optical path lengths through the inner cladding (in comparison to the backscattered light in the core of the fiber). The aforementioned two reasons can be detrimental to the image quality and performance of the multimodal OCT catheter, thus this catheter design employed a distal scanning approach.

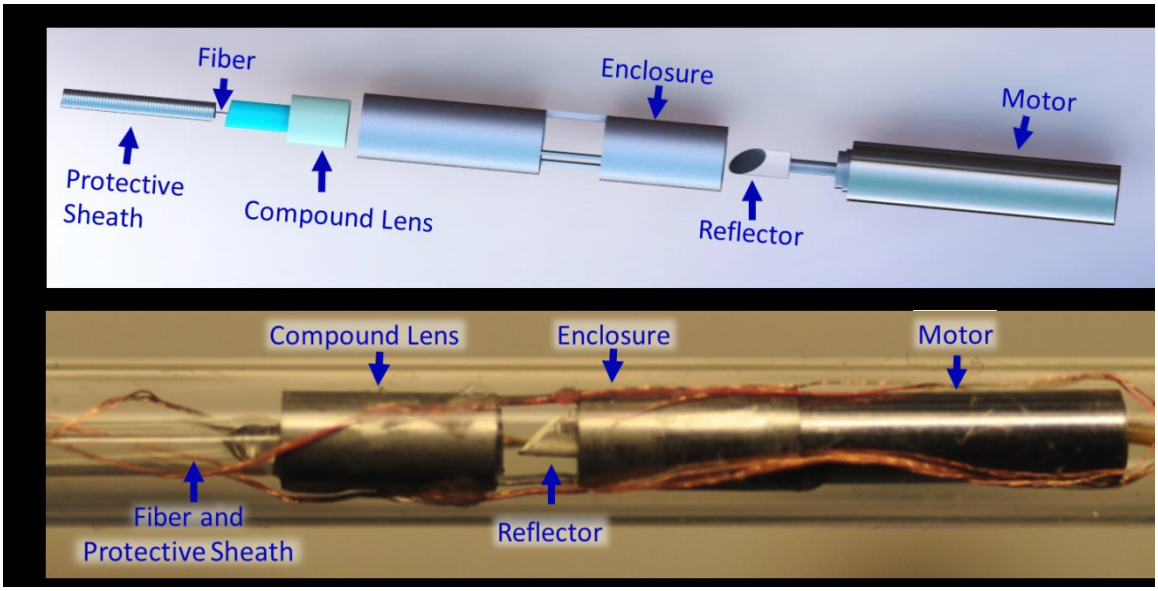

Figure 8.2: Endoscope schematic and photograph.

(A) Schematic of distal end of the dual-modal endoscope design. (B) A photograph of the constructed endoscope of an overall diameter of 2.9 mm including the housing transparent sheath.

One of the major advantages to this approach is that the imaging frame rate is dependent on the A-scan rate of the OCT system, ensuring the ability to perform high speed imaging for translational applications. Additionally, miniature micromotors are

now available as small as 900 μm in diameter enabling the catheter to be downsized from the catheter that was originally published.

The proof-of-concept catheter employed an off-the-shelf 1.9 mm diameter DC micromotor with a 45-degree rod reflector glued onto the shaft of the micromotor. Radial scanning was able to be performed when the motor was rotated.

The overall endoscope optics design is shown in Figure 8.1 A. The design employed is based on the compound lens design described in chapter 3, with a glass rod to expand the beam and a GRIN lens to focus the light, as shown in Figure 8.1 A. Since this system employs a 1300 nm swept source OCT system, no diffractive lens was employed for chromatic aberration corrections. The working distance (defined by the distance between the focal point and the enclosure) was measured to be 1.9 mm with the measured lateral resolution of ~13.7 μm.

In order to ensure that the fiber-lens assembly was aligned and centered with respect to the micromotor and rod reflector at opposite ends, a customized distal enclosure was fabricated through laser cutting. The enclosure was fabricated from a 13 gauge hypodermic tube whose inner diameter easily housed the micromotor, seen in the photograph in Figure 8.2 B. The enclosure was fabricated to have three windows separated by ultrathin metal struts (~127μm wide). The struts ensured that there was sufficient mechanical stability and the field of view blockage to the imaging beam was minimized (i.e. only 5% of the view over 360 degrees was blocked). Furthermore, the enclosure inner diameter ensured that the micromotor and rod reflector were centered with respect to the optical axis and also centered within the middle of the enclosure window to ensure that the beam was able to be deflected ~90° to image the sample.

The overall mechanical design enabled the distal end of the probe to have an overall diameter of 2.4 mm and a rigid length of 14.4 mm. The catheter was encased in a transparent protective plastic sheath with an outer diameter of 2.9 mm. Given the outer diameter of the plastic sheath, focal point was set at ~1.6 mm outside the protective sheath.

8.3.3 Combining OCT and Fluorescence Fiber Optically

The aforementioned single fiber based multimodal endoscope is able to deliver and collect light from a tissue sample as well as perform radial sampling. The next key consideration is in delivering OCT and fluorescence light to the endoscope fiber optically.

Several options for combination of the light sources exist, e.g. through free-space optics, a fiber-optic coupler, or other fiber-optic methods such as a wavelength division multiplexer (WDM). The concept of free-space coupling was quickly rejected in order to ensure the platform could be portable for use in a clinic. Furthermore this removed the need to consider optical components that could provide good coupling efficiency over a broad spectral bandwidth from fluorescence excitation at 488 to OCT wavelengths around 1300 nm. Secondly, since the OCT backscattered light will also go through the coupling device, it is critical to keep the round-trip loss low for the coupling unit, thus discounting the fiber-optical coupler.

Hence, the employed approach (see Figure 8.1) utilized an off-the-shelf fiber-optic wavelength division multiplexer (WDM) from (Thorlabs P/N WD202A2) which works for both the near infrared OCT source wavelength around 1310 nm and the visible fluorescence excitation light around 488 nm. The WDM maintained a minimal insertion

loss (i.e. -0.5 dB) for OCT as compared to free space coupling or the use of a simple fiber-optic coupler, which would result in a significant roundtrip loss of greater than 6 dB, leading to degradation of OCT detection sensitivity.

Due to the large wavelength gap between the OCT and fluorescence source wavelengths, the WDM efficiency for transmission of fluorescence excitation light (488 nm) was sub-optimal around 60%. This efficiency was sufficient for fluorescence imaging allowing 3 mW of incident power on the surface of the sample.

8.3.4 Fiber-Optic Separation of OCT Backscattered Light and Fluorescence Excitation Light

The final design challenge in this system was to be able to separate OCT backscattered light to guide it through the interferometer for detection from fluorescence emission which should be sent to the PMT for detection with minimal loss.

There are only a few options available that would allow for OCT light to be separated from fluorescence emission light effectively. Among these, the most straight-forward way is through free-space optics. Using collimators and a dichroic mirror (schematic not shown), it would be possible to recouple OCT backscattered light back to a single-mode fiber in the interferometer. However, the addition of a component within the sample arm path would introduce an extra loss thus degrading the OCT detection sensitivity. Furthermore, free space optics limits the portability and stability of the system.

Apart from this option our solution was to use a custom double clad fiber coupler (DCFC) from Lightel (P/N: 500-46712-01-1). The role of the DCFC would be to separate and guide the light in the inner cladding and the light in the core of the DCF into two

separate paths for detection. The customized DCFC consists of a single-mode fiber (SMF-28e) port, a DCF port with a standard double clad fiber from Nufern (9 μm core, 105 μm inner cladding and 125 μm outer cladding), and a multimode fiber port with a standard multimode fiber (105 μm core and 125 μm cladding), see Figure 8.1.

In the forward path (from the source to the sample), OCT source light and fluorescence excitation light have been combined into a single mode fiber through the WDM and this light will travel through the single-mode core of the double clad fiber port of the DCFC.

On the return path from the endoscope, both OCT backscattered light and fluorescence emission travel through the core and inner cladding of the double clad fiber. The light traveling in the core of the DCF is coupled back to the single-mode fiber port of the DCFC while the light traveling in the inner cladding is separated into the multimode fiber port of the DCFC. This allows the OCT backscattered light to return to the OCT module fiber optically. Once the backscattered light enters the OCT module, interference will occur and the interference pattern will finally be detected through balanced detection. No additional filters need to be used in the sample arm optics of the OCT module due to the fact that short wavelengths will not be able to propagate through the circulator employed in the sample arm, acting as a natural attenuator and filter.

Finally, fluorescence emission which travels mainly through the large inner cladding should be guided to the multimode fiber port of the DCFC. This light can be collected with a photomultiplier tube (PMT) which is equipped with band-pass filters to filter out potential leakage of the fluorescence excitation light that may have been backscattered into the fluorescence collection path.

Upon detection, both OCT and fluorescence signals were digitized, displayed and stored in computer in a synchronized fashion.

8.4 *Experimental Results*

This section will describe the experimental results obtained with this multimodal OCT and fluorescence imaging platform. *Ex vivo* tissue from a mouse tumor model was imaged in order to test the feasibility of this system. After confirming the ability of the system to perform multimodal imaging simultaneously, endoscopic imaging was performed on *ex vivo* rabbit esophagus tissue as proof-of-concept of intraluminal tissue imaging.

8.4.1 Feasibility Testing: Benchtop Imaging

Initial studies were performed on an *ex vivo* tissue sample from A431 xenograft mouse skin tumor model. A portion of the skin tumor was excised from the mouse prior to imaging. The tissue was stained using a 1.925 μM aqueous solution of acriflavine hydrochloride. Acriflavine hydrochloride was chosen as the contrast agent due to the broad excitation and emission spectra centered at ~470 nm and ~490 nm, respectively.

In order to stain the tissue sample it was submerged in the solution and incubated at 37°C for 5 minutes after which it was removed and washed with 37°C buffered saline three times (to remove excessive acriflavine). Once the tissue was thoroughly washed it was placed in a petri dish dermal side facing up for imaging.

The petri dish with tissue sample was placed on a motorized translation stage with 2 scanning axes. For preliminary imaging, the catheter was maintained in a stationary position while raster scanning was performed by the translation stage. 200 B-frames were

acquired and each frame consisted of 3072 A-scans spanning 3 mm with a pitch of 10 µm between sequential B-frames.

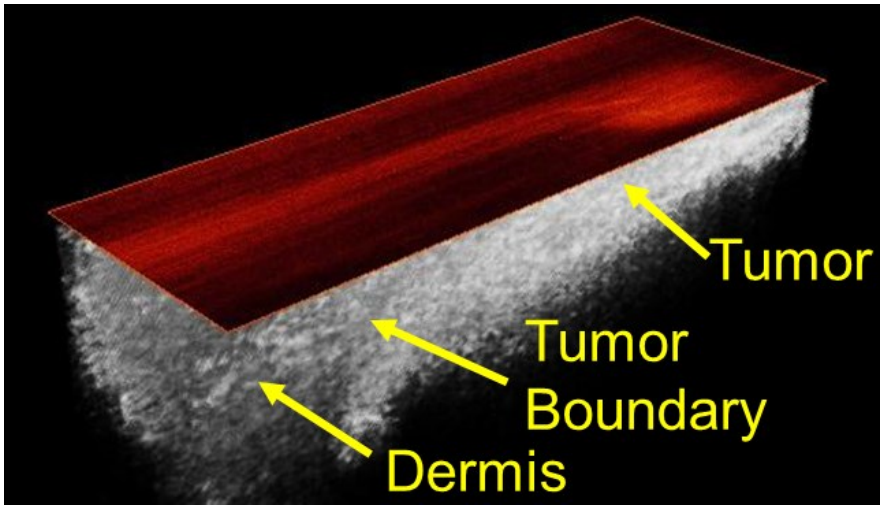

Figure 8.3: Preliminary results of multimodal imaging in mouse tumor.

Simultaneous 3D volumetric OCT (gray) and overlaid 2D fluorescence surface image (red hot colormap) of a mouse subcutaneous tumor *ex vivo*. Portion of the fluorescence surface intensity map appears to highlight the tumor region which generally has a higher density of cells and nuclei. Both OCT and fluorescence images were obtained simultaneously and were automatically co-registered.

Figure 8.3 shows the OCT volume displaced in grayscale with the corresponding 2D fluorescence map overlaid on the surface in a red hot colormap. In the OCT volume has a high backscattering region on the right where the tumor is located. This region has some localized fluorescence that can be seen on the fluorescence map with a higher intensity. The tumor region is expected to have higher fluorescence

intensity due to the increased density of cells and nuclei. Furthermore, upon closer inspection there is a light boundary between the highly scattering and low scattering regions in the OCT volume, separating the tumor from normal tissue. Since the tissue submerged in the dye solution it is possible that dye only adhered to surface areas and was not able to penetrate the full thickness of the tissue sufficiently to give a more even distribution of dye over the entire tumor region.

8.4.2 Endoscopic Imaging

The ability to image both OCT and fluorescence signals simultaneously led to further testing of this system endoscopically in a sample of *ex vivo* rabbit esophagus.

In order to demonstrate the ability for this system to be used clinically, an FDA approved fluorescence imaging contrast agent, fluorescein sodium was used in this portion of the experiment. A 300 μM solution of fluorescein sodium was prepared in advance to ensure that the sample was as fresh as possible during imaging.

After preparation of the dye, an entire segment of *ex vivo* rabbit esophagus approximately 6 cm in length was obtained. The tissue sample was stained immediately through 3 local injections, of 1-2 mL of solution, 1 cm apart along the length of the esophagus. The dye solution was injected between the lamina propria and muscularis mucosa from the submucosal side and the tissue was rinsed with buffered saline to wash away excess dye.

The tissue sample was sutured to the transparent protective plastic sheath of the endoscope in order to ensure the sample was stabilized during imaging. The suture was also able to serve as a registration landmark for OCT and fluorescence imaging.

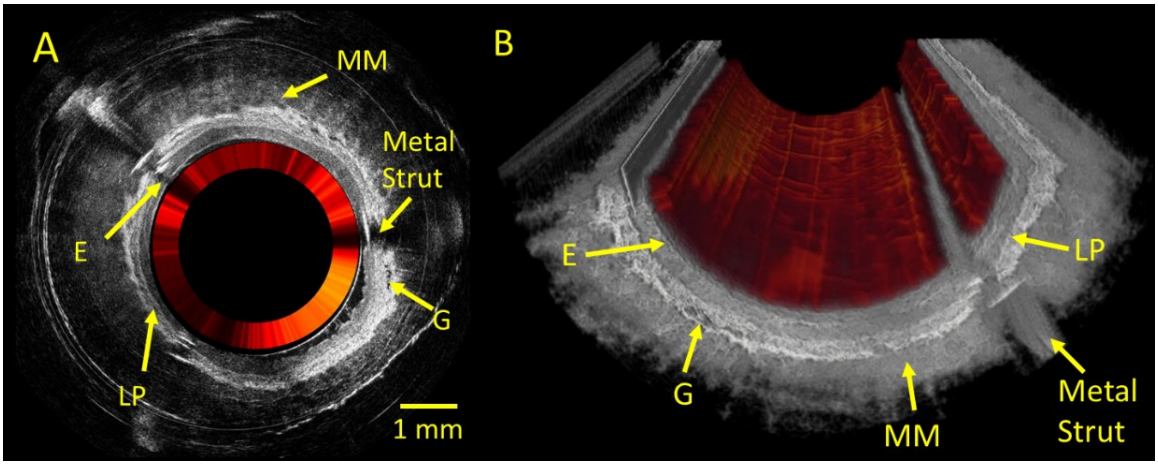

Figure 8.4 Multimodal imaging endoscopically in *ex vivo* rabbit esophagus.

Circumferential scanning and pull back were performed to obtain 3D volumetric OCT images and 2D fluorescence surface map of the esophagus with the endoscope. (A) Representative 2D cross-sectional OCT image of *ex vivo* rabbit esophagus during one circumferential scan (grayscale) with the overlaid inner annulus (red hot colormap) of the fluorescence intensity. (B) The cut-away view of the 3D OCT volumetric image (grayscale) and the 2D fluorescence intensity map inlaid (red hot colormap) on top of the OCT image. In both the 2D OCT cross-sectional image and 3D volumetric OCT image the normal layered structures of the esophagus can be clearly visualized, including the epithelium (E), lamina propria (LP), muscularis mucosa (MM), and glands (G). The co-registered and simultaneously acquired fluorescnce map shows striated structures which are believed to be vasculature [119, 138, 139].

To perform imaging, the endoscope was deployed into the esophagus. Circumferential scanning via the miniature micromotor formed cross-sectional B-frames while pull-back with a motorized translation stage enabled 3D volumetric scanning. Each OCT image frame consisted of 4096 A-lines achieving an overall frame rate of 10 frames-per-second with a pitch of 20 μm between sequential image frames, for a total pull-back length of 6 mm. The frame rate was limited by the gearhead on the off-the-shelf DC micromotor. For fluorescence imaging, 4096 points were acquired per rotation (in a synchronous fashion to OCT imaging). The volumetric scan was able to be completed within 30 second.

Figure 8.4 A is a representative cross-sectional OCT image (in grayscale) with the fluorescence signal overlaid as the colored annulus (red hot colormap). A longitudinally cutaway, volume rendered image of the pull-back scan is shown in Figure 8.4 B. In this figure, the fluorescence map is again superposed on the OCT structural volume.

Several normal esophageal structures such as epithelium, lamia propria, muscularis mucosa and glands can be visualized in the cross-sectional image and volume rendered OCT images. Additionally, there is a distribution of fluorescence intensity over the length of the esophagus.

Two remarkable features in the fluorescence map are the striated structures running along the length of the esophagus which are suspected vascular structures [150] and three signal poor regions corresponding to the metal struts of the endoscope enclosure. These features will be described further in the following section.

8.4.3 OCT-Fluorescence Correlation

With the ability to simultaneously visualize OCT and fluorescence in a volumetric data set, we wanted to ensure that the images are co-registered by correlating the structural features found the in the fluorescence map, with features in the OCT volume.

To find correlations the OCT volume was unrolled and flattened into a stack of 2D images. Figure 8.5 B-D show three representative OCT slices 700μm apart to correlate with the 2D fluorescence map shown in Figure 8.5 A. As mentioned earlier, one of the features that can be seen is the suture that was used to ensure the tissue is stable during imaging. The suture is seen as a signal poor region in the OCT and fluorescence images, as marked by the arrow in Figure 8.5 A. Additionally, striated structures that are thought to be vasculature can be seen throughout the length of the esophagus in both OCT and fluorescence images. Finally, there are three signal void regions in each of the above images, corresponding to the signal blocked by the metal struts of the enclosure. The combination of these features shows that there is significant correlation between the OCT and fluorescence map, ensuring that both images were automatically co-registered during imaging.

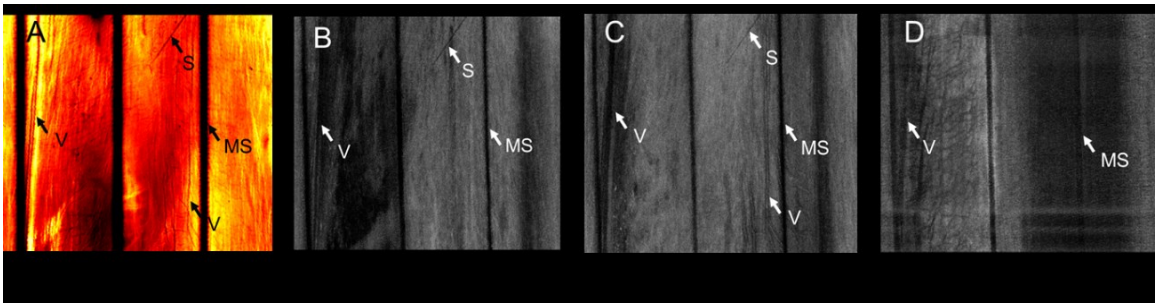

Figure 8.5: *En face* projection view of fluorescence image with depth correlated OCT images.

(A) Unwrapped 2D Fluorescence image. **(B-D)** Unwrapped OCT images at 700 µm, 1400 µm, and 2100 µm depth. The white arrows on the OCT images (B-D) correspond to the black arrows in the fluorescence map (A) indicating correlating structures such as vasculature (V), suture (S), and metal strut (MS). The suture was used to provide a registration mark for both OCT and fluorescence intensity images.

8.5 *Conclusions*

In this chapter, an entirely fiber-optic multimodal OCT and fluorescence imaging platform for endoscopic imaging has been described. The system was able to efficiently deliver and collect fluorescence excitation, fluorescence emission and OCT source light to the sample via a multimodal catheter based on a single double clad fiber.

The multimodal endoscope has a diameter 2.9 mm with a transparent protective plastic sheath which is slightly larger than the 2.8 mm accessory port of a commonly used clinical gastroscope. Current improvements in miniature micromotor technology can allow for the size of this endoscope to be reduced to nearly 60% of the current size, as

demonstrated by the ultrahigh resolution endoscope described in chapter 3 whose outer diameter (with protective plastic sheath) is only 1.78 mm.

In conjunction with the multimodal endoscope, the key components of this system, i.e. a wavelength division multiplexer and customized double clad fiber coupler, enabled all light paths to be guided fiber-optically. The OCT image quality was preserved through the system and the measured detection sensitivity of the OCT engine was ~108 dB with an A-scan rate of 40,000 A-lines-per-second.

Finally, concurrent, automatically co-registered multimodal imaging was demonstrated through preliminary studies in excised mouse tumor tissue as well as through intraluminal imaging of *ex vivo* rabbit esophagus. Several normal tissue layers were able to be visualized through intraluminal imaging of the *ex vivo* rabbit esophagus, demonstrating good OCT image quality.

Fluorescence imaging was also considered successful as it enabled visualization of structural features and landmark features demonstrated that fluorescence was co-registered with OCT. Acriflavine hydrochloride was originally employed as the exogenous contrast agent, however, the fluorescence emission intensity was suboptimal due to the suboptimal fluorescence excitation wavelength employed in this system (i.e. 488 nm as opposed to ~470 nm). Additionally, acriflavine hydrochloride is not approved for clinical use in the USA, rendering it a poor choice for comparison with clinically approved contrast agents. Hence, we employed an FDA approved dye, fluorescein sodium, for multimodal endoscopic imaging in *ex vivo* rabbit esophagus.

In conclusion, the results described in this chapter demonstrate an entirely fiber optic multimodal OCT and fluorescence imaging system with a distal scanning catheter

for intraluminal imaging. The ability to be used with an FDA approved dye and the ability to be downsized, suggest the future potential of this system for potential use in clinical applications.

Chapter 9 Conclusions

9.1 *Introduction*

This chapter concludes the description of work performed during the course of my graduate studies. In the beginning of this dissertation, I began with a brief review of the history of microscopy and engineering developments leading to the first medical endoscope. This dissertation is now written at a time 25 years after the landmark OCT in 1991[23] where *in vitro* retinal imaging and *ex vivo* imaging of human coronary artery was performed.

Over the past 25 years, OCT has demonstrated the capability to perform non-contact, real-time, high resolution imaging through benchtop and endoscopic OCT systems. In addition to morphological imaging, the field of OCT has been extended in many new directions over the past 25 years. Specifically, OCT has expanded to include polarization sensitive imaging[318, 319], full range imaging [291, 293, 294, 296, 297], blood flow imaging [271, 272, 278, 283, 284, 292], and elastography [320, 321]. Each of these extensions complements OCT imaging with unique information.

The work described in this dissertation contributes to and expands upon the growing subfield of ultrahigh resolution endoscopic OCT and will be summarized below.

9.2 *Summary of Dissertation*

The work performed in this dissertation can be categorized into two parts, engineering and subsequent biomedical imaging. The engineering portion of this dissertation was described in chapters 3 (ultrahigh resolution endoscopic imaging system)

and 4 (non-uniform rotational distortion correction) and the biomedical imaging portion was described in chapters 5 (pulmonary imaging) and 6 (colorectal cancer imaging) with an overarching goals of achieving ultrahigh resolution, endoscopic imaging of internal organs.

The last two chapters in this dissertation focus on other projects completed in the duration of graduate studies such as blood flow visualization in chapter 7 and multimodal endoscopic OCT and fluorescence imaging in chapter 8.

9.2.1 Engineering Developments

As mentioned earlier, this dissertation is written at a time 25 years after the first publication in the field of OCT. Through numerous engineering developments, spectral domain OCT was able to be implemented. Thus chapter 2 focuses on the theory of spectral domain OCT (SD-OCT) in order to lay the foundation for the work performed in this dissertation. SD-OCT is one of the two Fourier domain OCT methods where the interference signal is spectrally dispersed prior to collection with an OCT imaging spectrometer.

In general, OCT systems are made of 5 main components, the interferometer, light source, detector, sample, and reference arms. The interference signal is formed from the interference of back-reflected light from the reference arm and backscattered light from the sample with a low temporally coherent light source (i.e. broadband solid state lasers, superluminescent diode, or supercontinuum sources). In order to obtain an interference signal, the sample and reference arms must have equal optical path lengths regardless of the form of the sample arm (e.g. endoscope, hand held probe, free-space

microscope, multimodal OCT system). Path length matching must also consider dispersion usually through the addition of similar materials in both sample and reference arm, but may even consider more complex geometries such as rapid scanning optical delay lines for more precise dispersion compensation. Finally, the interference signal is to be detected with a balanced detector (swept source OCT) or in the case of this dissertation, a high resolution imaging spectrometer for OCT. The combination of the aforementioned light source, interferometer, sample and reference arm configurations, and finally detector enable imaging to be performed.

The light source governs the image contrast based on light tissue interactions (i.e. scattering and absorption) as well as the axial resolution. The interferometer, sample and reference arm configurations contribute to overall axial resolution degradation through overall spectral narrowing. The sample arm configuration determines the lateral resolution of the imaging system. Finally, the imaging spectrometer governs the calculated measurable imaging depth, sensitivity fall-off and can contribute to axial resolution broadening over the imaging depth (e.g. improper linear wavenumber calibration). Without a basic understanding of these fundamentals the progress that has been made through work performed for this dissertation would not be clear.

Moving forward these fundamentals helped to understand the decision making process for each component used to create an ultrahigh resolution, high speed endoscopic imaging system, described in chapter 3. Each component, was carefully scrutinized and optimized in order to achieve the best image quality and imaging performance. Chapter 3 laid a great emphasis on building an OCT imaging catheter at 800 nm. Only recently has

a proximal scanning catheter for 800 nm been demonstrated for volumetric imaging *in vivo* while achieving an axial resolution of 3.0 μm[78] and subsequently 2.7 μm with a broadband supercontinuum source[100]. These works served as a basis upon which a new catheter for high speed imaging could be built for ultrahigh resolution imaging. By employing a distal scanning design, speed was no longer limited by physical mechanical rotation of the catheter and high performance home-made rotary joints. Distal scanning alleviated the complicated mechanical assemblies with a small electrical device. For many years however, small micro-motors were not available smaller than 1.9 mm in diameter (1.5mm without a gear head for Micromo motor). The availability of a 900 μm DC micromotor enabled the entire catheter to be minimized to the size of a standard proximal scanning catheter (1.78 mm outer diameter with protective plastic sheath) with potential for further reduction in size. The final mechanical design assembly for the presented distal scanning catheter had been revised several times throughout the course of this dissertation. The challenges associated with fabricating a distal scanning catheter include minimizing the total field of view blockage due to wires and mechanical supports as well as minimizing the overall size.

Through careful consideration of these design features and incorporation of a customized diffractive element, an overall compact, ultrahigh resolution OCT catheter with high speed imaging capability was constructed and ready to be employed for imaging of internal organs.

A common problem with all types of OCT catheters is non-uniform rotational distortion (NURD) due to mechanical resistance in the path of proximal scanning

catheters or mechanical instability from miniature micro-motors. NURD exhibits image distortion in three main categories, translational NURD, stretch-shrink NURD, and stick-slip NURD. Due to the overwhelming similarities in ultrasound and proximal scanning OCT catheters there have been numerous papers with image processing algorithms to address translational NURD, and more recently papers to address stretch-shrink NURD. Stick-slip NURD which primarily occurs in distal scanning catheters (due to the aforementioned mechanical instability of the motors) has not been clearly discussed in the literature. Chapter 4 describes an algorithm to correct for stick-slip NURD, filling the gap in image processing algorithms for stick-slip NURD. With ever increasing A-scan rates, it is inevitable that distal scanning catheters will become more popular as alternatives to proximal scanning systems, thus the development and implementation of this algorithm will be helpful for numerous future systems with distal scanning catheters.

9.2.2 Biomedical Imaging

Equipped with a capable imaging system, it is necessary to showcase the ability and significance of performing *in vivo* imaging. In this dissertation, two biomedical imaging applications were addressed, pulmonary imaging and colorectal cancer imaging. One of the greatest advantages of this ultrahigh resolution imaging catheter is the ability to be small enough to be used in the working channel of a standard bronchoscope for small airway imaging in sheep and simultaneously be used for direct imaging of colorectal cancer in mice. The engineering efforts placed in reduction of size, increase in resolution and speed is demonstrated through the imaging results shown in chapters 5 and 6.

Chapter 5 describes the imaging results obtained from small airways *in vivo*. Chronic obstructive pulmonary diseases (COPD) are such debilitating diseases that affect a large population and understanding underlying physiological changes can help to effectively diagnose as well as develop and test therapeutic agents. For a long time visualizing small airways has been troublesome due to size constraints, however with the advent of OCT, it became possible to access and visualize small airways with depth information. This led to the ability to visualize airway wall components in a minimally invasive fashion without biopsies. In this dissertation, we employed high resolution endoscopic OCT to visualize small airways in a sheep model. Higher axial resolutions *in vivo* enabled visualization of smooth muscle with corresponding histology and a distal scanning catheter enabled high frame rate imaging up to 50 frames-per-second (limited based on the A-scan rate of the SD-OCT engine). Finally, the ability to image the same airway segment before and after ink marking shows the ability to perform volumetric airway segment registration. With these achievements, we come one step closer to proving high resolution OCT is capable of visualizing airway wall components *in vivo*.

Chapter 6 focused on longitudinal imaging of morphological changes in an ETBF induced colorectal cancer model in APC^{Min} mice. The standard technique to confirm the presence of tumors the colon has been to sacrifice the animal, fix and stain the tissue with methylene blue. This process is clearly not conducive to visualizing morphological changes as time progresses, or confirmation of tumor presence prior to tissue staining. The only alternative was endoscopic observation through a pediatric urethroscope, however excessive procedure time and trauma to the mice led to this option being unviable. Thus, the model was particularly interesting due to the fact that this was the

first time volumetric imaging could be performed with high resolution in mouse colon and due to the fact that it was performed several times over the course of eight weeks with little trauma to the mice. The ability to perform longitudinal imaging far surpassed the current capabilities of visualizing morphological changes in this model, and with quantitative assessments it would be possible to define correlated values for polyp versus healthy tissue regions.

9.2.3 Additional Projects

Finally, in addition to the main body of work composed in this dissertation, chapters 7 and 8 present two projects that are unrelated to high resolution endoscopic imaging with OCT. Chapter 7 presents an overview of blood flow visualization with some results obtained with the benchtop version of the ultrahigh resolution endoscopic OCT system, while chapter 8 presents results from a multimodal endoscopic OCT and fluorescence imaging platform.

Blood flow visualization and the ability to visualize vascular networks is of great significance for the study and understanding of physiological changes due to adverse events (e.g. stroke, tumor growth). Flow visualization was originally performed in ultrasound by taking advantage of Doppler frequency shifts from flow and beam probing geometries. The same concept was quickly adopted and implemented in the OCT field and since its adoption numerous algorithms to extract flow information from interference signals have been developed. In chapter 7, a brief review revealed that the algorithms could be categorized into phase resolved, intensity resolved, or frequency resolved methods. Taking advantage of intensity based methods such as speckle variance and

phase insensitive angiography results were demonstrated in a middle cerebral artery occlusion (MCAO) and tumor angiogenesis model. Each model provided an environment in which vascular network changes could be seen over the course of hours (MCAO) or weeks (tumor angiogenesis). These results demonstrated the capability of the ultrahigh resolution SD-OCT system to consistently measure vascular network changes.

Specifically, the MCAO model, required short term longitudinal scanning of the volume to visualize small vascular pattern changes, such as flow diversions, which were evident in the zoomed-in figures. On the other hand, tumor angiogenesis required a more global view because the overall vascular network changed as a whole in order to provide resources to the tumor. This led to changes in the surrounding regions as well and was able to be seen when compared against the vascular network pattern for a normal healthy portion of the ear. The ability to visualize localized and global changes make this a powerful and complementary addition to the information provided from structural imaging with OCT.

Finally, one of the last projects described in this dissertation was a multimodal OCT and fluorescence endoscopic OCT platform. This project represented a great step forward in the efforts to combine complementary imaging modalities for simultaneous visualization *in vivo*. The concept of multimodal imaging has been driven by the physical limitations (e.g. image contrast, depth of penetration, resolution) of each individual imaging modality. It is clear that even with the progress made by OCT to visualize structural information in high resolution and high speed, it is unable to be used for molecular imaging. Similarly, single photon fluorescence imaging is popular and widely

used for molecular targeting of specific structures, however, it lacks the ability to perform depth resolved, morphological imaging. Thus it is natural to combine these two imaging modalities to provide complementary information. The main challenge associated with combining OCT imaging with fluorescence imaging, was being able to implement it in a compact, fiber-optic, endoscopic platform.

The key to overcoming the aforementioned challenges is the use of double clad fiber and double clad fiber based components (e.g. double clad fiber coupler). Using a double clad fiber enabled us to maintain a single fiber based catheter design, allow OCT light to travel in single-mode, and enabled us to have greater collection efficiency for fluorescence emission from the large inner cladding of the fiber. Furthermore implementing a distal scanning catheter design eliminated the need to bulky home-built multimodal rotary joints, along with alleviating any cross-talk between the core and inner cladding of the double clad fiber during rotation.

Along with the catheter design, the most difficult challenge associated with ensuring this platform is entirely fiber optic, is finding a way to separate OCT backscattered light from fluorescence emission light. This was accomplished using a customized double clad fiber coupler. This singular device was designed to physically separate light from the core of the double clad fiber from light in the inner cladding of the double clad fiber, and in doing so it effectively allowed the path of OCT backscattered light to be separated from the path of the fluorescence emission light. With these key components, multimodal endoscopic imaging was demonstrated in *ex vivo* rabbit esophagus using an FDA approved imaging dye (i.e. fluorescein sodium).

In summation, OCT is an immensely powerful high resolution, non-contact, minimally invasive, real-time morphological imaging modality capable visualizing tissue microarchitecture and over the past 25 years, OCT has grown to include numerous extensions growing its potential for use in clinical applications.

References

1. Bardell, D., *The 1st Record of Microscopic Observations.* Bioscience, 1983. **33**(1): p. 36-38.
2. Masters, B.R., *History of the Optical Microscope in Cell Biology and Medicine*, in *Encyclopedia of Life Sciences (ELS)*2008, John Wiley & Sons: Chichester.
3. van den Tweel, J.G. and C.R. Taylor, *A brief history of pathology.* Virchows Archiv, 2010. **457**(1): p. 3-10.
4. Spaner, S.J. and G.L. Warnock, *A brief history of endoscopy, laparoscopy, and laparoscopic surgery.* Journal of Laparoendoscopic & Advanced Surgical Techniques-Part A, 1997. **7**(6): p. 369-373.
5. Shah, J., *Endoscopy through the ages.* Bju International, 2002. **89**(7): p. 645-652.
6. Nezhat, C. *Nezhat's History of Endoscopy*. 2005 [cited 2016; Available from: http://laparoscopy.blogs.com/endoscopyhistory/.
7. Jabbour, J.M., et al., *Confocal Endomicroscopy: Instrumentation and Medical Applications.* Annals of Biomedical Engineering, 2012. **40**(2): p. 378-397.
8. Dabbs, T. and M. Glass, *Fiberoptic Confocal Microscope - Focon.* Applied Optics, 1992. **31**(16): p. 3030-3035.
9. Dickensheets, D.L. and G.S. Kino, *Silicon-micromachined scanning confocal optical microscope.* Journal of Microelectromechanical Systems, 1998. **7**(1): p. 38-47.
10. Gmitro, A.F. and D. Aziz, *Confocal Microscopy through a Fiberoptic Imaging Bundle.* Optics Letters, 1993. **18**(8): p. 565-567.
11. Liang, C., et al., *Fiber confocal reflectance microscope (FCRM) for in-vivo imaging.* Optics express, 2001. **9**(13): p. 821-830.
12. Lane, P., A. Dlugan, and C. MacAulay, *DMD-enabled confocal microendoscopy.* Coherence Domain Optical Methods in Biomedical Science and Clinica Applications V, 2001. **4251**: p. 192-198.
13. Sung, K.B., et al., *Fiber-optic confocal reflectance microscope with miniature objective for in vivo imaging of human tissues.* Ieee Transactions on Biomedical Engineering, 2002. **49**(10): p. 1168-1172.
14. Juskaitis, R., T. Wilson, and T.F. Watson, *Real-time white light reflection confocal microscopy using a fibre-optic bundle.* Scanning, 1997. **19**(1): p. 15-19.
15. Sabharwal, Y.S., et al., *Slit-scanning confocal microendoscope for high-resolution in vivo imaging.* Applied Optics, 1999. **38**(34): p. 7133-7144.
16. Knittel, J., et al., *Endoscope-compatible confocal microscope using a gradient index-lens system.* Optics Communications, 2001. **188**(5-6): p. 267-273.
17. Bosselmann, T. and R. Ulrich, *High-Accuracy Position-Sensing with Fiber-Coupled White-Light Interferometers.* Proceedings of the Society of Photo-Optical Instrumentation Engineers, 1984. **514**: p. 361-364.
18. Danielson, B.L. and C.D. Whittenberg, *Guided-Wave Reflectometry with Micrometer Resolution.* Applied Optics, 1987. **26**(14): p. 2836-2842.
19. Takada, K., et al., *New Measurement System for Fault Location in Optical Wave-Guide Devices Based on an Interferometric-Technique.* Applied Optics, 1987. **26**(9): p. 1603-1606.

20. Youngquist, R.C., S. Carr, and D.E.N. Davies, *Optical Coherence-Domain Reflectometry - a New Optical Evaluation Technique.* Optics Letters, 1987. **12**(3): p. 158-160.
21. Macdonald, R.I., *Frequency-Domain Optical Reflectometer.* Applied Optics, 1981. **20**(10): p. 1840-1844.
22. Kingsley, S.A. and D.E.N. Davies, *Ofdr Diagnostics for Fiber and Integrated-Optic Systems.* Electronics Letters, 1985. **21**(10): p. 434-435.
23. Huang, D., et al., *Optical Coherence Tomography.* Science, 1991. **254**(5035): p. 1178-1181.
24. Hausler, G. and J. Neumann. *Coherence radar- an accurate 3-D sensor for rough surfaces*. in *SPIE* 1992.
25. Dresel, T., G. Hausler, and H. Venzke, *3-Dimensional Sensing of Rough Surfaces by Coherence Radar.* Applied Optics, 1992. **31**(7): p. 919-925.
26. Fercher, A.F., et al., *Measurement of Optical Distances by Optical-Spectrum Modulation.* Proceedings of Microscopy, Holography, and Interferometry in Biomedicine, 1994. **2083**: p. 263-267.
27. Fercher, A.F., et al., *Measurement of Intraocular Distances by Backscattering Spectral Interferometry.* Optics Communications, 1995. **117**(1-2): p. 43-48.
28. Bail, M., et al., *Coherence tomography with the "Spectral Radar" - Fast optical analysis in volume scatterers by short coherence interferometry.* Photon Propagation in Tissues Ii, Proceedings Of, 1996. **2925**: p. 298-303.
29. Hausler, G. and M.W. Lindner, *"Coherence Radar" and "Spectral Radar"-New Tools for Dermatological Diagnosis.* Journal of Biomedical Optics, 1998. **3**(1): p. 21-31.
30. Potsaid, B., et al., *Ultrahigh speed Spectral/Fourier domain OCT ophthalmic imaging at 70,000 to 312,500 axial scans per second.* Optics express, 2008. **16**(19): p. 15149-15169.
31. An, L., et al., *High speed spectral domain optical coherence tomography for retinal imaging at 500,000 A-lines per second.* Biomedical Optics Express, 2011. **2**(10): p. 2770-2783.
32. An, L., et al., *High-resolution 1050 nm spectral domain retinal optical coherence tomography at 120 kHz A-scan rate with 6.1 mm imaging depth.* Biomedical Optics Express, 2013. **4**(2): p. 245-59.
33. Lee, S.W., et al., *Optimization for Axial Resolution, Depth Range, and Sensitivity of Spectral Domain Optical Coherence Tomography at 1.3 microm.* The journal of the Korean Physical Society, 2009. **55**(6): p. 2354-2360.
34. Sorin, W.V., et al., *Coherent Fmcw Reflectometry Using a Temperature Tuned Nd-Yag Ring Laser.* Ieee Photonics Technology Letters, 1990. **2**(12): p. 902-904.
35. Passy, R., et al., *Experimental and Theoretical Investigations of Coherent Ofdr with Semiconductor-Laser Sources.* Journal of Lightwave Technology, 1994. **12**(9): p. 1622-1630.
36. Chinn, S.R., E.A. Swanson, and J.G. Fujimoto, *Optical coherence tomography using a frequency-tunable optical source.* Optics Letters, 1997. **22**(5): p. 340-342.
37. Golubovic, B., et al., *Optical frequency-domain reflectometry using rapid wavelength tuning of a Cr4+:forsterite laser.* Optics Letters, 1997. **22**(22): p. 1704-1706.

38. Haberland, U.H.P., V. Blazek, and H.J. Schmitt, *Chirp Optical Coherence Tomography of Layered Scattering Media.* Journal of Biomedical Optics, 1998. **3**(3): p. 259-266.
39. Lim, H., et al., *Optical frequency domain imaging with a rapidly swept laser in the 815-870 nm range.* Optics express, 2006. **14**(13): p. 5937-5944.
40. Srinivasan, V.J., et al., *High-speed, high-resolution optical coherence tomography retinal imaging with a frequency-swept laser at 850 nm.* Optics Letters, 2007. **32**(4): p. 361-363.
41. Lee, S.W., C.S. Kim, and B.M. Kim, *External line-cavity wavelength-swept source at 850 nm for optical coherence tomography.* Ieee Photonics Technology Letters, 2007. **19**(2-4): p. 176-178.
42. Huber, R., et al., *Fourier domain mode locking at 1050 nm for ultra-high-speed optical coherence tomography of the human retina at 236,000 axial scans per second.* Optics Letters, 2007. **32**(14): p. 2049-2051.
43. Potsaid, B., et al., *Ultrahigh speed 1050nm swept source / Fourier domain OCT retinal and anterior segment imaging at 100,000 to 400,000 axial scans per second.* Optics Express, 2010. **18**(19): p. 20029-20048.
44. Wieser, W., et al., *Multi-Megahertz OCT: High quality 3D imaging at 20 million A-scans and 4.5 GVoxels per second.* Optics express, 2010. **18**(14): p. 14685-14704.
45. Jayaraman, V., et al., *OCT Imaging up to 760 kHz Axial Scan Rate Using Single-Mode 1310nm MEMS-Tunable VCSELs with > 100nm Tuning Range.* 2011 Conference on Lasers and Electro-Optics (Cleo), 2011.
46. Potsaid, B., et al., *MEMS tunable VCSEL light source for ultrahigh speed 60kHz-1MHz axial scan rate and long range centimeter class OCT imaging.* Optical Coherence Tomography and Coherence Domain Optical Methods in Biomedicine Xvi, 2012. **8213**.
47. Huber, R., D.C. Adler, and J.G. Fujimoto, *Buffered Fourier domain mode locking: unidirectional swept laser sources for optical coherence tomography imaging at 370,000 lines/s.* Optics Letters, 2006. **31**(20): p. 2975-2977.
48. Herz, P.R., et al., *Micromotor endoscope catheter for in vivo, ultrahigh-resolution optical coherence tomography.* Optics Letters, 2004. **29**(19): p. 2261-2263.
49. Li, J.A., et al., *High speed miniature motorized endoscopic probe for 3D Optical Frequency Domain Imaging.* Optical Coherence Tomography and Coherence Domain Optical Methods in Biomedicine Xvii, 2013. **8571**.
50. Wang, T.S., et al., *Intravascular optical coherence tomography imaging at 3200 frames per second.* Optics Letters, 2013. **38**(10): p. 1715-1717.
51. Cho, H.S., et al., *High frame-rate intravascular optical frequency-domain imaging in vivo.* Biomedical Optics Express, 2014. **5**(1): p. 223-232.
52. Izatt, J.A., et al., *Micrometer-scale resolution imaging of the anterior eye in vivo with optical coherence tomography.* Arch Ophthalmol, 1994. **112**(12): p. 1584-9.
53. Drexler, W., et al., *Invivo Optical Coherence Tomography and Topography of the Fundus of the Human Eye.* Lasers in Ophthalmology Ii, Proceedings Of, 1995. **2330**: p. 134-145.
54. Drexler, W., et al., *Measurement of the Thickness of Fundus Layers by Partial Coherence Tomography.* Optical Engineering, 1995. **34**(3): p. 701-710.

55. Radhakrishnan, S., et al., *Real-time optical coherence tomography of the anterior segment at 1310 nm.* Arch Ophthalmol, 2001. **119**(8): p. 1179-85.
56. Hee, M.R., et al., *Optical Coherence Tomography of the Human Retina.* Archives of Ophthalmology, 1995. **113**(3): p. 325-332.
57. Cobb, M.J., et al., *Noninvasive assessment of cutaneous wound healing using ultrahigh-resolution optical coherence tomography.* Journal of Biomedical Optics, 2006. **11**(6): p. 064002.
58. Konig, K., et al., *Clinical optical coherence tomography combined with multiphoton tomography of patients with skin diseases.* J Biophotonics, 2009. **2**(6-7): p. 389-97.
59. Tearney, G.J., et al., *Scanning single-mode fiber optic catheter-endoscope for optical coherence tomography.* Optics Letters, 1996. **21**(7): p. 543-545.
60. Jang, I.K., et al., *In vivo characterization of coronary atherosclerotic plaque by use of optical coherence tomography.* Circulation, 2005. **111**(12): p. 1551-1555.
61. Kawasaki, M., et al., *Diagnostic accuracy of optical coherence tomography and integrated backscatter intravascular ultrasound images for tissue characterization of human coronary plaques.* Journal of the American College of Cardiology, 2006. **48**(1): p. 81-88.
62. Bouma, B.E., et al., *Evaluation of intracoronary stenting by intravascular optical coherence tomography.* Heart, 2003. **89**(3): p. 317-320.
63. Coxson, H.O., et al., *Airway wall thickness assessed using computed tomography and optical coherence tomography.* American Journal of Respiratory and Critical Care Medicine, 2008. **177**(11): p. 1201-1206.
64. Hanna, N., et al., *Two-dimensonal and 3-dimensional optical coherence tomographic imaging of the airway, lung, and pleura.* Journal of Thoracic and Cardiovascular Surgery, 2005. **129**(3): p. 615-622.
65. Ell, C., et al., *Endoscopic mucosal resection of early cancer and high-grade dysplasia in Barrett's esophagus.* Gastroenterology, 2000. **118**(4): p. 670-677.
66. Cobb, M.J., et al., *Imaging of subsquamous Barrett's epithelium with ultrahigh-resolution optical coherence tomography: a histologic correlation study.* Gastrointestinal endoscopy, 2010. **71**(2): p. 223-230.
67. Caygill, C.P.J., et al., *Barrett's esophagus: surveillance and reversal.* Barrett's Esophagus: The 10th Oeso World Congress Proceedings, 2011. **1232**: p. 196-209.
68. Sivak, M.V., et al., *High-resolution endoscopic imaging of the GI tract using optical coherence tomography.* Gastrointestinal endoscopy, 2000. **51**(4): p. 474-479.
69. Jackle, S., et al., *In vivo endoscopic optical coherence tomography of the human gastrointestinal tract - Toward optical biopsy.* Endoscopy, 2000. **32**(10): p. 743-749.
70. Pfau, P.R., et al., *Criteria for the diagnosis of dysplasia by endoscopic optical coherence tomography.* Gastrointestinal endoscopy, 2003. **58**(2): p. 196-202.
71. Shen, B., et al., *In Vivo Colonoscopic Optical Coherence Tomography for Transmural Inflammation in Inflammatory Bowel Disease.* Clinical Gastroenterology and Hepatology, 2004. **2**(12): p. 1080-1087.

72. Shen, B., et al., *Ex Vivo Histology-Correlated Optical Coherence Tomography in the Detection of Transmural Inflammation in Crohn's Disease.* Clinical Gastroenterology and Hepatology, 2004. **2**(9): p. 754-760.
73. Familiari, L., et al., *Optical coherence tomography evaluation of ulcerative colitis: The patterns and the comparison with histology.* American Journal of Gastroenterology, 2006. **101**(12): p. 2833-2840.
74. Drexler, W., et al., *In vivo ultrahigh-resolution optical coherence tomography.* Optics Letters, 1999. **24**(17): p. 1221-3.
75. Hartl, I., et al., *Ultrahigh-resolution optical coherence tomography using continuum generation in an air-silica microstructure optical fiber.* Optics Letters, 2001. **26**(9): p. 608-610.
76. Tumlinson, A.R., et al., *Endoscope-tip interferometer for ultrahigh resolution frequency domain optical coherence tomography in mouse colon.* Optics express, 2006. **14**(5): p. 1878-1887.
77. Tumlinson, A.R., et al., *In vivo ultrahigh-resolution optical coherence tomography of mouse colon with an achromatized endoscope.* Journal of Biomedical Optics, 2006. **11**(6): p. 064003.
78. Xi, J.F., et al., *Diffractive catheter for ultrahigh-resolution spectral-domain volumetric OCT imaging.* Optics Letters, 2014. **39**(7): p. 2016-2019.
79. Tuchin, V.V., *Tissue optics light scattering methods and instruments for medical diagnosis*, in *SPIE Press monograph PM166*2007, SPIE: Bellingham, Wash. (1000 20th St. Bellingham WA 98225-6705 USA). p. 1 online resource (xl, 840 p.
80. Tuchin, V.V., *Light Interaction with Biological Tissues (Overview).* Proceedings of Static and Dynamic Light Scattering in Medicine and Biology, 1993. **1884**: p. 234-272.
81. Wang, L.V. and H.-i. Wu, *Biomedical optics : principles and imaging*2007, Hoboken, N.J.: Wiley-Interscience. xiv, 362 pages.
82. Bohren, C.F. and D.R. Huffman, *Absorption and scattering of light by small particles*, in *Wiley science paperback series*1998, Wiley: New York. p. 1 online resource (xiv, 530 p.).
83. Schmitt, J.M., A. Knuttel, and R.F. Bonner, *Measurement of Optical-Properties of Biological Tissues by Low-Coherence Reflectometry.* Applied Optics, 1993. **32**(30): p. 6032-6042.
84. Liang, W.X., J. Mavadia, and X.D. Li, *Optical Coherence Tomography.* Diagnostic Endoscopy, 2014: p. 135-170.
85. Tripathi, R., et al., *Spectral shaping for non-Gaussian source spectra in optical coherence tomography.* Optics Letters, 2002. **27**(6): p. 406-408.
86. Akcay, A.C., J.P. Rolland, and J.M. Eichenholz, *Spectral shaping to improve the point spread function in optical coherence tomography.* Optics Letters, 2003. **28**(20): p. 1921-1923.
87. Wojtkowski, M., et al., *Ultrahigh-resolution, high-speed, Fourier domain optical coherence tomography and methods for dispersion compensation.* Optics express, 2004. **12**(11): p. 2404-2422.
88. Lippok, N., et al., *Dispersion compensation in Fourier domain optical coherence tomography using the fractional Fourier transform.* Optics express, 2012. **20**(21): p. 23398-23413.

89. Wang, Y., et al., *Dispersion compensation for FD-OCT using spectrum reconstruction.* Journal of X-Ray Science and Technology, 2015. **23**(5): p. 639-646.
90. Fercher, A.F., et al., *Numerical dispersion compensation for Partial Coherence Interferometry and Optical Coherence Tomography.* Optics express, 2001. **9**(12): p. 610-615.
91. Bouma, B.E. and G.J. Tearney, *Handbook of optical coherence tomography*2002, New York: Marcel Dekker. x, 741 p.
92. Shidlovski, V. and J. Wei, *Superluminescent diodes for optical coherence tomography.* Test and Measurement Applications of Optoelectronic Devices, 2002. **4648**: p. 139-147.
93. Carl Zeiss Meditec, I., *CIRRUS HD-OCT 4000 and 400*, 2015, Carl Zeiss Meditec, Inc.: USA.
94. Carl Zeiss Meditec, I., *CIRRUS HD-OCT 5000 and 500*, 2012, Carl Zeiss Meditec, Inc.: USA.
95. Company, B.I.-a.L.M., *Envisu SDOCT Product Specifications*, Bioptigen Inc. - a Leica Microsysems Company: USA.
96. Bouma, B., et al., *High-Resolution Optical Coherence Tomographic Imaging Using a Mode-Locked Ti-Al2o3 Laser Source.* Optics Letters, 1995. **20**(13): p. 1486-1488.
97. Drexler, W., et al., *In vivo ultrahigh-resolution optical coherence tomography.* Optics Letters, 1999. **24**(17): p. 1221-1223.
98. Bouma, B.E., et al., *Self-phase-modulated Kerr-lens mode-locked Cr:forsterite laser source for optical coherence tomography.* Optics Letters, 1996. **21**(22): p. 1839-1841.
99. Wang, D.L., et al., *Super-achromatic rapid scanning microendoscope for ultrahigh-resolution OCT imaging.* Ieee Journal of Selected Topics in Quantum Electronics, 2007. **13**(6): p. 1596-1601.
100. Yuan, W., et al., *Optimal operational conditions for supercontinuum-based ultrahigh-resolution endoscopic OCT imaging.* Optics Letters, 2016. **41**(2): p. 250-253.
101. Hee, M.R., et al., *Femtosecond Transillumination Optical Coherence Tomography.* Optics Letters, 1993. **18**(12): p. 950-952.
102. Bouma, B.E. and G.J. Tearney, *Power-efficient nonreciprocal interferometer and linear-scanning fiber-optic catheter for optical coherence tomography.* Optics Letters, 1999. **24**(8): p. 531-533.
103. Rollins, A.M. and J.A. Izatt, *Optimal interferometer designs for optical coherence tomography.* Optics Letters, 1999. **24**(21): p. 1484-1486.
104. Dubois, A., et al., *High-resolution full-field optical coherence tomography with a Linnik microscope.* Applied Optics, 2002. **41**(4): p. 805-812.
105. Dubois, A., et al., *Ultrahigh-resolution full-field optical coherence tomography.* Applied Optics, 2004. **43**(14): p. 2874-2883.
106. Kuo, W.C., et al., *Balanced detection for spectral domain optical coherence tomography.* Optics express, 2013. **21**(16): p. 19280-19291.
107. Yun, S.H., et al., *High-speed spectral-domain optical coherence tomography at 1.3 mu m wavelength.* Optics express, 2003. **11**(26): p. 3598-3604.

108. Nassif, N.A., et al., *In vivo high-resolution video-rate spectral-domain optical coherence tomography of the human retina and optic nerve.* Optics express, 2004. **12**(3): p. 367-376.
109. Nassif, N., et al., *In vivo human retinal imaging by ultrahigh-speed spectral domain optical coherence tomography.* Optics Letters, 2004. **29**(5): p. 480-482.
110. Chan, K.K.H. and S. Tang, *High-speed spectral domain optical coherence tomography using non-uniform fast Fourier transform.* Biomedical Optics Express, 2010. **1**(5): p. 1309-1319.
111. Wang, K., et al., *Development of a non-uniform discrete Fourier transform based high speed spectral domain optical coherence tomography system.* Optics express, 2009. **17**(14): p. 12121-12131.
112. Traub, W.A., *Constant-Dispersion Grism Spectrometer for Channeled Spectra.* Journal of the Optical Society of America a-Optics Image Science and Vision, 1990. **7**(9): p. 1779-1791.
113. Hu, Z. and A.M. Rollins, *Fourier domain optical coherence tomography with a linear-in-wavenumber spectrometer.* Optics Letters, 2007. **32**(24): p. 3525-3527.
114. Wojtkowski, M., et al., *In vivo human retinal imaging by Fourier domain optical coherence tomography.* Journal of Biomedical Optics, 2002. **7**(3): p. 457-463.
115. Gelikonov, V.M., G.V. Gelikonov, and P.A. Shilyagin, *Linear-wavenumber spectrometer for high-speed spectral-domain optical coherence tomography.* Optics and Spectroscopy, 2009. **106**(3): p. 459-465.
116. Liu, X., et al., *Rapid-scanning forward-imaging miniature endoscope for real-time optical coherence tomography.* Opt. Lett., 2004. **29**(15): p. 1763-1765.
117. Yang, V.X.D., et al., *Interstitial Doppler optical coherence tomography.* Optics Letters, 2005. **30**(14): p. 1791-1793.
118. Li, X.D., T.H. Ko, and J.G. Fujimoto, *Intraluminal fiber-optic Doppler imaging catheter for structural and functional coherence tomography.* Optics Letters, 2001. **26**(23): p. 1906-1908.
119. Wu, Y.C., et al., *Robust High-Resolution Fine OCT Needle for Side-Viewing Interstitial Tissue Imaging.* Ieee Journal of Selected Topics in Quantum Electronics, 2010. **16**(4): p. 863-869.
120. Zuccaro, G., et al., *Optical coherence tomography of the esophagus and proximal stomach in health and disease.* American Journal of Gastroenterology, 2001. **96**(9): p. 2633-2639.
121. Pan, Y., H. Xie, and G.K. Fedder, *Endoscopic optical coherence tomography based on a microelectromechanical mirror.* Opt Lett, 2001. **26**(24): p. 1966-8.
122. Wang, Z.G., et al., *In vivo bladder imaging with microelectromechanical systems-based endoscopic spectral domain optical coherence tomography.* Journal of Biomedical Optics, 2007. **12**(3).
123. Huo, L., et al., *Forward-viewing resonant fiber-optic scanning endoscope of appropriate scanning speed for 3D OCT imaging.* Optics Express, 2010. **18**(14): p. 14375-14384.
124. Zara, J.M., et al., *Electrostatic micromachine scanning mirror for optical coherence tomography.* Opt Lett, 2003. **28**(8): p. 628-30.

125. Jung, W., et al., *Three-dimensional endoscopic optical coherence tomography by use of a two-axis microelectromechanical scanning mirror.* Applied Physics Letters, 2006. **88**(16).
126. Aguirre, A.D., et al., *Two-axis MEMS scanning catheter for ultrahigh resolution three-dimensional and en face imaging.* Optics express, 2007. **15**(5): p. 2445-2453.
127. Kim, K.H., et al., *Two-axis magnetically-driven MEMS scanning catheter for endoscopic high-speed optical coherence tomography.* Optics express, 2007. **15**(26): p. 18130-18140.
128. Jang, I.K., et al., *Visualization of coronary atherosclerotic plaques in patients using optical coherence tomography: comparison with intravascular ultrasound.* Journal of American College of Cardiology, 2002. **39**(4): p. 604-9.
129. Wang, T.S., et al., *Heartbeat OCT: in vivo intravascular megahertz-optical coherence tomography.* Biomedical Optics Express, 2015. **6**(12): p. 5021-5032.
130. Tsai, T.H., et al., *Ultrahigh speed endoscopic optical coherence tomography for gastroenterology.* Biomedical Optics Express, 2014. **5**(12): p. 4387-4404.
131. Armstrong, J.J., et al., *Quantitative upper airway imaging with anatomic optical coherence tomography.* American Journal of Respiratory and Critical Care Medicine, 2006. **173**(2): p. 226-233.
132. McLaughlin, R.A., et al., *Imaging of Breast Cancer With Optical Coherence Tomography Needle Probes: Feasibility and Initial Results.* Ieee Journal of Selected Topics in Quantum Electronics, 2012. **18**(3): p. 1184-1191.
133. Curatolo, A., et al., *Ultrasound-Guided Optical Coherence Tomography Needle Probe for the Assessment of Breast Cancer Tumor Margins.* American Journal of Roentgenology, 2012. **199**(4): p. W520-W522.
134. Hwang, J.H., et al., *Optical coherence tomography imaging of the pancreas: a needle-based approach.* Clinical gastroenterology and hepatology : the official clinical practice journal of the American Gastroenterological Association, 2005. **3**(7 Suppl 1): p. S49-52.
135. Lorenser, D., et al., *Ultrathin side-viewing needle probe for optical coherence tomography.* Optics Letters, 2011. **36**(19): p. 3894-3896.
136. Quirk, B.C., et al., *In situ imaging of lung alveoli with an optical coherence tomography needle probe.* Journal of Biomedical Optics, 2011. **16**(3).
137. McLaughlin, R.A., et al., *Static and dynamic imaging of alveoli using optical coherence tomography needle probes.* Journal of Applied Physiology, 2012. **113**(6): p. 967-974.
138. Fu, H.L., et al., *Flexible miniature compound lens design for high-resolution optical coherence tomography balloon imaging catheter.* Journal of Biomedical Optics, 2008. **13**(6): p. 060502-060502-3.
139. Xi, J.F., et al., *High-resolution OCT balloon imaging catheter with astigmatism correction.* Optics Letters, 2009. **34**(13): p. 1943-1945.
140. Kowalevicz, A., et al., *Ultrahigh resolution optical coherence tomography using a superluminescent light source.* Optics express, 2002. **10**(7): p. 349-53.
141. Tran, P.H., et al., *In vivo endoscopic optical coherence tomography by use of a rotational microelectromechanical system probe.* Optics Letters, 2004. **29**(11): p. 1236-1238.

142. Herz, P.R., et al., *Micromotor endoscope catheter for in vivo, ultrahigh-resolution optical coherence tomography.* Optics Letters, 2004. **29**(19): p. 2261-3.
143. Tsai, T.H., et al., *Ultrahigh speed endoscopic optical coherence tomography using micromotor imaging catheter and VCSEL technology.* Biomedical Optics Express, 2013. **4**(7): p. 1119-1132.
144. Li, J.A., et al., *High speed miniature motorized endoscopic probe for optical frequency domain imaging.* Optics express, 2012. **20**(22): p. 24132-24138.
145. Mavadia, J., et al., *An all-fiber-optic endoscopy platform for simultaneous OCT and fluorescence imaging.* Biomedical Optics Express, 2012. **3**(11): p. 2851-2859.
146. Mavadia-Shukla, J., et al. *In vivo Airway Imaging with High-speed Ultrahigh resolution Endoscopic OCT*. in *Biomedical Optics Congress 2016*. 2016. Hollywood, FL: OSA.
147. KG, O.E.S.C., *Solutions for Bronchoscopy*, 2014, Olympus Europa SE & CO. KG: Hamburg, Germany.
148. INC., O.A., *190-Series Colonoscopes*, 2014, Olympus America INC.: U.S.A.
149. Li, X.D., et al., *Imaging needle for optical coherence tomography.* Optics Letters, 2000. **25**(20): p. 1520-1522.
150. Tearney, G.J., et al., *In vivo endoscopic optical biopsy with optical coherence tomography.* Science, 1997. **276**(5321): p. 2037-2039.
151. O'Shea, D.C. and Society of Photo-optical Instrumentation Engineers., *Diffractive optics design, fabrication, and test*, in *Tutorial texts in optical engineering v TT 62*2004, SPIE: Bellingham, Wash. (1000 20th St. Bellingham WA 98225-6705 USA). p. 1 online resource (xii, 241 p.
152. Leitgeb, R., C.K. Hitzenberger, and A.F. Fercher, *Performance of fourier domain vs. time domain optical coherence tomography.* Optics express, 2003. **11**(8): p. 889-894.
153. A/S, N.P., *SuperK EXTREME: High Power Supercontinuum fiber laser series*, NKT Photonics A/S: USA.
154. A/S, N.P., *SuperK SPLIT: Spectral splitting filter for SuperK supercontinuum lasers*, NKT Photonics A?S: USA.
155. AG, E., *Exalos 840nm Swpet Sources*, Exalos AG: Schlieren, Switzerland.
156. Lee, S.W., et al., *Fourier Domain Optical Coherence Tomography for Retinal Imaging with 800-nm Swept Source: Real-time Resampling in k-domain.* Journal of the Optical Society of Korea, 2011. **15**(3): p. 293-299.
157. Goda, K., et al., *High-throughput optical coherence tomography at 800 nm.* Optics express, 2012. **20**(18): p. 19612-19617.
158. Cho, J., G. Gulsen, and C.S. Kim, *800-nm-centered swept laser for spectroscopic optical coherence tomography.* Laser Physics, 2014. **24**(4).
159. Shirazi, M.F., M. Jeon, and J. Kim, *850 nm centered wavelength-swept laser based on a wavelength selection galvo filter.* Chinese Optics Letters, 2016. **14**(1).
160. An, L., et al., *High-resolution 1050 nm spectral domain retinal optical coherence tomography at 120 kHz A-scan rate with 6.1 mm imaging depth.* Biomedical Optics Express, 2013. **4**(2): p. 245-259.
161. An, L., G.Y. Guan, and R.K.K. Wang, *High-speed 1310 nm-band spectral domain optical coherence tomography at 184,000 lines per second.* Journal of Biomedical Optics, 2011. **16**(6).

162. van Soest, G., J.G. Bosch, and A.F.W. van der Steen, *Azimuthal registration of image sequences affected by nonuniform rotation distortion.* Ieee Transactions on Information Technology in Biomedicine, 2008. **12**(3): p. 348-355.
163. Kang, W., et al., *Motion artifacts associated with in vivo endoscopic OCT images of the esophagus.* Optics express, 2011. **19**(21): p. 20722-20735.
164. Ughi, G.J., et al., *Automatic three-dimensional registration of intravascular optical coherence tomography images.* Journal of Biomedical Optics, 2012. **17**(2).
165. Gatta, C., et al., *Fast Rigid Registration of Vascular Structures in IVUS Sequences.* Ieee Transactions on Information Technology in Biomedicine, 2009. **13**(6): p. 1006-1011.
166. Yin, J.C., et al., *In vivo early detection of smoke-induced airway injury using three-dimensional swept-source optical coherence tomography.* Journal of Biomedical Optics, 2009. **14**(6).
167. Shi, Y., et al., *Motion artifact reduction for IVUS-based thermal strain imaging.* Ieee Transactions on Ultrasonics Ferroelectrics and Frequency Control, 2005. **52**(8): p. 1312-1319.
168. Sun, C., et al., *In vivo feasibility of endovascular Doppler optical coherence tomography.* Biomedical Optics Express, 2012. **3**(10): p. 2600-10.
169. ten Hoff, H., et al., *Imaging artifacts in mechanically driven ultrasound catheters.* International journal of cardiac imaging, 1989. **4**(2-4): p. 195-9.
170. Kimura, B.J., et al., *Distortion of intravascular ultrasound images because of nonuniform angular velocity of mechanical-type transducers.* American Heart Journal, 1996. **132**(2): p. 328-336.
171. Kearney, P.P., et al., *A study of the quantitative and qualitative impact of catheter shaft angulation in a mechanical intravascular ultrasound system.* Ultrasound in Medicine and Biology, 1997. **23**(1): p. 87-93.
172. Ahsen, O.O., et al., *Correction of rotational distortion for catheter-based en face OCT and OCT angiography.* Optics Letters, 2014. **39**(20): p. 5973-5976.
173. Sherwood, L., *Human physiology : from cells to systems*. 3rd ed1997, Belmont, CA: Wadsworth Pub. Co. 1 v. (various pagings).
174. Hogg, J.C., P.T. Macklem, and Thurlbec.Wm, *Site and Nature of Airway Obstruction in Chronic Obstructive Lung Disease.* New England Journal of Medicine, 1968. **278**(25): p. 1355-&.
175. Jones, R.L., et al., *Airway remodelling in COPD: It's not asthma!* Respirology, 2016. **21**(8): p. 1347-1356.
176. Jeffery, P.K., *Structural and inflammatory changes in COPD: a comparison with asthma.* Thorax, 1998. **53**(2): p. 129-136.
177. Hogg, J.C., et al., *The nature of small-airway obstruction in chronic obstructive pulmonary disease.* New England Journal of Medicine, 2004. **350**(26): p. 2645-2653.
178. Marieb, E.N., *Human anatomy & physiology*. 5th ed2001, San Francisco: Benjamin Cummings. xxii, 1249 p.
179. Vestbo, J., et al., *Global Strategy for the Diagnosis, Management, and Prevention of Chronic Obstructive Pulmonary Disease GOLD Executive Summary.* American Journal of Respiratory and Critical Care Medicine, 2013. **187**(4): p. 347-365.

180. Jeffery, P.K., *Structural and inflammatory changes in COPD: a comparison with asthma.* Thorax, 1998. **53**(2): p. 129-36.
181. Saetta, M., et al., *Loss of Alveolar Attachments in Smokers - a Morphometric Correlate of Lung-Function Impairment.* American Review of Respiratory Disease, 1985. **132**(4): p. 894-900.
182. Scichilone, N., et al., *The airway response to deep inspirations decreases with COPD severity and is associated with airway distensibility assessed by computed tomography.* Journal of Applied Physiology, 2008. **105**(3): p. 832-838.
183. Rennard, S.I., *Overview of causes of COPD. New understanding of pathogenesis and mechanisms can guide future therapy.* Postgraduate medicine, 2002. **111**(6): p. 28-30, 33-4, 37-8.
184. Peacock, J.L., et al., *Outdoor air pollution and respiratory health in patients with COPD.* Thorax, 2011. **66**(7): p. 591-596.
185. Tuder, R.M. and I. Petrache, *Pathogenesis of chronic obstructive pulmonary disease (vol 122, pg 2749, 2012).* Journal of Clinical Investigation, 2012. **122**(11): p. 4300-4300.
186. Balantic, M., et al., *A Polymorphism in ORMDL3 is Associated Not Only With Asthma Without Rhinitis but Also With Chronic Obstructive Pulmonary Disease.* Journal of Investigational Allergology and Clinical Immunology, 2013. **23**(4): p. 256-261.
187. Wilk, J.B., et al., *Genome-Wide Association Studies Identify CHRNA5/3 and HTR4 in the Development of Airflow Obstruction.* American Journal of Respiratory and Critical Care Medicine, 2012. **186**(7): p. 622-632.
188. Molfino, N.A., *Genetics of COPD.* Chest, 2004. **125**(5): p. 1929-1940.
189. Nakamura, H., *Genetics of COPD.* Allergology international : official journal of the Japanese Society of Allergology, 2011. **60**(3): p. 253-8.
190. Kattan, M., et al., *Pulmonary-Function Abnormalities in Symptom-Free Children after Bronchiolitis.* Pediatrics, 1977. **59**(5): p. 683-688.
191. Pullan, C.R. and E.N. Hey, *Wheezing, Asthma, and Pulmonary Dysfunction 10 Years after Infection with Respiratory Syncytial Virus in Infancy.* British Medical Journal, 1982. **284**(6330): p. 1665-1669.
192. Mok, J.Y.Q. and H. Simpson, *Outcome for Acute Bronchitis, Bronchiolitis, and Pneumonia in Infancy.* Archives of Disease in Childhood, 1984. **59**(4): p. 306-309.
193. Barker, D.J.P., et al., *Relation of Birth-Weight and Childhood Respiratory-Infection to Adult Lung-Function and Death from Chronic Obstructive Airways Disease.* British Medical Journal, 1991. **303**(6804): p. 671-675.
194. *How Serious is COPD.* 2015; Available from: http://www.lung.org/lung-health-and-diseases/lung-disease-lookup/copd/learn-about-copd/how-serious-is-copd.html?referrer=https://www.google.com/.
195. Macklem, P.T. and J. Mead, *Resistance of Central and Peripheral Airways Measured by a Retrograde Catheter.* Journal of Applied Physiology, 1967. **22**(3): p. 395-&.
196. Barnes, P.J. and S. Kleinert, *COPD--a neglected disease.* Lancet, 2004. **364**(9434): p. 564-5.

197. Jeffery, P.K., *Remodeling in asthma and chronic obstructive lung disease.* American Journal of Respiratory and Critical Care Medicine, 2001. **164**(10): p. S28-S38.
198. Chung, K.F., *The role of airway smooth muscle in the pathogenesis of airway wall remodeling in chronic obstructive pulmonary disease.* Proceedings of the American Thoracic Society, 2005. **2**(4): p. 347-54; discussion 371-2.
199. James, A.L. and S. Wenzel, *Clinical relevance of airway remodelling in airway diseases.* The European respiratory journal, 2007. **30**(1): p. 134-55.
200. Tiddens, H.A., et al., *Cartilaginous airway dimensions and airflow obstruction in human lungs.* American Journal of Respiratory and Critical Care Medicine, 1995. **152**(1): p. 260-6.
201. Sims, J.M., *An overview of asthma.* Dimensions of critical care nursing : DCCN, 2006. **25**(6): p. 264-8.
202. Pearce, N., J. Douwes, and R. Beasley, *Is allergen exposure the major primary cause of asthma?* Thorax, 2000. **55**(5): p. 424-31.
203. Cookson, W. and M. Moffatt, *Making sense of asthma genes.* The New England journal of medicine, 2004. **351**(17): p. 1794-6.
204. Holgate, S.T. and R. Polosa, *The mechanisms, diagnosis, and management of severe asthma in adults.* Lancet, 2006. **368**(9537): p. 780-93.
205. Ober, C. and T.C. Yao, *The genetics of asthma and allergic disease: a 21st century perspective.* Immunological reviews, 2011. **242**(1): p. 10-30.
206. Cookson, W.O. and M.F. Moffatt, *Genetics of asthma and allergic disease.* Human molecular genetics, 2000. **9**(16): p. 2359-64.
207. Akinbami, L.J., et al., *Trends in asthma prevalence, health care use, and mortality in the United States, 2001-2010.* NCHS data brief, 2012(94): p. 1-8.
208. *Expert Panel Report 3 (EPR-3): Guidelines for the Diagnosis and Management of Asthma-Summary Report 2007.* The Journal of allergy and clinical immunology, 2007. **120**(5 Suppl): p. S94-138.
209. Jarjour, N.N., et al., *Investigative use of bronchoscopy in asthma.* American Journal of Respiratory and Critical Care Medicine, 1998. **157**(3 Pt 1): p. 692-7.
210. James, A.L., et al., *Airway smooth muscle hypertrophy and hyperplasia in asthma.* American Journal of Respiratory and Critical Care Medicine, 2012. **185**(10): p. 1058-64.
211. Jeffery, P.K., *Remodeling and inflammation of bronchi in asthma and chronic obstructive pulmonary disease.* Proceedings of the American Thoracic Society, 2004. **1**(3): p. 176-83.
212. Tsuboi, M., et al., *Optical coherence tomography in the diagnosis of bronchial lesions.* Lung cancer, 2005. **49**(3): p. 387-94.
213. Michel, R.G., et al., *Optical coherence tomography as an adjunct to flexible bronchoscopy in the diagnosis of lung cancer: a pilot study.* Chest, 2010. **138**(4): p. 984-8.
214. Hariri, L.P., et al., *Volumetric optical frequency domain imaging of pulmonary pathology with precise correlation to histopathology.* Chest, 2013. **143**(1): p. 64-74.

215. Lam, S., et al., *In vivo optical coherence tomography imaging of preinvasive bronchial lesions.* Clinical cancer research : an official journal of the American Association for Cancer Research, 2008. **14**(7): p. 2006-11.
216. Armstrong, J.J., et al., *In vivo size and shape measurement of the human upper airway using endoscopic long-range optical coherence tomography.* Optics express, 2003. **11**(15): p. 1817-1826.
217. Armstrong, J.J., et al., *Quantitative upper airway imaging with anatomic optical coherence tomography.* American Journal of Respiratory and Critical Care Medicine, 2006. **173**(2): p. 226-33.
218. McLaughlin, R.A., et al., *Applying anatomical optical coherence tomography to quantitative 3D imaging of the lower airway.* Optics express, 2008. **16**(22): p. 17521-9.
219. McLaughlin, R.A., et al., *Respiratory gating of anatomical optical coherence tomography images of the human airway.* Optics express, 2009. **17**(8): p. 6568-77.
220. Robertson, C., et al., *Investigating in vivo airway wall mechanics during tidal breathing with optical coherence tomography.* Journal of Biomedical Optics, 2011. **16**(10): p. 106011.
221. Williamson, J.P., et al., *Measuring airway dimensions during bronchoscopy using anatomical optical coherence tomography.* The European respiratory journal, 2010. **35**(1): p. 34-41.
222. Noble, P.B., et al., *Airway narrowing assessed by anatomical optical coherence tomography in vitro: dynamic airway wall morphology and function.* Journal of Applied Physiology, 2010. **108**(2): p. 401-11.
223. Noble, P.B., et al., *Distribution of airway narrowing responses across generations and at branching points, assessed in vitro by anatomical optical coherence tomography.* Respiratory Research, 2010. **11**: p. 9.
224. Hanna, N., et al., *Two-dimensional and 3-dimensional optical coherence tomographic imaging of the airway, lung, and pleura.* The Journal of thoracic and cardiovascular surgery, 2005. **129**(3): p. 615-22.
225. Popp, A., et al., *Imaging of the three-dimensional alveolar structure and the alveolar mechanics of a ventilated and perfused isolated rabbit lung with Fourier domain optical coherence tomography.* Journal of Biomedical Optics, 2006. **11**(1): p. 014015.
226. McLaughlin, R.A., et al., *Static and dynamic imaging of alveoli using optical coherence tomography needle probes.* Journal of Applied Physiology, 2012. **113**(6): p. 967-74.
227. Pitris, C., et al., *High resolution imaging of the upper respiratory tract with optical coherence tomography: a feasibility study.* American Journal of Respiratory and Critical Care Medicine, 1998. **157**(5 Pt 1): p. 1640-4.
228. Yang, Y., et al., *Use of optical coherence tomography in delineating airways microstructure: comparison of OCT images to histopathological sections.* Physics in medicine and biology, 2004. **49**(7): p. 1247-55.
229. Coxson, H.O., et al., *Airway wall thickness assessed using computed tomography and optical coherence tomography.* American Journal of Respiratory and Critical Care Medicine, 2008. **177**(11): p. 1201-6.

230. Lee, A.M., et al., *Validation of airway wall measurements by optical coherence tomography in porcine airways.* Plos One, 2014. **9**(6): p. e100145.
231. Matsuba, K. and W.M. Thurlbeck, *A morphometric study of bronchial and bronchiolar walls in children.* The American review of respiratory disease, 1972. **105**(6): p. 908-13.
232. Adams, D.C., et al., *Birefringence microscopy platform for assessing airway smooth muscle structure and function in vivo.* Science translational medicine, 2016. **8**(359): p. 359ra131.
233. Mavadia-Shukla, J., et al. *In vivo Airway Imaging with High-speed Ultrahigh-resolution Endoscopic OCT*. in *Biomedical Optics 2016,* . 2016. Fort Lauderdale, Florida: Optical Society of America, 2016.
234. Lum, H. and W. Mitzner, *Effects of 10% formalin fixation on fixed lung volume and lung tissue shrinkage. A comparison of eleven laboratory species.* The American review of respiratory disease, 1985. **132**(5): p. 1078-83.
235. Suter, M.J., et al., *Esophageal-guided biopsy with volumetric laser endomicroscopy and laser cautery marking: a pilot clinical study.* Gastrointestinal endoscopy, 2014. **79**(6): p. 886-96.
236. Vogelstein, B. and K.W. Kinzler, *The multistep nature of cancer.* Trends in genetics : TIG, 1993. **9**(4): p. 138-41.
237. Fearon, E.R., *Molecular genetics of colorectal cancer.* Annual review of pathology, 2011. **6**: p. 479-507.
238. Tjalsma, H., et al., *A bacterial driver-passenger model for colorectal cancer: beyond the usual suspects.* Nature reviews. Microbiology, 2012. **10**(8): p. 575-82.
239. Sears, C.L. and D.M. Pardoll, *Perspective: alpha-bugs, their microbial partners, and the link to colon cancer.* The Journal of infectious diseases, 2011. **203**(3): p. 306-11.
240. Group, U.S.C.S.W., *United States Cancer Statistics: 1999-2011 Incidence and Mortality Web-based Report*, 2014, U.S. Department of Health and Human Services, Centers for Disease Control and Prevention and National Cancer Institute: Atlanta.
241. Siegel, R., C. DeSantis, and A. Jemal, *Colorectal cancer statistics, 2014.* Ca-a Cancer Journal for Clinicians, 2014. **64**(2): p. 104-117.
242. Qaseem, A., et al., *Screening for Colorectal Cancer: A Guidance Statement From the American College of Physicians (vol 156, pg 378, 2012).* Annals of Internal Medicine, 2012. **157**(2): p. 152-152.
243. Qaseem, A., et al., *Screening for Colorectal Cancer: A Guidance Statement From the American College of Physicians.* Annals of Internal Medicine, 2012. **156**(5): p. 378-U209.
244. Yi, J., et al., *Spatially resolved optical and ultrastructural properties of colorectal and pancreatic field carcinogenesis observed by inverse spectroscopic optical coherence tomography.* Journal of Biomedical Optics, 2014. **19**(3).
245. Cothren, R.M., et al., *Detection of dysplasia at colonoscopy using laser-induced fluorescence: A blinded study.* Gastrointestinal Endoscopy, 1996. **44**(2): p. 168-176.
246. Marchesini, R., et al., *Light-Induced Fluorescence Spectroscopy of Adenomas, Adenocarcinomas and Nonneoplastic Mucosa in Human Colon .1. Invitro*

Measurements. Journal of Photochemistry and Photobiology B-Biology, 1992. **14**(3): p. 219-230.
247. McCallum, A.L., et al., *Evaluation of autofluorescence colonoscopy for the detection and diagnosis of colonic polyps.* Gastrointestinal Endoscopy, 2008. **68**(2): p. 283-290.
248. Mayinger, B., et al., *Endoscopic light-induced autofluorescence spectroscopy for the diagnosis of colorectal cancer and adenoma.* Journal of Photochemistry and Photobiology B-Biology, 2003. **70**(1): p. 13-20.
249. Pitris, C., et al., *Feasibility of optical coherence tomography for high-resolution imaging of human gastrointestinal tract malignancies.* Journal of Gastroenterology, 2000. **35**(2): p. 87-92.
250. Kobayashi, K., et al., *High-resolution cross-sectional imaging of the gastrointestinal tract using optical coherence tomography: preliminary results.* Gastrointestinal Endoscopy, 1998. **47**(6): p. 515-523.
251. Hung, K.E., et al., *Development of a mouse model for sporadic and metastatic colon tumors and its use in assessing drug treatment.* Proceedings of the National Academy of Sciences of the United States of America, 2010. **107**(4): p. 1565-1570.
252. Xue, Y.B., et al., *Generation of a Transgenic Mouse for Colorectal Cancer Research with Intestinal Cre Expression Limited to the Large Intestine.* Molecular Cancer Research, 2010. **8**(8): p. 1095-1104.
253. Rosenberg, D.W., C. Giardina, and T. Tanaka, *Mouse models for the study of colon carcinogenesis.* Carcinogenesis, 2009. **30**(2): p. 183-196.
254. Becker, C., M.C. Fantini, and M.F. Neurath, *High resolution colonoscopy in live mice.* Nature Protocols, 2006. **1**(6): p. 2900-2904.
255. Becker, C., et al., *In vivo imaging of colitis and colon cancer development in mice using high resolution chromoendoscopy.* Gut, 2005. **54**(7): p. 950-954.
256. Funovics, M.A., et al., *Simultaneous fluorescence imaging of protease expression and vascularity during murine colonoscopy for colonic lesion characterization.* Gastrointestinal Endoscopy, 2006. **64**(4): p. 589-597.
257. McCallum, A.L., et al., *Evaluation of autofluorescence colonoscopy for the detection and diagnosis of colonic polyps.* Gut, 2006. **55**: p. A24-A24.
258. Hariri, L.P., et al., *Endoscopic optical coherence tomography and laser-induced fluorescence spectroscopy in a murine colon cancer model.* Lasers in Surgery and Medicine, 2006. **38**(4): p. 305-313.
259. Wall, R.A. and J.K. Barton, *Fluorescence-based surface magnifying chromoendoscopy and optical coherence tomography endoscope.* Journal of Biomedical Optics, 2012. **17**(8).
260. Rabizadeh, S., et al., *Enterotoxigenic bacteroides fragilis: a potential instigator of colitis.* Inflammatory bowel diseases, 2007. **13**(12): p. 1475-83.
261. Sears, C.L., A.L. Geis, and F. Housseau, *Bacteroides fragilis subverts mucosal biology: from symbiont to colon carcinogenesis.* The Journal of clinical investigation, 2014. **124**(10): p. 4166-72.
262. Zeineldin, M. and K.L. Neufeld, *More than two decades of Apc modeling in rodents.* Biochimica Et Biophysica Acta-Reviews on Cancer, 2013. **1836**(1): p. 80-89.

263. Housseau, F. and C.L. Sears, *Enterotoxigenic Bacteroides fragilis (ETBF)-mediated colitis in Min (Apc(+/-)) mice A human commensal-based murine model of colon carcinogenesis.* Cell Cycle, 2010. **9**(1): p. 3-5.
264. Sacco, R.L., et al., *Guidelines for prevention of stroke in patients with ischemic stroke or transient ischemic attack: a statement for healthcare professionals from the American Heart Association/American Stroke Association Council on Stroke: co-sponsored by the Council on Cardiovascular Radiology and Intervention: the American Academy of Neurology affirms the value of this guideline.* Circulation, 2006. **113**(10): p. e409-49.
265. Hossmann, K.A., *Viability Thresholds and the Penumbra of Focal Ischemia.* Annals of Neurology, 1994. **36**(4): p. 557-565.
266. Kaplan, B., et al., *Temporal Thresholds for Neocortical Infarction in Rats Subjected to Reversible Focal Cerebral-Ischemia.* Stroke, 1991. **22**(8): p. 1032-1039.
267. Srinivasan, V.J., et al., *Quantitative cerebral blood flow with Optical Coherence Tomography.* Optics Express, 2010. **18**(3): p. 2477-2494.
268. Jia, Y.L. and R.K. Wang, *Label-free in vivo optical imaging of functional microcirculations within meninges and cortex in mice.* Journal of Neuroscience Methods, 2010. **194**(1): p. 108-115.
269. Srinivasan, V.J., et al., *Rapid volumetric angiography of cortical microvasculature with optical coherence tomography.* Optics Letters, 2010. **35**(1): p. 43-45.
270. Lee, J., et al., *Motion correction for phase-resolved dynamic optical coherence tomography imaging of rodent cerebral cortex.* Optics Express, 2011. **19**(22): p. 21258-21270.
271. Liu, G.J., et al., *A comparison of Doppler optical coherence tomography methods.* Biomedical Optics Express, 2012. **3**(10): p. 2669-2680.
272. Ren, H.W., et al., *Phase-resolved functional optical coherence tomography: simultaneous imaging of in situ tissue structure, blood flow velocity, standard deviation, birefringence, and Stokes vectors in human skin.* Optics Letters, 2002. **27**(19): p. 1702-1704.
273. Yang, V.X.D., et al., *Improved phase-resolved optical Doppler tomography using the Kasai velocity estimator and histogram segmentation.* Optics Communications, 2002. **208**(4-6): p. 209-214.
274. Carmeliet, P. and R.K. Jain, *Angiogenesis in cancer and other diseases.* Nature, 2000. **407**(6801): p. 249-57.
275. Folkman, J., *Tumor angiogenesis: therapeutic implications.* The New England journal of medicine, 1971. **285**(21): p. 1182-6.
276. Folkman, J., *Role of angiogenesis in tumor growth and metastasis.* Seminars in oncology, 2002. **29**(6 Suppl 16): p. 15-8.
277. Vakoc, B.J., et al., *Three-dimensional microscopy of the tumor microenvironment in vivo using optical frequency domain imaging.* Nature Medicine, 2009. **15**(10): p. 1219-23.
278. Mariampillai, A., et al., *Optimized speckle variance OCT imaging of microvasculature.* Optics Letters, 2010. **35**(8): p. 1257-9.

279. Mariampillai, A., et al., *Speckle variance detection of microvasculature using swept-source optical coherence tomography.* Optics Letters, 2008. **33**(13): p. 1530-2.
280. Mahmud, M.S., et al., *Review of speckle and phase variance optical coherence tomography to visualize microvascular networks.* Journal of Biomedical Optics, 2013. **18**(5): p. 50901.
281. Liu, G.J., et al., *Intensity-based modified Doppler variance algorithm: application to phase instable and phase stable optical coherence tomography systems.* Optics express, 2011. **19**(12): p. 11429-11440.
282. Liu, G., et al., *A comparison of Doppler optical coherence tomography methods.* Biomedical Optics Express, 2012. **3**(10): p. 2669-80.
283. Liu, G.J., et al., *High-resolution imaging of microvasculature in human skin in-vivo with optical coherence tomography.* Optics express, 2012. **20**(7): p. 7694-7705.
284. Srinivasan, V.J., et al., *Rapid volumetric angiography of cortical microvasculature with optical coherence tomography.* Optics Letters, 2010. **35**(1): p. 43-5.
285. Zhao, Y., et al., *Doppler standard deviation imaging for clinical monitoring of in vivo human skin blood flow.* Optics Letters, 2000. **25**(18): p. 1358-60.
286. Leitgeb, R., et al., *Real-time assessment of retinal blood flow with ultrafast acquisition by color Doppler Fourier domain optical coherence tomography.* Optics express, 2003. **11**(23): p. 3116-21.
287. Liu, G., et al., *Real-time bulk-motion-correction free Doppler variance optical coherence tomography for choroidal capillary vasculature imaging.* Optics express, 2011. **19**(4): p. 3657-66.
288. Ren, H., et al., *Imaging and quantifying transverse flow velocity with the Doppler bandwidth in a phase-resolved functional optical coherence tomography.* Optics Letters, 2002. **27**(6): p. 409-11.
289. Wang, R.K., *Three-dimensional optical micro-angiography maps directional blood perfusion deep within microcirculation tissue beds in vivo.* Physics in medicine and biology, 2007. **52**(23): p. N531-7.
290. Wang, R.K., et al., *Three dimensional optical angiography.* Optics express, 2007. **15**(7): p. 4083-97.
291. Wojtkowski, M., et al., *Full range complex spectral optical coherence tomography technique in eye imaging.* Optics Letters, 2002. **27**(16): p. 1415-7.
292. An, L. and R.K. Wang, *In vivo volumetric imaging of vascular perfusion within human retina and choroids with optical micro-angiography.* Optics express, 2008. **16**(15): p. 11438-52.
293. An, L. and R.K. Wang, *Use of a scanner to modulate spatial interferograms for in vivo full-range Fourier-domain optical coherence tomography.* Optics Letters, 2007. **32**(23): p. 3423-3425.
294. Baumann, B., et al., *Full range complex spectral domain optical coherence tomography without additional phase shifters.* Optics express, 2007. **15**(20): p. 13375-87.

295. Zhang, J., J.S. Nelson, and Z. Chen, *Removal of a mirror image and enhancement of the signal-to-noise ratio in Fourier-domain optical coherence tomography using an electro-optic phase modulator.* Optics Letters, 2005. **30**(2): p. 147-9.
296. Bachmann, A., R. Leitgeb, and T. Lasser, *Heterodyne Fourier domain optical coherence tomography for full range probing with high axial resolution.* Optics express, 2006. **14**(4): p. 1487-96.
297. Gotzinger, E., et al., *High speed full range complex spectral domain optical coherence tomography.* Optics express, 2005. **13**(2): p. 583-94.
298. Lee, H.C., et al., *Circumferential optical coherence tomography angiography imaging of the swine esophagus using a micromotor balloon catheter.* Biomedical Optics Express, 2016. **7**(8): p. 2927-42.
299. Mavadia, J., et al., *An all-fiber-optic endoscopy platform for simultaneous OCT and fluorescence imaging.* Biomedical Optics Express, 2012. **3**(11): p. 2851-9.
300. Mavadia, J., et al. *All-Fiber-Optic Based Catheter System for Simultaneous Endoscopic Optical Coherence Tomography and Fluorescence Imaging*. in *OSA BIOMED*. 2012. Miami: OSA Technical Digest.
301. Dacosta, R.S., B.C. Wilson, and N.E. Marcon, *New optical technologies for earlier endoscopic diagnosis of premalignant gastrointestinal lesions.* Journal of Gastroenterology and Hepatology, 2002. **17 Suppl**: p. S85-104.
302. Kiesslich, R., et al., *Confocal laser endoscopy for diagnosing intraepithelial neoplasias and colorectal cancer in vivo.* Gastroenterology, 2004. **127**(3): p. 706-713.
303. Barton, J.K., F. Guzman, and A. Tumlinson, *Dual modality instrument for simultaneous optical coherence tomography imaging and fluorescence spectroscopy.* Journal of Biomedical Optics, 2004. **9**(3): p. 618-623.
304. Yuan, S.A., et al., *Co-registered optical coherence tomography and fluorescence molecular imaging for simultaneous morphological and molecular imaging.* Physics in Medicine and Biology, 2010. **55**(1): p. 191-206.
305. Zhao, Y.B., et al., *Integrated multimodal optical microscopy for structural and functional imaging of engineered and natural skin.* Journal of Biophotonics, 2012. **5**(5-6): p. 437-448.
306. Hariri, L., et al., *Ex vivo optical coherence tomography and laser induced fluorescence spectroscopy imaging of murine gastrointestinal tract.* Advanced Biomedical and Clinical Diagnostic Systems III, 2005. **5692**: p. 295-306.
307. Wall, R.A., G.T. Bonnema, and J.K. Barton, *Focused OCT and LIF Endoscope.* Endoscopic Microscopy V, 2010. **7558**: p. - 98.
308. Wall, R.A., G.T. Bonnema, and J.K. Barton, *Novel focused OCT-LIF endoscope.* Biomedical Optics Express, 2011. **2**(3): p. 421-430.
309. Ryu, S.Y., et al., *Combined system of optical coherence tomography and fluorescence spectroscopy based on double-cladding fiber.* Optics Letters, 2008. **33**(20): p. 2347-2349.
310. Ryu, S.Y., et al., *The Development of Double Clad Fiber and Double Clad Fiber Coupler for Fiber Based Biomedical Imaging Systems.* Journal of the Optical Society of Korea, 2009. **13**(3): p. 310-315.

311. Ryu, S.Y., et al., *Combined swept-source optical coherence tomography and fluorescence spectroscopy system.* Multimodal Biomedical Imaging V, 2010. **7557**.
312. Lemire-Renaud, S., et al., *Double-clad fiber coupler for endoscopy.* Optics express, 2010. **18**(10): p. 9755-9764.
313. Madore, W.J., et al., *Asymmetric double-clad fiber couplers for endoscopy.* Optics Letters, 2013. **38**(21): p. 4514-4517.
314. Yoo, H., et al., *Intra-arterial catheter for simultaneous microstructural and molecular imaging in vivo.* Nature Medicine, 2011. **17**(12): p. 1680-U202.
315. Liang, S., et al., *Intravascular atherosclerotic imaging with combined fluorescence and optical coherence tomography probe based on a double-clad fiber combiner.* Journal of Biomedical Optics, 2012. **17**(7): p. 070501.
316. Lorenser, D., et al., *Dual-modality needle probe for combined fluorescence imaging and three-dimensional optical coherence tomography.* Optics Letters, 2013. **38**(3): p. 266-8.
317. Scolaro, L., et al. *Dual-modality Imaging Needle for Combined Optical Coherence Tomography and Fluorescence Imaging of Fluorescently Labelled Tissue*. in *BIOMED*. 2014. OSA.
318. de Boer, J.F., et al., *Two-dimensional birefringence imaging in biological tissue by polarization-sensitive optical coherence tomography.* Optics Letters, 1997. **22**(12): p. 934-6.
319. de Boer, J.F. and T.E. Milner, *Review of polarization sensitive optical coherence tomography and Stokes vector determination.* Journal of Biomedical Optics, 2002. **7**(3): p. 359-71.
320. Kennedy, K.M., et al., *Quantitative micro-elastography: imaging of tissue elasticity using compression optical coherence elastography.* Scientific Reports, 2015. **5**: p. 15538.
321. Singh, M., et al., *Phase-sensitive optical coherence elastography at 1.5 million A-Lines per second.* Optics Letters, 2015. **40**(11): p. 2588-2591.

BIOGRAPHY

Jessica Mavadia-Shukla was born in 1988 in the U.S.A. In spring of 2010, Jessica graduated Summa Cum Laude from New Jersey Institute of Technology, Newark, New Jersey, with an undergraduate degree in biomedical engineering. During her undergraduate studies she was a summer biomedical research intern at the National Institutes of Health in 2008 and 2009. In addition, for 3 semesters, she was an undergraduate teaching assistant for a sophomore level Biomedical Computing course.

In fall of 2010, Jessica began her PhD at Johns Hopkins University. During her graduate studies she was a graduate teaching assistant for Principles of Instrumentation Lab and Systems Bioengineering Lab I. In addition, she served as the vice president and president of the JHU SPIE Student Chapter, where she organized and participated in community outreach events and organized university seminars.